Optical Antenna Enhanced Spontaneous Emission in Semiconductors

By

Kevin James Messer

A dissertation submitted in partial satisfaction of the

requirements for the degree of

Doctor of Philosophy

in

Engineering – Electrical Engineering and Computer Sciences

in the

Graduate Division

of the

University of California, Berkeley

Committee in Charge:

Professor Eli Yablonovitch, Chair
Professor Ming C. Wu
Professor Feng Wang

Spring 2016

Optical Antenna Enhanced Spontaneous Emission in Semiconductors

Abstract

Optical Antenna Enhanced Spontaneous Emission in Semiconductors

by

Kevin James Messer

Doctor of Philosophy in Engineering – Electrical Engineering and Computer Sciences

University of California, Berkeley

Professor Eli Yablonovitch, Chair

Optical antennas can be used to dramatically increase the rate that semiconductors spontaneously emit photons. While traditional LEDs are limited in bandwidth due to the "slow" rate of spontaneous emission, antenna-enhanced LEDs have the potential to be a fast, efficient, nanoscale light emitter. Traditionally, lasers have dominated LEDs as the emitter in optical interconnects due to a 200x speed advantage of stimulated emission over spontaneous emission. This paradigm may be reversed by coupling LEDs to optical antennas. In fact, antenna enhanced spontaneous emission can be faster than the fastest stimulated emission.

Spontaneous emission originates from dipole fluctuations within the emitting material. The size of these fluctuations is much less than the wavelength of light emission, which leads to slow spontaneous emission. Coupling the material to an optical antenna corrects the size mismatch and improves the rate of radiation. An optical antenna circuit model is developed to predict the degree to which spontaneous emission can be enhanced. The circuit model presented in this dissertation shows that enhancement over 1000x is possible while still maintaining greater than 50% efficiency.

The circuit model provides insight how to design optical antennas for coupling to dipole sources, for maximum enhancement, and for high efficiency. A method for incorporating the anomalous skin effect, often overlooked in metal optics, is provided. While FDTD/FEM simulations cannot include this effect due to its nonlocal nature, its impact can be examined through the use of the optical antenna circuit model. Analysis of the tradeoff between achieving large spontaneous emission enhancement and maintaining high efficiency leads to an ideal antenna feedgap size of 10nm.

Experimental demonstration of spontaneous emission enhancement from InP coupled to an arch-dipole antenna is presented. Photoluminescence measurements show light emission from antenna-coupled InP over bare InP ridges was enhanced by 120x. The results correspond to a 14x enhancement of spontaneous emission once absorption enhancement is taken into account.

To improve on the previous results, 2D materials from the family of transition metal dichalcogenides are used as the active material. In monolayer form, these materials are direct band gap semiconductors with very low rates of surface recombination. The cavity-backed slot antenna is used to couple to the monolayer semiconductor. The resonant properties of the cavity-backed slot antenna are measured through dark-field scattering and used to match the antenna resonance to the wavelength of light emission. A WSe_2 monolayer is etched into ribbons and coupled to the hotspot of a silver cavity-backed slot antenna resulting in an observed spontaneous emission enhancement of 318x.

Finally, an unetched MoS_2 monolayer is coupled to an array of gold cavity-backed slot antennas in order to demonstrate both high enhancement and high quantum efficiency. Spatially resolved photoluminescence measurements show efficient emission only in the location of optical antennas. Areas of the MoS_2 monolayer coupled to antennas show 7% quantum efficiency corresponding to a >250x increase in efficiency over bare MoS_2 monolayers. These results demonstrate the exciting potential for antenna-enhanced LEDs to be both fast and efficient light emitters.

Acknowledgments

Table of Contents

List of Figures

1 Introduction

Antennas are used to focus electromagnetic radiation to length scales much smaller than a wavelength. Operated in reverse, antenna can be used to efficiently transfer energy from a sub-wavelength structure into electromagnetic radiation. This holds true for all frequency regimes of the electromagnetic spectrum. We have all had experience with radio frequency antennas through cell phones, radios, and televisions, but the applications of optical antennas are only now beginning to be explored. Interestingly, the designs used for optical antennas are very similar to radio frequency antennas. This is a result of the linearity of Maxwell's equations. A million-fold decrease in the wavelength results in an equivalent million-fold decrease in the antenna dimensions. However, a notable difference in the optical regime is the properties of the metals used to make the antennas. The effects of material properties on optical antennas will be discussed in Chapter 3 of this dissertation.

Optical antennas have numerous potential applications due to their ability to enhance light-matter interactions at the nanoscale. Inefficient light emitters can get a boost in efficiency when coupled to an optical antenna resulting in stronger photoluminescence (PL). The vibrational structure of materials can be explored by using optical antennas for surface-enhanced Raman spectroscopy (SERS). Nonlinear effects can be enhanced by strengthening the local electric field in an optical antenna gap. The focusing nature of optical antennas can be utilized for nanoscale imaging. Optical antennas can be used to focus energy from a laser to heat nanoscale magnets for heat-assisted magnetic recording (HAMR) in the hard drive industry.

Incorporating a semiconductor in the feedgap of an optical antenna leads to even more potential applications. Acting as a receiver, there is potential for optical antenna enhanced photodetectors and photovoltaics. As an emitter, the potential for antenna-enhanced LEDs exists. This application, enhancing spontaneous emission in semiconductors using optical antennas, is the prime focus of this dissertation.

The fundamental physics behind spontaneous emission and antenna-enhanced spontaneous emission will be discussed in Chapter 1. In Chapter 2, the potential for antenna-enhanced LEDs to compete with lasers as the emitter in optical interconnects will be presented. Chapter 3 develops a circuit model that describes the enhancement and efficiency attainable using optical antennas. This circuit model gives insight into proper optical antenna design and can incorporate effects not included in simulation tools. Chapter 4 provides analysis of optical antenna materials and some antenna designs. Experimental demonstration of spontaneous emission enhancement in InP is shown in Chapter 5. Finally, Chapter 6 contains experiments demonstrating spontaneous emission

enhancement in WSe_2 and MoS_2. Both high efficiency and large enhancement are observed by coupling the monolayer semiconductors to an optical antenna.

1.1 Spontaneous Emission

Spontaneous emission is the process by which an excited electron spontaneously loses energy to emit a photon. In semiconductors, this occurs when an electron in the conduction band recombines with a hole in the valence band to emit a photon of energy close to the semiconductor's band gap. By connecting a supply of energized electrons to a semiconducting material, spontaneous emission can efficiently generate light as is done in LEDs. The goal of this section will be to explain what drives this light emission process and what determines the average time it takes to occur.
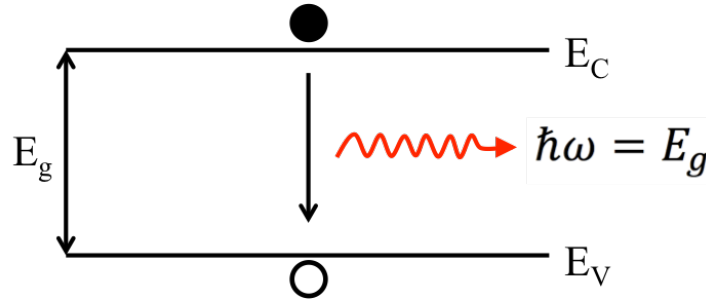
Figure 1. Spontaneous emission of a photon from an excited electron-hole pair in a semiconductor.

The seemingly simple process of spontaneous emission is actually a result of one of the most fundamental ideas in Quantum Mechanics, the Heisenberg Uncertainty principle. The principle states that there is always a minimum uncertainty in knowing the position and momentum of a particle. Equivalently, this means that the lowest energy state of a system will have non-zero energy. As is done in many textbooks, applying this principle to a quantum harmonic oscillator yields the zero point energy of half a photon, $E_0 = \hbar\omega/2$. Quantum field theory extends the idea of the harmonic oscillator to electromagnetic fields. Each electromagnetic mode of a system consists of a harmonic oscillator and will contain a minimum energy, E_0. Understanding the time averaged energy density of an electromagnetic wave can be expressed as $E/V = \epsilon_0 n^2 \mathcal{E}^2$ allows us to define the zero-point electric field as:

$$\mathcal{E}_{zpf} = \sqrt{\hbar\omega/2\epsilon_0 n^2 V} \tag{1.1}$$

where ϵ_0 is the permittivity of free space, n is the index of refraction, and V is the volume of the electromagnetic mode.

The zero-point electric field is present in every electromagnetic mode, including regions where energized electrons are present. The interaction of the zero-point field with the electron is a perturbation to the excited state of the electron. Fermi's Golden Rule can be employed to describe transitions between states when such a perturbation is present[1],[2]. The transition rate, W_{if}, from an initial state, i, to a final state, f, due to the perturbation, H', can be expressed as:

$$W_{fi} = \frac{2\pi}{\hbar} \langle f|H'|i\rangle^2 \delta(E_f - E_i + \hbar\omega) \tag{1.2}$$

The perturbation, H', for the interaction between the electron and photon in the dipole approximation is given by:

$$H' = -\langle f|q\boldsymbol{r} \cdot \boldsymbol{E}|i\rangle \tag{1.3}$$

where $\boldsymbol{r}$ is the position vector of the electron of charge q, and $\boldsymbol{E}$ is the electric field vector. For spontaneous emission, the only field present will be the zero-point electric field given in (1.1). By recognizing the electric field will not change appreciably over a unit cell, we may reduce (1.3) to include the dipole moment, $\boldsymbol{x_0} = \langle f|\boldsymbol{r}|i\rangle$.

$$H' = -q\boldsymbol{x_0} \cdot \boldsymbol{E} \tag{1.4}$$

The spontaneous emission process requires the transition of electron from excited state, i, to ground state, f, and the emission of a photon with energy $\hbar\omega = E_i - E_f$. An available photon state must therefore exist at energy $\hbar\omega$. The density of photon states, ρ_{phot}, must be included in the transition rate of Fermi's Golden rule. We may now express the spontaneous emission rate, Γ_{sp}, as:

$$\Gamma_{sp} = \frac{2\pi}{\hbar} \left(qx_0\mathcal{E}_{zpf}\right)^2 \rho_{phot} \tag{1.5}$$

The consequences of equation (1.5) are profound. It tells us that the spontaneous emission rate is not a fixed quantity, but instead depends on the electromagnetic environment of the excited electron. The electric field perturbation will depend on the refractive index of the medium and mode volume through (1.1), and the optical density of states can be engineered to be either very high or low at the frequency of our choosing. If we ask how fast the spontaneous emission rate can be, this would suggest that the only limit would be when perturbation theory breaks down near the strong coupling regime. Practical considerations due to loss in antennas will limit the spontaneous emission rate before the perturbation theory limit occurs, but it gives an indication that spontaneous emission can be greatly enhanced beyond typical rates.

Equation (1.5) also draws an interesting comparison between spontaneous emission and stimulated emission. While stimulated emission requires an applied electric field in order to drive transitions from the excited state to ground state, spontaneous emission only requires the zero-point field. Both light emission processes have rates dependent on the

3

intensity of the driving electric field. Because of this, lasers require a high photon density in the laser cavity in order to achieve fast modulation. Materials will always undergo some type of breakdown due to the high fields involved in stimulated emission, leading to the practical limit of stimulated emission around 50GHz. Spontaneous emission has no such limitation because no applied field is required for emission to occur. Instead, the electromagnetic environment can be designed so that the zero-point field is incredibly strong and spontaneous transitions occur quickly.

An additional requirement for spontaneous emission to occur is momentum matching of the electron-hole pair. The spontaneous emission rate derived here is valid under the assumption that the excited state is already momentum matched to an available ground state. In real semiconductors, terms would be added to account for the k-space distribution of carriers in the conduction and valence band as well as the carrier occupation in each band.

Let us now consider the case of spontaneous emission in a homogenous medium of refractive index, n. The density of photon states, in a volume, V, for this case is easily derived in optics textbooks[1].

$$\rho_{phot} = \frac{\omega^2 n^3 V}{\pi^2 \hbar c^3} \tag{1.6}$$

We insert (1.1) and (1.6) into (1.5) to give the spontaneous emission rate. Additionally, we average over all dipole orientations in three dimensions giving a factor of 1/3.

$$\Gamma_{sp} = \frac{\omega^3 q^2 x_0^2 n}{3\pi \hbar c^3 \epsilon_0} \tag{1.7}$$

This is the conventional rate of spontaneous emission from a dipole. When coupled to the carrier dynamics in semiconductors this yields a spontaneous emission lifetime, $\tau_{sp} = 1/\Gamma_{sp}$, on the order of 1ns. It should be noted that finding the analytic solution for the photon density of states for this situation is incredibly easy. For complicated structures involving metals, a simple analytic solution of the photon density of states cannot be done. In light of this, it is much more intuitive to treat the problem of spontaneous emission enhancement with antenna theory.

1.2 Antenna Enhanced Spontaneous Emission

The spontaneous emission rate of light from semiconductors can be expressed in terms of antenna theory. In the analogy to classic antenna theory, the optical dipole matrix element, x_0, of a semiconductor material can be treated as a small dipole emitting radiation. For most semiconductors the dipole moment is on the order of a unit cell, corresponding to a length of roughly 0.5 nm [3]. The wavelength of light emission from

most semiconductors is several hundreds of nanometers. Clearly, the dipole moment is much smaller than the wavelength of emission, so we may treat it as a radiating Hertzian dipole. This large dimensional mismatch is an unfortunate act of nature, but gives us the opportunity to dramatically increase the rate of spontaneous emission.

We may treat the spontaneous emission of a photon from an electron-hole pair in terms of radiated power in the following way:

$$\frac{1}{\tau_{sp}} = \frac{P_{rad}}{\hbar\omega} = \frac{I^2 R_{rad}}{2\hbar\omega} = \frac{(q\omega)^2 R_{rad}}{2\hbar\omega} \tag{1.8}$$

Here, $I = q\omega$ is the quantum mechanical current due to the oscillating dipole moment in the material. R_{rad} is the radiation resistance of the material dipole moment, and can be expressed as the radiation resistance of a Hertzian dipole [4] with length $\ell = 2x_0$.

$$R_{rad} = \frac{2\pi}{3} Z_0 \left(\frac{2x_0}{\lambda}\right)^2 n \tag{1.9}$$

where $Z_0 = 1/\epsilon_0 c$ is the impedance of free space. Inserting (1.9) into (1.8) and converting wavelength terms to frequency gives an expression for the spontaneous emission rate:

$$\frac{1}{\tau_{sp}} = \frac{\omega^3 q^2 x_0^2 n}{3\pi\hbar c^3 \epsilon_0} \tag{1.10}$$

This is precisely the same expression as (1.7) which was derived directly from Fermi's Golden Rule. For this simplest case, we may draw a circuit model to express the situation.
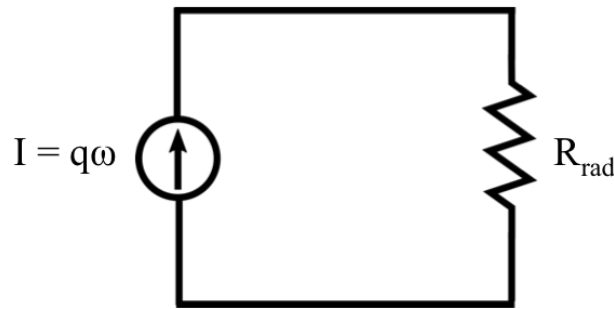
Figure 2. Circuit Model for spontaneous emission in homogenous electromagnetic environment

Here, the power dissipated in the radiation resistance is the power radiated by the dipole source, which can be related to the spontaneous emission lifetime through (1.8). The radiation resistance given in (1.9) is proportional to x_0^2/λ^2, making it immediately obvious that the small dipole moment will result in a very small radiation resistance. In

fact, for $x_0 = 0.5$ nm and $\lambda = 1000$nm, we get a radiation resistance of 0.8 mΩ. In contrast, antennas can easily have a radiation resistance of 50 Ω. Therefore, we should expect to be able to increase the power radiated by the source by several orders of magnitude with the use of an optical antenna.

In order to understand what type of spontaneous emission rate enhancement is possible using optical antennas we will construct a very basic model. Our antenna will be the dipole antenna with an emitted coupled to the feedgap as shown Figure 3.
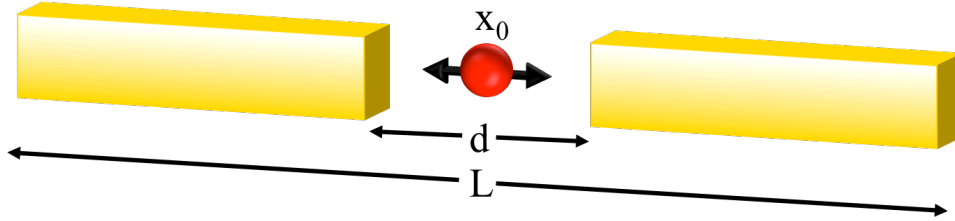
Figure 3. Dipole emitter coupled to an optical antenna

The radiation resistance for this antenna will be taken as that of a small dipole antenna [4].

$$R_{rad} = \frac{\pi}{6} Z_0 \left(\frac{L}{\lambda^2}\right)$$

(1.11)

In addition to power loss by radiation, the unavoidable loss in metal materials means there will also be some power dissipated as heat through ohmic losses. An extra resistor, R_Ω, will be used to represent this loss.

The final piece to the model is a description of the current source driving the antenna. In the case of spontaneous emission in a homogenous environment as in Figure 2, the dipole moment acts as its own antenna and gets the full benefit of the quantum mechanical current, $q\omega$. However, when a dipole emitter is coupled to an antenna, as in Figure 3, the full current is not induced into the arms of the antenna. The situation of a dipole oscillating in the feedgap of an antenna is essentially equivalent to that of a moving charge between to electrodes (Figure 4).
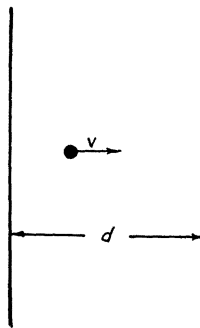
Figure 4. A moving charge with velocity, v, between two electrodes separated by a distance, d, induces a current in the electrodes. Reproduced from [5]

These two situations can be treated equivalent as long as we are able to make the quasistatic approximation, which is the case for a small antenna feedgap size, d. Following the work of Shockley [6] and Ramo [5], we can get the current induced in the antenna arms by the oscillating dipole source.

$$I = E_v q v \tag{1.12}$$

where E_v is the component of electric field in the direction of the moving charge at the position of the charge when the electrode is at 1 V and the charge is removed [5], [6]. For the case of a small gap between to parallel electrodes, the solution is:

$$I = \frac{q\omega x_0}{d} \tag{1.13}$$

The simple circuit model describing antenna enhanced spontaneous emission is shown below in Figure 5.
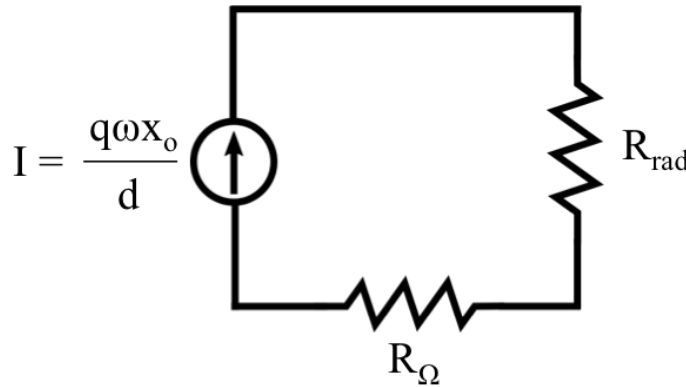
Figure 5. Simple circuit model for spontaneous emission from an emitter in the feedgap of a dipole antenna

The enhancement of the spontaneous emission rate can now be estimated by taking the ratio of the power emitted in the radiation resistance of Figure 5 to the power emitted in the radiation resistance of Figure 2. Nearly all terms cancel and we are left with an expression depending only on the length of the antenna and the size of the feedgap.

$$\text{Enhancement} \propto \left(\frac{L}{d}\right)^2 \tag{1.14}$$

Based on (1.14), the spontaneous emission enhancement can be very large for long antennas and small feedgaps. The benefit of an antenna is maximized when its length is roughly $\lambda/2$, so for a feedgap of 10 nm with emission at 1000 nm, we might expect an enhancement on the order of 2500x. This basic circuit model is only intended to give a

7

rough idea of what order of magnitude spontaneous emission enhancement is possible using optical antennas. A more detailed circuit model incorporating the resonant nature of antennas, the response of metals at optical frequencies, and the impact of ohmic loss will be presented in a later section.

A natural question to ask is, how is it possible for the same oscillating dipole moment to emit a different amount of power based only on its environment? Surely this violates some type of conservation law. The answer lies in the nature of the dipole moment. The oscillating dipole moment is almost an ideal current source due to its high impedance. The impedance of a small dipole is $|Z| = Z_0 \lambda / 2\pi x_0$ which is greater than $10^5 \ \Omega$ for most materials [7]. So, by placing this source in a different environment we are merely changing the voltage on the quantum current source. The zero-point fluctuations of the excited electron are doing more work when it is placed in the feed gap of the antenna. The concern of violating an energy conservation law is answered by noticing that energy must constantly be supplied to the system by an external source to maintain a concentration of excited carriers above thermal equilibrium. Once the external source is removed, the material will return to thermal equilibrium and the rate of spontaneous emission will be exactly balanced by absorption. The equilibration of carriers will of course occur more quickly when the material is coupled to an optical antenna.

1.3 The Purcell Effect and Antennas

Enhancement of the spontaneous emission rate was predicted by Purcell in a short conference paper in 1946 [8]. Purcell noticed that the optical density of states was not the typical free space value when a source was coupled to a resonator. In fact, the density of states could be much higher in the resonator than in free space. This has led to a large amount of work on exploiting microcavities to leverage the Purcell effect to enhance spontaneous emission. In this section the Purcell effect will first be derived followed by an explanation of the drawbacks to using the Purcell interpretation of optical antenna enhanced spontaneous emission.

To derive the Purcell enhancement of spontaneous emission, we proceed by reexamining (1.5). Instead of taking the photon density of states for a homogenous medium, we modify it to that of an optical cavity [1].We will treat this cavity as a Lorentzian resonance at resonant frequency, ω_0, with a bandwidth, $\Delta\omega$.

$$\rho_{phot} = \frac{(\hbar\Delta\omega)/(2\pi)}{(\hbar\omega - \hbar\omega_0)^2 + (\hbar\Delta\omega/2)^2} \tag{1.15}$$

The zero-point electric field must also be defined in the cavity in order to make use of (1.5). In the case of a homogenous medium, the zero-point electric field is uniform in space and was derived from the energy density of zero-point energy. For the case of an

optical cavity, a mode volume must be defined such that the cavity still contains a zero-point energy of $\hbar\omega/2$.

$$V_{eff} = \frac{\hbar\omega}{2\epsilon_0 n^2 \mathcal{E}_{\max}^2} \tag{1.16}$$

where $\mathcal{E}_{max}$ is the magnitude of the maximum zero-point electric field in the cavity. If we now take the location of the dipole emitter to be at the location and in the orientation of $\mathcal{E}_{max}$, the spontaneous emission rate at $\omega = \omega_0$ becomes:

$$\Gamma_{cav} = \frac{2q^2 x_0^2 Q}{\hbar\epsilon_0 n^2 V_{eff}} \tag{1.17}$$

where $Q = \omega_0/\Delta\omega$ is the quality factor of the cavity. Taking the ratio of (1.17) to (1.7) gives the Purcell enhancement of the spontaneous emission rate [8].

$$F_p = \frac{3Q}{4\pi^2 V_{eff}} \left(\frac{\lambda}{n}\right)^3 \tag{1.18}$$

Using the Purcell factor, F_p, to estimate spontaneous emission enhancement is a useful tool when the quality factor and mode volume are well-defined quantities. This approach is applicable to dielectric cavities with minimal optical loss. In these cavities analytic solutions can be obtained for Q and V_{eff} yielding a straightforward solution to (1.18). However, there are a number of issues that arise when the Purcell effect is used to explain antenna enhanced spontaneous emission.

First, the mode volume of an optical antenna cannot be well defined. A good antenna design has low Q due to the dominant rate of energy loss through radiation. Therefore, a method of calculating mode volume must be used which separates fields radiating into the far-field from fields contributing to stored energy in the antenna "cavity". This method of mode volume approximation has been shown to lead to significant error in prediction of the spontaneous emission enhancement [9].

Second, the Purcell factor in (1.18) accounts for all forms of energy dissipation from the cavity. In fact, it is correct to interpret the Purcell factor as the ratio of power dissipated by a dipole source placed in the position of interest, P_{cav}, to the power dissipated by a dipole in freespace, P_0.

$$F_p = \frac{P_{cav}}{P_0} \tag{1.19}$$

For dielectric cavities with minimal absorption nearly all loss from the cavity is in the form of radiation. In optical antennas there are significant losses due to absorption in metals. A significant portion of the power dissipated by a dipole source coupled to an optical antenna may be going directly to heat via ohmic loss. The Purcell factor simply

9

treats these losses as another form of energy decay adding to the emitter's decay rate. Instead of sweeping these non-radiative losses into the total decay rate, this dissertation will distinguish the various decay channels into which the emitter loses its energy. Due to this distinction, an added emphasis is put on the efficiency of devices used to enhance the spontaneous emission rate.

1.4 Speed and Quantum Efficiency

Highly efficient conversion of energy between electricity and light is a desirable quality for any optoelectronic device. The simultaneous desire for high-speed devices often comes with a trade-off in device efficiency. This section will study the connection between the modulation rate of LEDs and their quantum efficiency. The interplay between these two design requirements leads to interesting design choices for antenna enhanced LEDs.

Carriers in semiconductors may decay radiatively by emitting a photon of light or non-radiatively by converting their energy into heat. These recombination processes occur in parallel and therefore compete with one another. Each may be assigned a lifetime describing the average rate of occurrence. In this way, the quantum efficiency, QE, and total carrier recombination rate, Γ_{tot}, can be defined.

$$QE = \frac{\dfrac{1}{\tau_r}}{\dfrac{1}{\tau_r} + \dfrac{1}{\tau_{nr}}} \tag{1.20}$$

$$\Gamma_{tot} = \frac{1}{\tau_r} + \frac{1}{\tau_{nr}} \tag{1.21}$$

The connection between efficiency and speed in clear from (1.20) and (1.21). As an example, let us consider a bulk semiconductor know to have a spontaneous emission lifetime of 1 ns. If the material is completely free of defects, we may take $\tau_{nr} = \infty$. This situation would yield of quantum efficiency of 100% and $\Gamma_{tot} = 1$ GHz. If the material were suddenly inundated with defects so that $\tau_{nr} = 1$ ps, the quantum efficiency would plummet to 0.1%, but the total rate of recombination would increase to 1 THz. Due to the tradeoff between efficiency and speed, an increase in the spontaneous emission rate of a semiconductor is only useful if it maintains high efficiency.
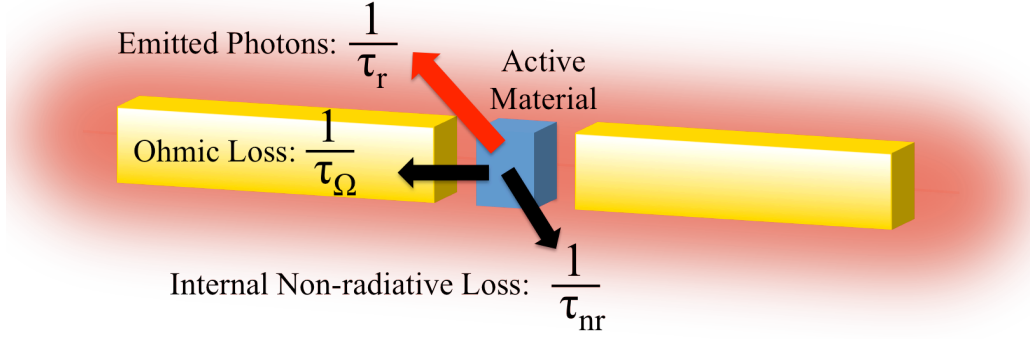
Figure 6. Energy decay channels for a semiconductor coupled to an optical antenna.

When optical antennas are used to modify the spontaneous emission rate, the efficiency and decay rate equations must be adjusted to incorporate both the new rate of spontaneous emission as well as the rate of energy dissipation into ohmic losses in the antenna. Figure 6 shows the three decay channels present when a semiconductor is coupled to an optical antenna. Incorporating ohmic loss gives the new efficiency and rate equations:

$$QE = \frac{\frac{1}{\tau_r}}{\frac{1}{\tau_r} + \frac{1}{\tau_\Omega} + \frac{1}{\tau_{nr}}} \tag{1.22}$$

$$\Gamma_{tot} = \frac{1}{\tau_r} + \frac{1}{\tau_\Omega} + \frac{1}{\tau_{nr}} \tag{1.23}$$

Alternatively, it can be useful to express (1.22) and (1.1)in terms of the homogenous material (bulk semiconductor) spontaneous emission lifetime, τ_0. To do so, we make use of the enhancement factor, F_p. Recall that this factor incorporates both power radiated by the antenna and ohmic losses in the antenna, so we have the expression:

$$F_p = \frac{P_{ant}}{P_0} = \frac{\frac{1}{\tau_r} + \frac{1}{\tau_\Omega}}{\frac{1}{\tau_0}} \tag{1.24}$$

Next, we define the efficiency of the optical antenna, η_{Ant}.

$$\eta_{Ant} = \frac{\frac{1}{\tau_r}}{\frac{1}{\tau_r} + \frac{1}{\tau_\Omega}} \tag{1.25}$$

η_{Ant} quantifies the radiation efficiency of a dipole source coupled to the optical antenna. If a semiconductor with no defects ($\tau_{nr} = \infty$) were used as the source, the quantum

11

efficiency would be equal to the antenna efficiency. Finally, the expressions for quantum efficiency and total recombination rate can be expressed as:

$$QE = \frac{\dfrac{F_p}{\tau_0}\eta_{Ant}}{\dfrac{F_p}{\tau_0} + \dfrac{1}{\tau_{nr}}} \qquad (1.26)$$

$$\Gamma_{tot} = \frac{F_p}{\tau_0} + \frac{1}{\tau_{nr}} \qquad (1.27)$$

Equations (1.26) and (1.27) summarize the exciting potential of using optical antenna enhanced spontaneous emission. For materials that are typically very inefficient light emitters ($\tau_{nr} \ll \tau_0$), an optical antenna can boost their quantum efficiency to a maximum of η_{Ant}. Together, equations (1.26) and (1.27) demonstrate perhaps the more exciting application of creating very fast and highly efficient LEDs.

2 Optical Interconnects

Worldwide demand for data continues to grow at an extreme pace. Total internet traffic is expected to rise at a rate of 23% per year largely due to increased video and mobile demand [10]. By 2019, Internet traffic will reach 168 exabytes (10^{18} bytes) per month. This is in comparison to the mere 5.2 exabytes per month of global Internet traffic in 2007. While consumer demand for greater bandwidth continues to grow, power consumption has emerged as a serious limitation to providing it. Without major breakthroughs in energy efficiency, the power consumption of the network required to provide the Internet with sufficient throughput will quickly get out of hand.
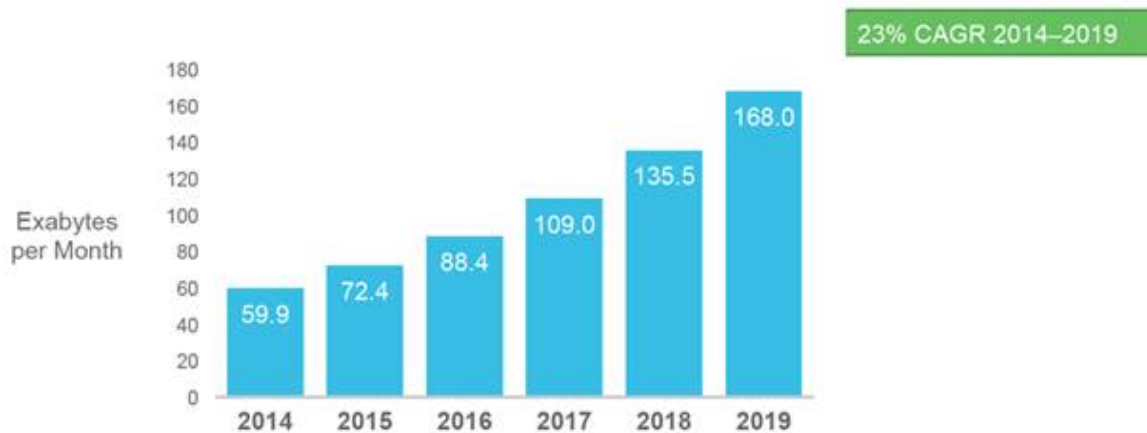
Figure 7. Growth forecast for global internet traffic. It is predicted that traffic will growth at a rate of 23% per year. Reproduced from [10]

The electric power used by data centers already accounted for around 2% of all electricity used in the United States in 2010 [11]. The equivalent of 34 coal-fired power plants (500 MW) were used to supply the electricity necessary to power data centers in the US in 2013. This is expected to rise to 50 power plants by 2020 [12]. Clearly this is not a sustainable trend. In order to overcome this challenge, a more efficient method of communicating data must be developed.

Optical interconnects provide a solution for more efficient data communication. Using optics to transmit data can be significantly favorable to using wires due to the absence of capacitance that must be charged and discharged when transmitting voltage along a wire. The steady change from electrical to optical interconnects has been progressing from long distances (the transatlantic fiber in 1988) to lengths on the order of meters (rack-to-rack optical communication in datacenters) used today. The progression of optics to shorter and shorter length scales is illustrated in Figure 8. If the energy consumption of optical interconnects continues to decrease, the possibility of using light for communication on-chip becomes very real.

Network type	MAN & WAN	LAN	System	Board	Chip
	Metro & long haul	Campus, Enterprises	Intra-rack Inter-rack	Chip-to-chip	On-chip
Distance	Multi-km	10 – 300 m	0.3 – 10 m	0.01 – 0.3 m	<2 cm
Adoption of optical	Since 80s	Since 90s	Since late 00s	After 2012	After 2012
Type of Connectivity	All-optical	Point-to-point and All-optical	Point-to-point	Point-to-point	Point-to-point & all-optical

Figure 8. Optical Interconnect applications for various distances. Reproduced from [13]

2.1 Energy Requirements

Energy consumption in interconnects of microprocessors is estimated to be 50-80% of all power consumed on chip [14], [15]. This energy is expended in the dynamic charging and discharging of the capacitances in the interconnect wires. The capacitance of all on-chip wires is around 2 pF/cm [15]. We can estimate the energy dissipated by an electrical interconnect as:

$$\text{Energy/bit} = C_{wire}V^2 \qquad (2.1)$$

For a 1 V signal transmitting 100 μm, this gives 20 fJ/bit. If we look at the longest wires on a chip, of order 1 cm, the energy cost becomes 2 pJ/bit. In order to provide an advantage over electrical interconnects, an optical link would need to perform significantly better than this. An analysis from [15] suggests that optical links would need to achieve 2-10 fJ/bit to be a viable alternative for on-chip electrical interconnects. Realistically, optical links would never replace all electrical interconnects because very short wires still perform quite well. The benefit of optical interconnects would come when replacing the longest on-chip wires and for connecting chips to nearby chips.

Optical interconnects can transmit data with significantly less energy than wire interconnects. The transmission of light through fibers or waveguides does not suffer from capacitive charging that is required for wires. The minimum energy per bit limitation for optical interconnects comes in the form of signal to noise ratio. For an interconnect to be viable, it must transmit data with a signal to noise ratio such that the bit error rate (BER) does not exceed a value specified by the circuit designer. The BER can vary for particular applications and error correction strategies, but here we will assume a required BER of 10^{-15}. For the ideal case of an optical link with a photodetector that can

detect single photons, the noise limitation will be due to photon shot noise. Shot noise follows a Poisson distribution:

$$P(n) = e^{-M} \cdot \frac{M^n}{n!} \qquad (2.2)$$

where $P(n)$ is the probability of receiving n photons and M is the average number of photons [16]. The rate of errors will be the average probability of detecting a "1" when a "0" is sent and the probability of detection a "0" when a "1" is sent. Since there is no shot noise for sending "0" bits, only the second probability will be non-zero.

$$\text{BER} = \frac{1}{2} e^{-M} \qquad (2.3)$$

We may now conclude the average number of photons per bit necessary for a given BER is:

$$N_{ph} = -\frac{\ln(2 \cdot \text{BER})}{2} \qquad (2.4)$$

where $N_{ph} = M/2$ is the average number of photons per bit including both the "0" and "1" states. For a BER of 10^{-15} this gives 17 photons/bit. If an optical link is used with 1eV photons, the minimum energy per but of the interconnect is only 3 aJ/bit. Giving a little room to work with, we could say an optical link using 100 photons/bit is possible and would consume only 20 aJ/bit. This is a three orders of magnitude decrease in energy consumption when compared to a 100 μm electrical interconnect.

The potential energy advantage of optical interconnects over electrical is clear. Unfortunately, the technology required for such a low-power optical interconnect does not exist. Today's best optical interconnects can operate using around 10,000 photons/bit at the photodetector [16]. Breakthroughs in both the photodetector and light emitter are required for 100 photon/bit communications to become a reality. With high efficiency, low-power, and high speed, the antenna enhanced LED is an excellent candidate for the light emitter in such a low energy optical interconnect.

2.2 Light Emitters

Lasers have completely dominated in practice as the primary light emitter used for optical interconnects. While there are many benefits to using lasers for the emitter, there are also significant drawbacks. This section will compare the benefits and drawbacks for using LEDs and lasers as the emitter in optical interconnects.

The major differentiating benefit that lasers have over LEDs is their modulation speed. Fundamentally, the stimulated emission process driving electron-hole recombination in

lasers follows Fermi's Golden Rule as shown in (1.2). The perturbation driving the transition is cause by the electric field of photons in the laser cavity. As the density of photons increases, the rate of stimulated emission increases. Therefore, the rate of stimulated emission, and the maximum modulation rate of lasers, is proportional to the optical power output of the laser.

We may deduce a similar conclusion by small signal analysis of the laser rate equations. Doing so yields the laser 3dB frequency [1], [17]:

$$f_{3dB} \approx \frac{1.55}{2\pi} \sqrt{\frac{v_g g' S}{\tau_p}} \tag{2.5}$$

where v_g is the photon group velocity, g' is the differential gain coefficient, S is the photon density in the laser cavity, and τ_p is the photon lifetime in the cavity. For an electrically injected device, we find $f_{3dB} \propto \sqrt{I - I_{th}}$ where I is the current and I_{th} is the current required to achieve lasing. Two conclusions may now be drawn regarding lasers: (1) There is always a minimum power required to achieve stimulated emission in lasers, and (2) To achieve a high modulation rate, the laser must be operated above this minimum threshold. While lasers have been demonstrated with modulation rates up to 50 GHz, the potential for extremely low-power optical communications in the 100 photon/bit energy range does not exist due to the fundamental limitations of stimulated emission.

LEDs typically suffer from a low modulation rate due to spontaneous emission lifetimes on the order of 1 ns. However, as this dissertation will show, the spontaneous emission rate can be greatly enhanced by coupling the semiconductor to an optical antenna. Small signal analysis of the LED rate equations yield a 3dB frequency:

$$f_{3dB} = \frac{1}{2\pi\tau_{sp}} \tag{2.6}$$

The spontaneous emission lifetime leads to a maximum modulation rate of around 250 MHz in LEDs. If the spontaneous emission rate could be enhanced using an optical antenna by a factor of 200x, LEDs would be competitive with the 50 GHz modulation rate of the fastest lasers.

In addition, it is also important to look at how the modulation rate of LEDs depends on input power. A 100 photon/bit interconnect would require high speed even at very low power operation. The carrier recombination rate equation in an LED is:

$$\frac{dn}{dt} = \frac{n}{\tau_{nr}} + Bnp + Cn^3 \tag{2.7}$$

16

where n is the electron density, p is the hole density, τ_{nr} is the non-radiative lifetime due to Shockley-Read-Hall recombination, B is the bimolecular recombination coefficient responsible for spontaneous emission, and C is the Auger recombination coefficient. For simplicity, we will make the assumption that the device is very efficient and the contribution from non-radiative recombination can be ignored. The LED will be operated at very low power so we will also neglect the contribution of Auger recombination. The active region may also be p-doped, so the hole density can be taken as a constant. In this case we may introduce a spontaneous emission lifetime as $\tau_{sp} = 1/Bp$ and the rate equation simplifies to:

$$\frac{dn}{dt} = \frac{n}{\tau_{sp}} \tag{2.8}$$

The recombination lifetime for the LED is a constant, τ_{sp}, which yields the maximum modulation rate given in (2.6). Notice that the modulation rate contains no dependence on the carrier concentration or photon density, as is the case for the laser. Therefore, even at extremely low power operation, the LED can achieve its maximum modulation rate.

Other considerations for the light emitter in an optical interconnect include waveguide or fiber coupling, data propagation, and device size. Single mode lasers are presently used in Silicon Photonics for optical transceivers. Single mode operation is important to minimize differential group delay, which can limit the maximum attainable bandwidth for longer distance interconnects. Single mode operation of conventional LEDs is not possible due to the large area of incoherent emission. However, antenna enhanced LEDs are nanoscale devices and will emit radiation from a single spatial mode that can be efficiently coupled to an optical waveguide [18]. While the broadband spectrum emitted by LEDs will lead to some dispersion in the waveguide mode, this is not expected to limit the modulation bandwidth for the few centimeter length scale of these interconnects. Finally, antenna enhanced LEDs are fundamentally on the order of the wavelength of light emission in size. Therefore these devices are only 100s of nanometers in size allowing for compact integration for on-chip optical interconnects.

In conclusion, the antenna enhanced LED can be a viable emitter for short-range optical interconnects. High-speed data communication at extremely low power is achievable with antenna enhanced LEDs, and cannot be achieved by lasers due to the fundamental limitations of stimulated emission. While developing and integrating an efficient antenna enhanced LED will prove a challenge, the potential to make the required emitter for 100 photon/bit optical communications is possible.

3 Circuit Model for Optical Antennas

Antenna enhanced spontaneous emission has so far been described using two different methods. The first approach utilized the radiation resistance of antennas to estimate the enhancement that an antenna can provide. While illustrating the concept of antenna enhanced spontaneous emission, this approach failed to properly account for the resonant behavior of antennas or to estimate the achievable efficiency. The second method utilized the Purcell factor to describe the enhancement in terms of quality factor and mode volume. The Purcell approach fails to adequately describe the enhancement because mode volume is not well defined for antennas and cannot be calculated in a straightforward manner for arbitrary antenna geometries. To more completely understand antenna enhanced spontaneous emission, a complete circuit model will be developed in this section.

3.1 RLC Circuit

Any piece of metal is a resonator with a characteristic resonant frequency and quality factor. This resonance comes from the fact that any piece of metal will have some capacitance and inductance associated with an oscillation between electric and magnetic fields. The resonant frequency of the piece of metal will be $\omega_0 = 1/\sqrt{LC}$. When provided with an excitation at ω_0, the energy in the piece of metal will decay either as ohmic loss or radiation. These loss mechanisms may be treated as a resistance, R. The quality factor may then be found as $Q = \omega_0 L/R$. By defining a point in space with which to measure voltage and current, we may extract the quantities R, L and C. Knowing these components gives a complete description of the resonance of the piece of metal in question. We may therefore construct the RLC circuit in Figure 9 to describe an optical antenna used for spontaneous emission enhancement. Throughout this section we will focus on the fundamental mode (lowest frequency resonance) of the antenna. For a dipole antenna this corresponds to the oscillation of charge at each of its ends. In general, the same approach can be taken to analyze higher order modes as well.
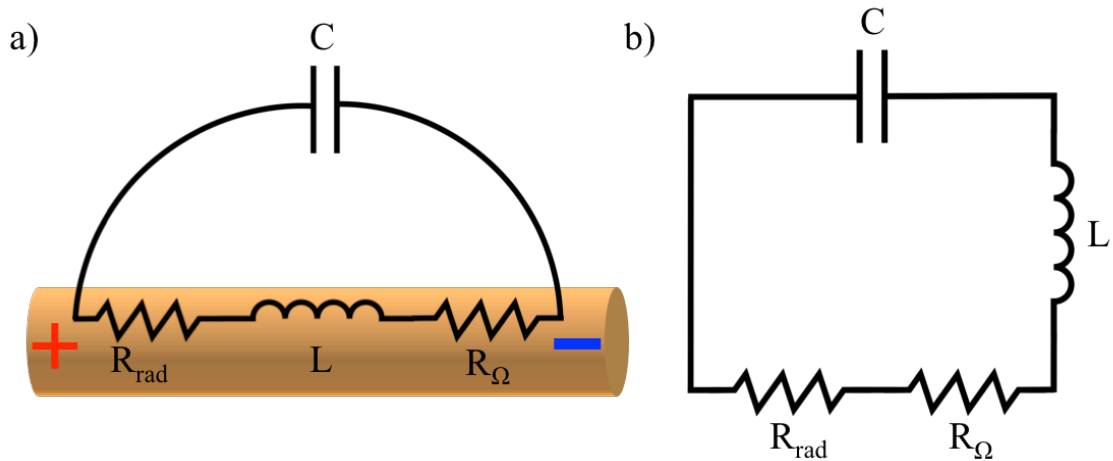
Figure 9. Circuit model for fundamental resonance of an antenna. a) Circuit model overlaying antenna. Fundamental mode has charge located at each end of the antenna. b) Circuit diagram for antenna resonance.

The circuit in Figure 9 describes the fundamental resonance of a straight wire, but this geometry does not couple well to a dipole source unless there is a feedgap. Adding a feedgap will change the resonance of the antenna due to the extra capacitance of a small gap between two metals. As the gap in the antenna increases, one would expect the resonant frequency to increase due to lower capacitance. If the two halves are separated even further, the two halves of the antenna will eventually be entirely decoupled and the resonant frequency will be twice that of the antenna with no gap. The effects of a feedgap on the resonant properties of the dipole antenna can be modeled using the circuit in Figure 10.
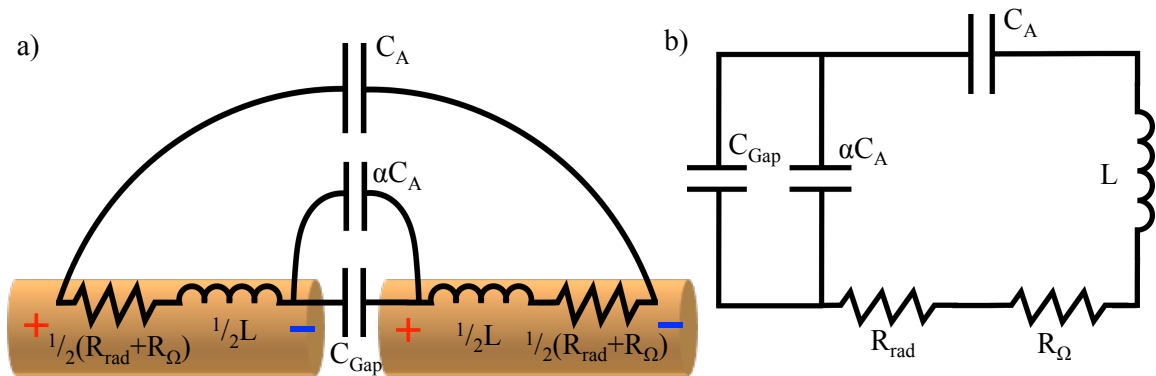
Figure 10. Circuit Model for dipole antenna with a feedgap. a) Circuit overalying antenna geometry. Charge accumulates at the ends of each section of metal at resonance. b) Circuit diagram for the dipole antenna with a feedgap.

The circuit diagram in Figure 10 includes the capacitance due to the parallel capacitor created by the feedgap, C_{Gap}. It also includes a term to account for the fringe fields around the feedgap, αC_A. Here, α is a term to account for the strength of the fringing

capacitance in terms of the main antenna capacitance C_A. α has been found to be near unity for small antenna gaps (gap distance less than the wire radius). As the gap size decreases, the gap capacitance, $C_{Gap} = \epsilon_r \epsilon_0 A/d$, will increase. A large C_{Gap} will essentially short the antenna for very narrow gap due to the low gap impedance, $Z_C = 1/j\omega C$. In this case, the circuit diagram in Figure 10b will converge to that of the simple wire antenna in Figure 9b.

The inductance and capacitance used in the circuit model will depend on the geometry of the antenna used. For the simple cases of a dipole with or without a feedgap, these circuit parameters can be estimated using the inductance and capacitance of a wire.

Gap Capacitance	$C_{Gap} = \dfrac{\epsilon_0 \epsilon_g A}{d}$
Faraday Inductance [19]	$L_f = \dfrac{\mu_0 \ell}{\pi^2} \ln\left(\dfrac{\ell}{r}\right)$
Antenna Capacitance [19]	$C_A = \dfrac{\epsilon_0 \epsilon_A \ell}{\ln\left(\dfrac{\ell}{r}\right)}$
Radiation Resistance	$R_{rad} = \dfrac{\pi}{6} Z_0 \left(\dfrac{\ell}{\lambda}\right)^2$

Figure 11. Circuit model components of a dipole antenna. The gap of the antenna contains material with permittivity ϵ_g. The antenna is embedded in an environment with permittivity ϵ_A.
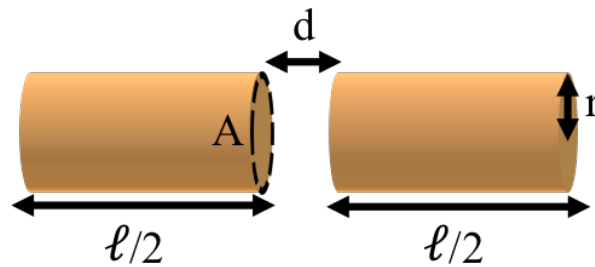
Figure 12. Physical dimensions used to characterize the dipole antenna

With the antenna capacitance and inductance given as functions of the antenna's geometry given in Figure 11, we may now analyze the resonant frequency of the dipole antenna using the circuit diagram in Figure 10. The simplest case to analyze is when the antenna has no gap. In this situation, the gap is shorted and the circuit diagram reduces to Figure 9b.

$$\omega_0 = \frac{1}{\sqrt{LC}} = \frac{1}{\sqrt{L_f C_A}} = \frac{1}{\sqrt{\dfrac{\epsilon_0 \epsilon_A \mu_0 \ell^2}{\pi^2}}} = \frac{c\pi}{\ell n_A} \tag{3.1}$$

$$\ell = \frac{c\pi}{\omega_0 n_A} = \frac{\lambda}{2 n_A}$$

As expected, the length of a dipole antenna with no gap is a half-wavelength. The resonant frequency for the dipole antenna with a gap becomes a more complicated function of the dipole antenna geometry.

$$\omega_0 = \frac{1}{\sqrt{LC}} = \frac{\sqrt{1 + \alpha + C_{Gap}/C_A}}{\sqrt{L_f C_A (\alpha + C_{Gap}/C_A)}} = \frac{c\pi}{\ell n_A} \sqrt{\frac{\left(1 + \alpha + \dfrac{A \ln\left(\frac{\ell}{r}\right) \epsilon_g}{d\ell \epsilon_A}\right)}{\left(\alpha + \dfrac{A \ln\left(\frac{\ell}{r}\right) \epsilon_g}{d\ell \epsilon_A}\right)}} \tag{3.2}$$

$$\ell = \frac{\lambda}{2 n_A} \sqrt{\frac{\left(1 + \alpha + \dfrac{A \ln\left(\frac{\ell}{r}\right) \epsilon_g}{d\ell \epsilon_A}\right)}{\left(\alpha + \dfrac{A \ln\left(\frac{\ell}{r}\right) \epsilon_g}{d\ell \epsilon_A}\right)}} \tag{3.3}$$

The dependence of the resonant frequency on the size of the gap, d, is seen in (3.5). When d is small, the square root term will converge to one and the resonant frequency is equivalent to the case with no gap. When d becomes large, the resonant frequency increases. As stated earlier, the model given here begins to break down as d becomes much greater than r due to the slight dependence of α on those terms.
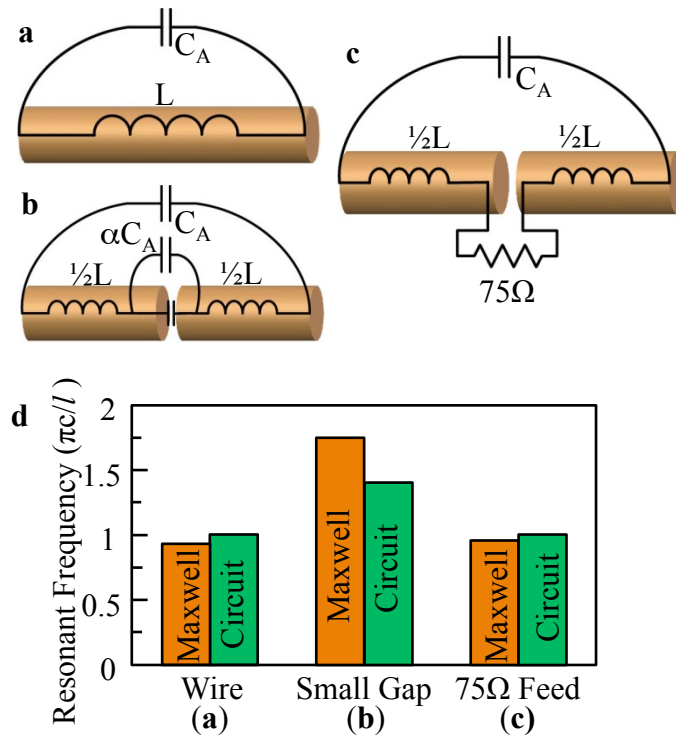
Figure 13. Comparison of resonant frequency using the antenna circuit model and full FDTD Maxwell solver.

The impedance of the feedgap is crucial in determining how various sources can couple to the antenna. In RF applications it is normal to connect the antenna feedgap to a 75 Ω transmission line. For coupling to a dipole source, the feedgap impedance should very high. The effect of various antenna feedgap terminations on the resonance of the antenna is shown in Figure 13. For each case, the resonance was analyzed using the circuit model and by using an FDTD Maxwell simulator. The circuit model predicts the shift in resonant frequency for different feedgap impedances with reasonably low error.

3.2 Kinetic Inductance

In the RF regime, the antenna capacitance and inductance for a given antenna do not depend on the metal material used. The capacitance and inductance of the antenna are only dependent on geometry due to their origin in the electric and magnetic fields outside the metallic structure. This picture of antennas breaks down at optical frequencies. At very high frequencies, electrons in metals are not able to respond exactly in phase with the optical field. A phase shift between electric field and electron motion arises from the fact that the electrons have mass and therefore inertia. Equivalently, this effect may be treated as an added inductance in the antenna. A similar effect has been observed in superconductors, and is named Kinetic Inductance.

The impact of kinetic inductance on optical antennas can be quantitatively included in the optical antenna circuit model by adding an additional inductance. The complex permittivity of a metal is sufficient to completely describe the ohmic loss and kinetic inductance in that material. For metals, the Drude model can be used to relate physical material parameters to the complex permittivity.

$$\epsilon_m = \epsilon_\infty - \frac{\omega_p^2}{\omega(\omega + j\gamma_c)} \tag{3.4}$$

where ϵ_∞ is the permittivity at infinite frequency due to bound electrons, ω_p is the plasma frequency, and γ_c is the electron collision frequency. The Drude model given in (3.7) relies on only three parameters and gives a good fit for most metals in the visible and near-infrared regime. For materials that contain absorption bands in the frequency regime of interest a multi-oscillator model will be required.

The permittivity at optical frequencies has been experimentally determined for a variety of materials in the literature. However, it will be more convenient to include the material properties in the circuit model through a real and imaginary impedance. To do so requires conversion of complex permittivity to complex conductivity, σ. The relationship between the two is seen from Ampere's Law. In the microscopic picture, only current density, J, and charge density, ρ, describe the physical situation with no need for relative permittivity, ϵ_m. In the macroscopic picture, the complicated situation of currents and charge density inside a material are all lumped into a relative permittivity. Using the definition of conductivity, $\sigma = J/E$, gives a comparison of the two pictures of Ampere's Law.

$$\nabla \times H = \sigma E + j\omega\epsilon_0 E \tag{3.5}$$

$$\nabla \times H = j\omega\epsilon_0\epsilon_m E \tag{3.6}$$

Recognizing that (3.8) and (3.10) must be equivalent yields the desired relationship between conductivity and permittivity.

$$\sigma = j\omega\epsilon_0(\epsilon_m - 1) \tag{3.7}$$

Since we will want to work with impedances, it is useful to convert the complex conductivity to a resistivity[20].

$$\rho = \frac{1}{\sigma} = \frac{1}{j\omega\epsilon_0(\epsilon_m - 1)} \tag{3.8}$$

Now, we may convert the complex resistivity into impedance $Z = R_\Omega + j\omega L_K = \rho\ell/A$, where ℓ is the length of the metal and A is the cross sectional area. The real part of this

impedance is the ohmic loss resistance, R_Ω. The imaginary portion of this impedance is the impedance due to kinetic inductance, L_K.

$$R_\Omega = \text{Re}\{Z\} = \frac{\text{Re}\{\rho\}\ell}{A} = \frac{\epsilon_m''}{\epsilon_0\omega\big((1-\epsilon_m')^2 + \epsilon_m''^2\big)}\left(\frac{\ell}{A}\right) \qquad (3.9)$$

$$L_K = \frac{\text{Im}\{Z\}}{\omega} = \frac{\text{Im}\{\rho\}\ell}{\omega A} = \frac{(1-\epsilon_m')}{\epsilon_0\omega^2\big((1-\epsilon_m')^2 + \epsilon_m''^2\big)}\left(\frac{\ell}{A}\right) \qquad (3.10)$$

where the metal permittivity has been divided into its real and imaginary parts such that $\epsilon_m = \epsilon_m' - j\epsilon_m''$. The conversions given by (3.9) and (3.10) allow any piece of material to be characterized by circuit components $R, L,$ and C. Metals, which have negative ϵ', will correspond to an inductance. Dielectrics, which have positive ϵ', correspond to a capacitance. Materials that have loss, a non-zero ϵ'', will include a resistance.

Upon examination of (3.10), we see that the kinetic inductance will become large as ϵ_m' approaches one. This occurs near the plasma frequency where the material transitions from a metal to a dielectric. The field of plasmonics essentially operates in this regime where kinetic inductance is dominant. In fact, both plasmonic devices and optical antennas can be described using circuit models. Moving forward, the kinetic inductance will be simply added in series to the magnetic field inductance, L_f, so that the total inductance in the antenna is $L = L_f + L_K$.

3.3 Coupling Sources to Antennas

A dipole source placed in the feedgap of an antenna will induce current into the arms of the antenna. These currents drive the RLC circuit described in the previous section producing radiation and heat. As described by equation (1.13), Ramo's theorem can be used to calculate the magnitude of current induced in the antenna by the dipole source. As the gap of the antenna decreases, the induced current increases. Current coupling can be included in a circuit model for optical antenna enhanced spontaneous emission by including a current source with magnitude $I_0 = q\omega x_0/d$.
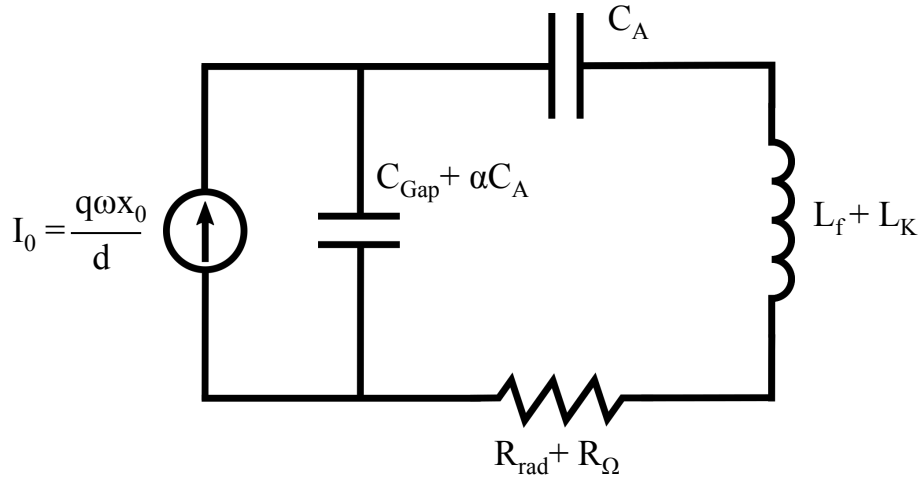
Figure 14. Antenna circuit model including coupling to a dipole source

The capacitance of fringing fields, αC_A, and the gap capacitance, C_{Gap}, appear in parallel to the current source. These capacitances have impedance that essentially shorts the source. For example, if the antenna did not have a gap, the driving source would have no voltage across it and would not induce current into the antenna. This effect highlights the importance of considering the gap impedance when designing an optical antenna. The impedance of the dipole sources used for spontaneous emission enhancement can be estimated as $|Z| = Z_0 \lambda / 2\pi x_0$, which is on the order of 10^5 Ω. Therefore, the gap impedance of the antenna needs to be very high. As a comparison, a 10 nm gap consisting of a wire with 20 nm radius operating at $\lambda = 1000$ nm will have an impedance of only 477 Ω. If the gap is filled with a semiconductor of index $n = 3.5$, the same size gap now only has an impedance of 39 Ω. The shorting of the dipole source will ultimately limit the amount of spontaneous emission enhancement achievable for the structure in Figure 10. The induced current increases as the gap size decreases, but this benefit is countered by the decrease in gap impedance.

To overcome the limitations that the gap impedance puts on sponteneous emission enhancement, one must change the geometry near the feedgap of the antenna. The strategy employed is essentially the same as including an impedance matching network in an RF antenna design. However, in this case we would like the source to see as high an impedance as possible. To do this, either we can attempt to reduce the gap capacitance or we can add inductance to make a resonant matching circuit.
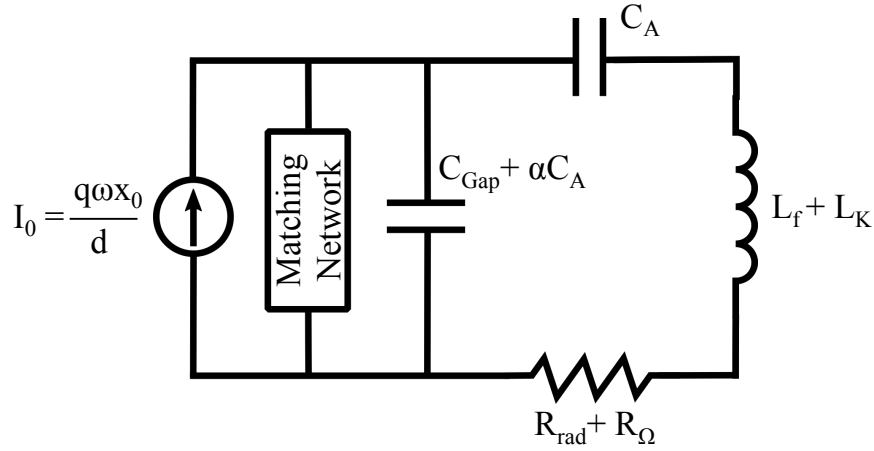
Figure 15. Antenna circuit model with a matching network. An inductance at the feedgap of the antenna can be utilized to decrease shorting of the dipole source current that occurs when C_{Gap} is large.

The capacitance of the gap can be controlled through the exact geometry at the gap of the antenna. Up to this point, it has been assumed that the feed gap in the antenna consist of two flat electrodes. This is actually a very unfavorable situation due to the large capacitance of the parallel plate geometry. The capacitance of the same size antenna gap can be reduced by rounding the electrode tips. The rounded gap capacitance can be estimated as:

$$C_{Gap} = \frac{\pi \epsilon_g r}{2} \left(\ln \left(\frac{r}{d} \right) + 2\gamma \right) \tag{3.11}$$

where r is the radius of the tips and γ is Euler's constant [21]. The depedance of gap capacitance on gap spacing given for rounded tips only increases logarithmically. The reduction in gap capacitance leads to less current being shunted and therefore a larger enhancement for the same antenna gap. Alternatively, adding an inductance near the antenna gap allows one to control the gap impedance as a function of frequency. Extra inductance can be achieved by adding a small arch around the gap of the antenna. By changing the size of the arch used, the impedance of the gap can be controlled.

3.4 Losses in Optical Antennas

In order to estimate the achievable efficiency that optical antennas can obtain, we must understand the various sources of loss. The antenna circuit model so far contains two resistances. Power dissipated in R_{rad} corresponds to power radiated while power dissipated in R_Ω corresponds to ohmic loss in the antenna. These two loss mechanisms sufficiently describe the fundamental mode of the antenna.

However, when a dipole source is brought very close to an antenna or is placed in the gap of an antenna, it does not only excite the fundamental mode of the antenna. The dipole source generates a field profile that is very tightly confined. The confinement of the fields

26

near the source results in confined currents induced on the antenna electrodes. As current flows away from the tips of the antenna, it spreads out. This current spreading results in additional ohmic losses that were not accounted for in the antenna mode.

The electric field profiles in Figure 16 show the contrasting situations of exciting the antenna with a plane-wave and exciting with a dipole in the feedgap. Plane-wave excitation results in the field distribution corresponding to the antenna mode, which has a very uniform electric field in the gap. Dipole excitation results in additional fields that are tightly confined to the gap of the antenna.
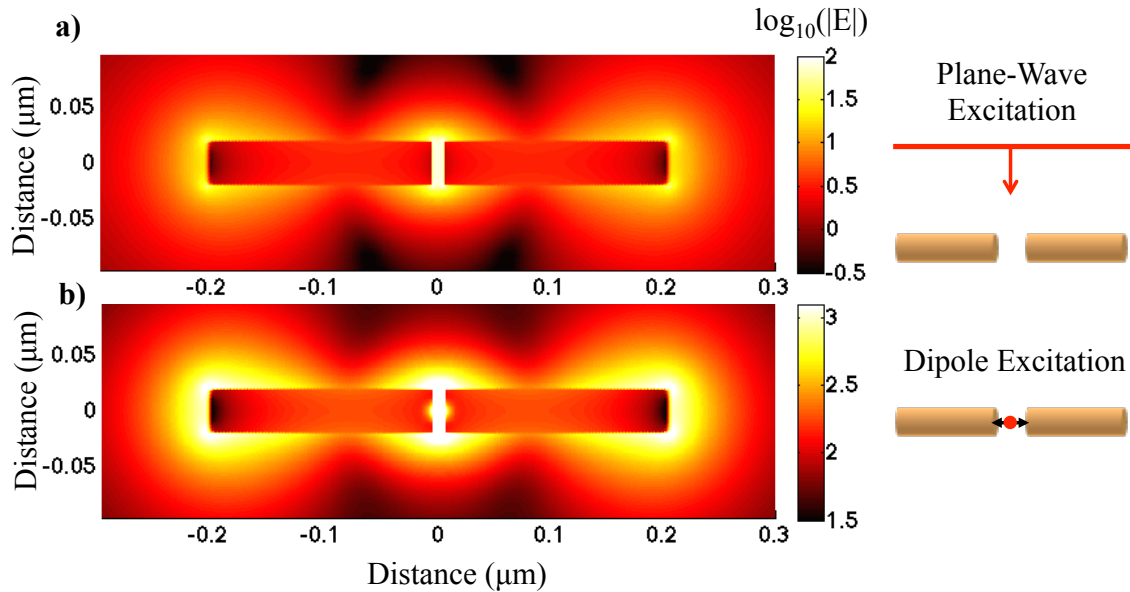
Figure 16. a) Electric field profile for an optical antenna excited by an incoming plane wave. The fundamental antenna mode has a uniform field distribution in the feedgap. b) Electric field profile for optical antenna excited by a dipole placed in the feedgap. Near the dipole the tightly confined field distribution results in additional ohmic loss. These losses can be included in a circuit model through a spreading resistance, R_{spread}.

The resistance due to current spreading can be estimated by treating the induced currents on the antenna tips as a point contact of size βa, where a is the distance between the metal and dipole source and β is a factor related to the geometry of the antenna tips. Figure 17 shows this geometry of spreading resistance near the antenna gap, which corresponds to the situation in Figure 16b.
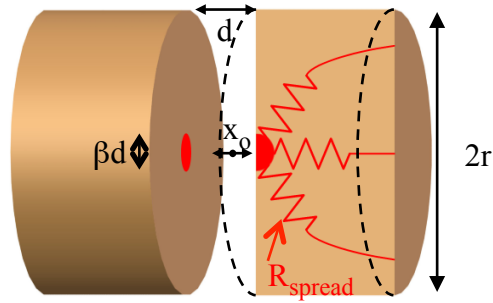
Figure 17. Diagram of dipole induced spreading resistance. Dipole excitation of an antenna results in additional loss that is not inherent to the fundamental antenna mode.

The field confinement that corresponds to spreading resistance can easily be seen in simulations by bringing a dipole near a metal surface. Electric field profiles for a dipole source 10, 5, 2 and 1 nm away from a metal surface a shown in Figure 18. The electric field been normalized to the maximum field in the metal for each case. The fields become more confined laterally as the dipole approaches the metal surface, which results in increased spreading resistance.
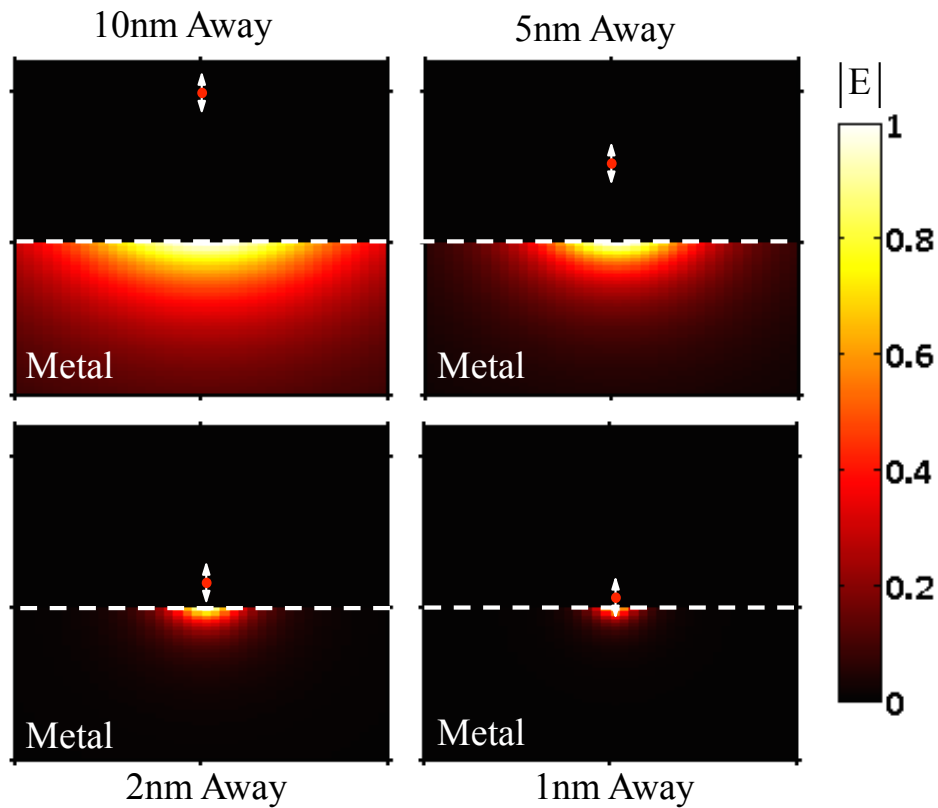
Figure 18. Electric field profile in a metal as the dipole source approaches. In each case the field is normalized to the maximum field inside the metal. The induced current is confined to a smaller lateral dimension as the dipole nears the interface.

If the dipole is always placed in the center of the antenna gap, the contact size will decrease as the gap size decreases. The spreading resistance may then be taken as:

$$R_{spread} = \frac{\text{Re}\{\rho\}}{\beta d}$$

(3.12)

where ρ is the complex resistivity defined in (3.8). The additional loss resistance, R_{spread}, is not related to the losses in the fundamental antenna mode. Therefore this loss term is not included in the resonating portion of the circuit in Figure 14. Instead, R_{spread} is added directly in series with the driving current, I_0. Including the spreading resistance leads to the final form of the antenna circuit model as shown in Figure 19.
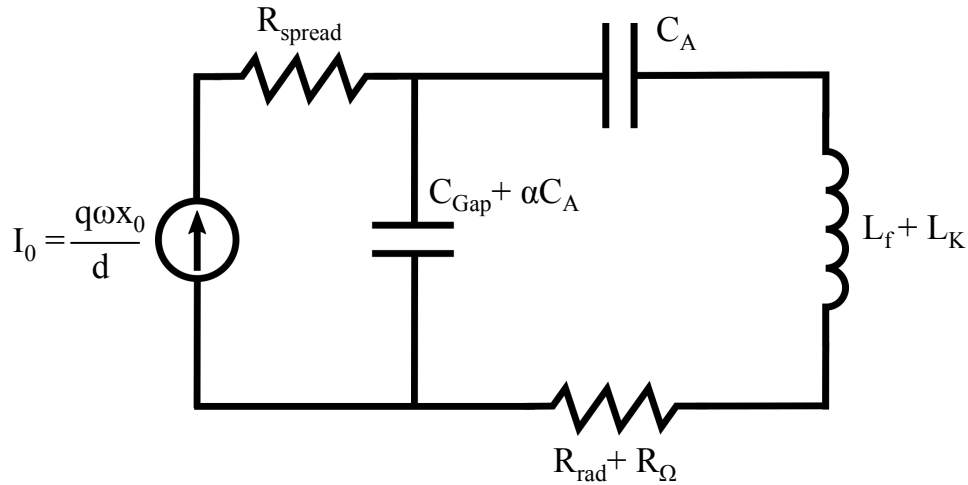
Figure 19. Complete antenna circuit model for spontaneous emission enhancement. R_{spread} accounts for losses due to currents confined to a small cross sectional area very near the dipole source.

The ideal situation of locating a dipole source directly in the center of the antenna gap is not always practical. When the dipole is offset from the center, equation (3.12) no longer adequately describes loss due to spreading currents near the dipole source. Neglected in the above analysis is the distribution of induced charges on the antenna electrodes. As the light emitter oscillates over a distance, x_0, the charges on the nearby electrode respond by bunching and spreading. This redistribution of charge on the electrode's surface is current that results in losses via the previously discussed spreading resistance. None of this "dead-sheet" current oscillates in the antenna mode and therefore does not radiate. It can be shown that the magnitude of the "dead-sheet" current is proportional to the distance, a, between the light emitter and the electrode of interest, which gives $I_{dead} \approx q\omega x_0/a$. It is important to note that while the current that results in radiation, I_0, depends only on the total size of the antenna gap, the useless current, I_{dead}, increases as the emitter nears one of the antenna electrodes. Taking I_{dead} into account results in a greater amount of power dissipated by the resistance near the antenna electrode surface, R_{spread}. Therefore, we

can include this effect in the Figure 19 circuit by increasing R_{spread} by approximately the factor $(d/a)^2$ while driving the circuit with the antenna current, I_0.

An alternative description of the losses due to current spreading considers that the dipole source couples to modes other than the fundamental antenna mode. There are an infinite number of off-resonant modes that exist at the metal-dielectric boundary. These modes vary based on the exact geometry of the antenna used, but they are most strongly excited at the metal interface closest to the dipole source. These modes also have the common distinction that they do not radiate. Therefore, the excitation of these modes near the dipole is another source of ohmic loss. It is possible to analytically solve for the contribution of each of these surface modes for a simple antenna geometry [22]. However, for our purposes it is more useful to estimate the degree to which these modes contribute to ohmic loss by lumping them into a single resistance that can be included for any antenna geometry.

3.5 Anomalous Skin Effect

Losses in metals occur when electrons in the metal lose their energy through scattering processes. The rate at which electrons scatter was represented by γ_c in the Drude model for the material's permittivity. For bulk metals at low frequency, this picture adequately represents the loss. However, if the electric field skin depth approaches that of the mean free path of electrons in the metal, the bulk electron collision properties of the metal no longer apply. This is exactly the situation that arises when a dipole becomes very near the tips of an optical antenna.
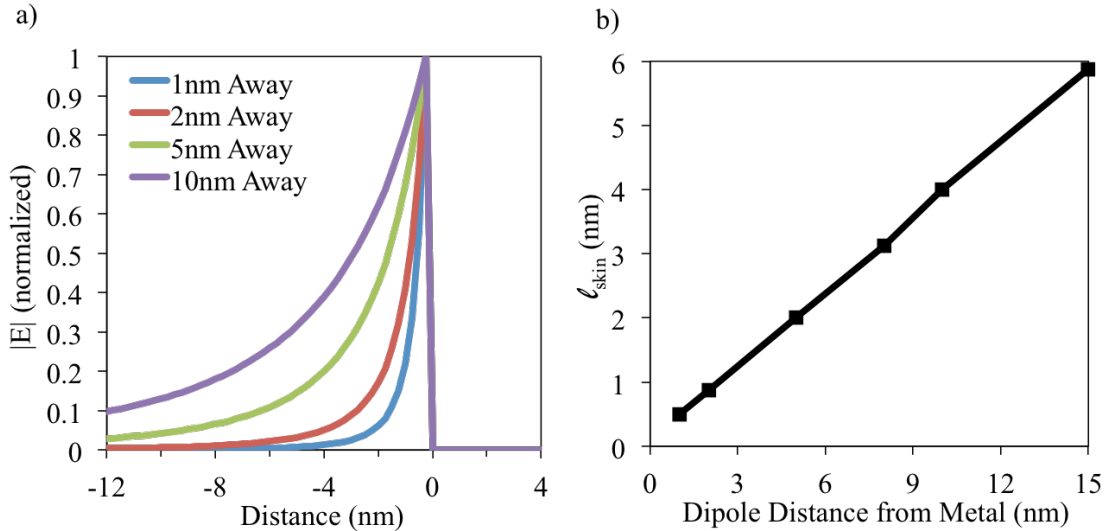
Figure 20. a) Electric field profile inside the metal due to a dipole located various distances from the metal interface. The field is set to zero outside the metal for clarity. b) The skin depth of fields contributing to spreading resistance as a function of the distance between the dipole source and metal interface.

In this regime, the anomalous skin effect becomes important as electrons suffer collisions more frequently. Due to the nonlocal nature of the anomalous skin effect, it is not taken into account in standard FDTD/FEM optical simulations. The anomalous skin effect was originally studied at low temperatures where the mean free path of electrons is long in order to describe the surprisingly large absorptivity of metals in this regime [23][24], [25]. This additional loss mechanism can be described as follows.

(1) An electron within the skin depth of an applied field gains energy from the field.
(2) The energized electron propagates out of the skin depth region.
(3) The energy carried by the electron can no longer interact with the field, so it is lost. The skin depth can therefore be thought of as an effective scattering barrier.

In addition, electrons within the skin depth region can collide with the metal surface. A graphic of these two types of collisions is shown in Figure 21. In practice, electron surface collisions will be diffuse and result in energy loss. It may be possible to have specular reflection of electrons, but this would require perfect single crystal facets at the metal surface.

A method of including these additional collisions is to use the Drude model with modified electron collision frequency. Kreibig used this approach to account for the increased rate of surface collisions in small Ag particles by adding a $A v_F / R$ term to the bulk collision frequency, where A is a constant close to 1, v_F is the electron Fermi velocity, and R is the radius of the metal particle [26]. Gilberd [27] and Holstein [28] used a similar approach to estimate the increased optical absorptivity of metals under the assumption of the collisionless skin depth, c/ω_p. We adopt the same strategy by modifying the average rate of electron collisions, γ_c, by equation (3.13), where ℓ_{mfp} is the mean free path of electrons, ℓ_{skin} is the skin depth, and δ is a coefficient to account for the exact nonlocal treatment of these effects. The quantity v_F / ℓ_{mfp} is the metal's bulk collision rate. The collision rate given by (3.13) is valid as long as the thickness of metal used is greater than the skin depth. If this is not the case, ℓ_{skin} is replaced by the metal thickness.

$$\gamma_c = \frac{v_F}{\ell_{mfp}} + \frac{v_F}{\delta \ell_{skin}} \tag{3.13}$$

The modified electron collision rate is substituted into (3.14), a Drude model for complex permittivity, where ϵ_∞ is the background permittivity due to bound electrons, ω_p is the plasma frequency, and ω is the frequency.

$$\epsilon_m = \epsilon_\infty - \frac{\omega_p^2}{\omega(\omega + i\gamma_c)} \tag{3.14}$$

The optical frequency resistivity can then be found as $\rho = \text{Im}\{1/\omega\epsilon_0(1 - \epsilon_m)\}$. In terms of the bulk resistivity, ρ_0, the modified collision resistivity becomes $\rho_{ASE} = \rho_0(1 + \ell_{mfp}/\delta\ell_{skin})$. This new resistivity can be used to analyze the losses in metal structures.
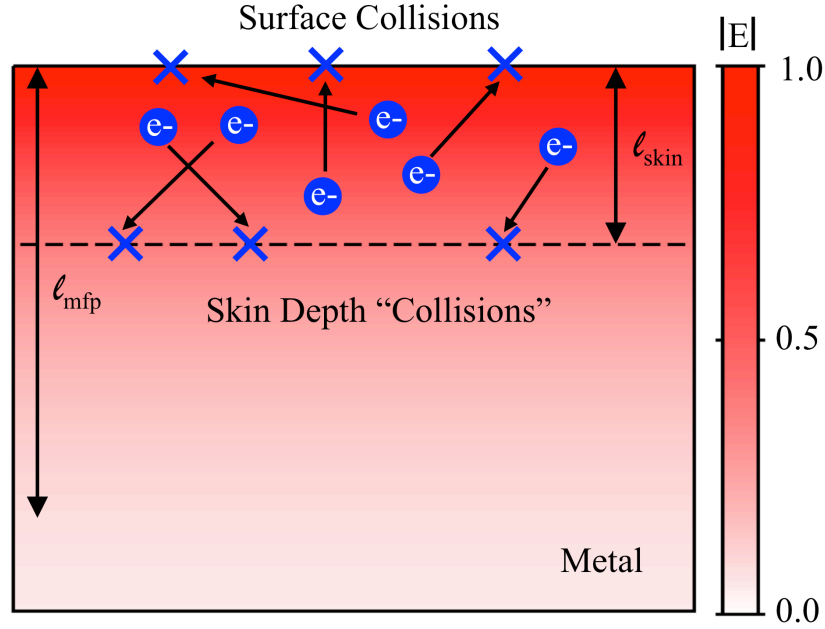
Figure 21. Electron collisions with the metal surface and the skin depth (anomalous skin effect) decrease the effective mean free path of electrons. The additional rate of electron collisions leads to higher loss and reduced antenna efficiency.

Following equation (3.13), the increased collision rates can be modeled by modifying the resistivity by the factor $(1 + \ell_{mfp}/\delta\ell_{skin})$. This treatment would suffice if the true bulk mean free path of electrons at optical frequencies were known, but all optical measurements of the complex permittivity of Au and Ag also suffer from a skin depth on the order of the mean free path. The additional loss due to the anomalous skin effect is convolved with the heavily cited optical constants published by Johnson and Christy [29] and Palik [30]. In fact, the neglect of the anomalous skin effect is acknowledged as a possible source of error in Palik's handbook. Therefore, we include an additional term in the resistance adjustment, shown in equation (3.15), to account for the skin depth at which the optical constants were measured, $\ell_{skinMeas}$.

$$R_{ASE} = R_0 \left(1 - \frac{\ell_{mfp}}{\delta\ell_{skinMeas}} + \frac{\ell_{mfp}}{\delta\ell_{skin}} \right) \qquad (3.15)$$

A number of other models have been presented to address the impact of nonlocal effects in nanoscale metal structures [31]–[33]. All of these models predict that metal losses increase substantially as the dimensions of the problem (size of metal particle or ℓ_{skin}) are reduced below ℓ_{mfp}. These nonlocal models are inherently complex and it is not

32

straightforward to apply them to arbitrary 3-D antenna geometries. Our methodology allows for the simple introduction of nonlocal loss effects for any antenna geometry through the resistances of the circuit model in Figure 19. One is then able to get more realistic estimates of loss than in standard FDTD/FEM simulation. The omission of these losses in simulation of optical antennas will always lead to artificially high claims of optical efficiency.
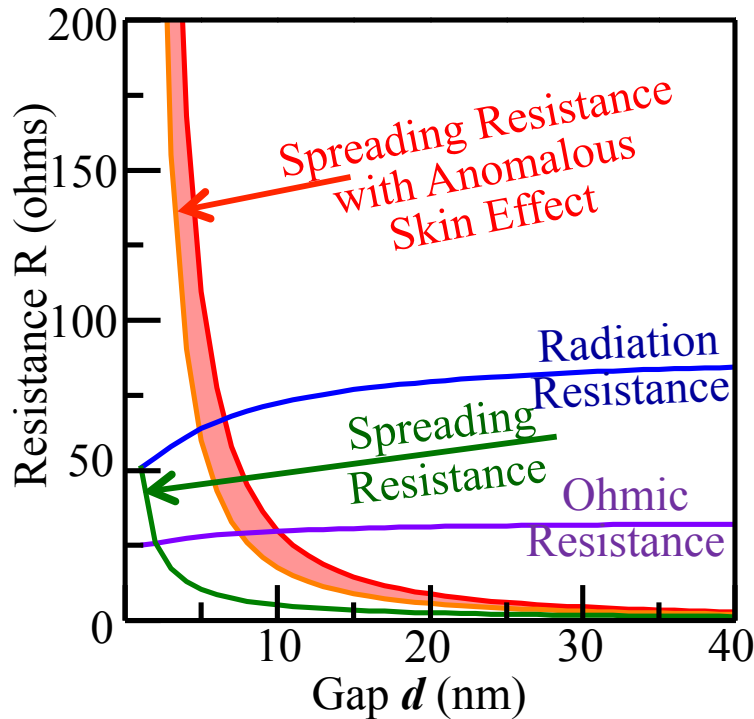
Figure 22. Resistances in optical antennas. Power dissipated in the radiation resistance leads to light emission while power dissipated in the ohmic resistance and spreading resistance goes into heat. The anomalous skin effect significantly increases spreading resistance losses for small gaps.

To get an idea of how harmful the spreading resistance an anomalous skin effect can be, we can compare the magnitude of the various antenna resistances as a function of gap spacing. For large antenna gaps, the antenna can be quite efficient due to a large radiation resistance compared to the ohmic losses in the antenna mode. However, below 10 nm gaps the spreading resistance begins to dominate as shown in Figure 22. Since the skin depth is reduced below the mean free path of electrons in this regime, the anomalous skin effect dominates and the spreading resistance becomes many times greater than radiation resistance.

3.6 Enhancement and Efficiency

The circuit model that has been presented in this section is intended to give insight into the limits of efficient optical antenna enhanced spontaneous emission. The complete circuit model in Figure 23 can now be used to derive expressions for spontaneous emission enhancement and efficiency. The spontaneous emission enhancement is given by the rate that a dipole source produces photons when coupled to the optical antenna compared to when it is in homogenous material. This is equivalent to the ratio of power dissipated in the antenna radiation resistance of Figure 23 to the power dissipated in the dipole radiation resistance of Figure 2.

$$\text{Enhancement} = \frac{\frac{1}{\tau_r}}{\frac{1}{\tau_0}} = \frac{P_{rad}}{P_0} \tag{3.16}$$

The antenna efficiency, η_{Ant}, can be determined using the circuit model by taking the ratio of power dissipated in the radiation resistance to the total power dissipated by the dipole source.

$$\eta_{Ant} = \frac{\frac{1}{\tau_r}}{\frac{1}{\tau_r} + \frac{1}{\tau_\Omega} + \frac{1}{\tau_{spread}}} = \frac{P_{rad}}{P_{rad} + P_\Omega + P_{spread}} \tag{3.17}$$

The efficiency given here is similar to that given by (1.25) in the earlier discussion of antenna efficiency, but the additional losses from spreading resistance are included.
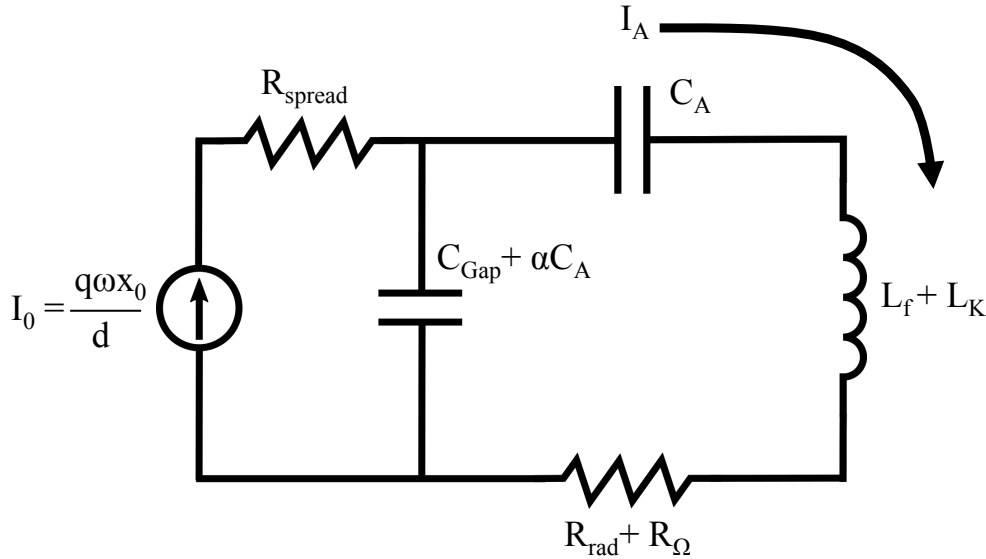
Figure 23. Full optical antenna circuit model. I_A represents current that flowing in the fundamental mode of the antenna.

To calculate P_{rad}, we must first derive an expression for the current that flows in the antenna mode, I_A. To do so, it will be useful to use the quality factor, Q, of the antenna. By neglecting the current source, we can analyze the circuit model to get the frequency and Q of the antenna resonance:

$$\omega_0 = \frac{1}{\sqrt{L_{tot}C_{tot}}} = \frac{1}{\sqrt{(L_f + L_K)C_A}}\sqrt{\frac{1 + \alpha + \dfrac{C_{Gap}}{C_A}}{\alpha + \dfrac{C_{Gap}}{C_A}}} \tag{3.18}$$

$$Q = \frac{\omega_0 L_{tot}}{R_{tot}} = \frac{\omega_0(L_f + L_K)}{R_{rad} + R_\Omega} \tag{3.19}$$

where the resonating portion of Figure 23 was reduced into components as follows.

$$L_{tot} = L_f + L_K; \quad C_{tot} = \frac{C_A\left(\alpha + \dfrac{C_{Gap}}{C_A}\right)}{1 + \alpha + \dfrac{C_{Gap}}{C_A}}; \quad R_{tot} = R_{rad} + R_\Omega \tag{3.20}$$

For a resonating circuit with quality factor, Q, the current in the resonator, I_{res}, is enhanced such that $I_{res} = QI_0$ where I_0 is the drive current. The antenna, being a resonator, gets a similar benefit. However, the full effect is not taken advantage of due to the shunting of the drive current by the capacitance, $C_{gap} + \alpha C_A$. Instead, the current seen by R_{rad} will be:

$$I_A = \frac{QI_0}{1 + \alpha + \dfrac{C_{Gap}}{C_A}} \tag{3.21}$$

The power radiated when the dipole source is coupled to the optical antenna then becomes:

$$P_{rad} = \frac{1}{2}I_A^2 R_{rad} = \frac{1}{2}\frac{Q^2 I_0^2}{\left(1 + \alpha + \dfrac{C_{Gap}}{C_A}\right)^2}R_{rad} \tag{3.22}$$

Treating the dipole source in free space as a Hertzian dipole gives the power radiated without an optical antenna.

$$P_0 = \frac{1}{2}I_{dipole}^2 R_{dipole} = \frac{1}{2}(q\omega)^2 \frac{2\pi}{3}Z_0\left(\frac{x_0}{\lambda}\right)^2 \tag{3.23}$$

We may now derive an expression for spontaneous emission enhancement by taking the ratio of (3.22) and (3.23).

$$\text{Enhancement} = \frac{P_{rad}}{P_0} = \frac{\frac{1}{2}\left(\frac{q\omega x_0}{d}\right)^2 \frac{Q^2}{\left(1 + \alpha + C_{Gap}/C_A\right)^2} R_{rad}}{\frac{1}{2}(q\omega)^2 \frac{2\pi}{3} Z_0 \left(\frac{x_0}{\lambda}\right)^2}$$

$$= \frac{3}{2\pi}\left(\frac{\lambda}{d}\right)^2 \frac{Q^2}{\left(1 + \alpha + C_{Gap}/C_A\right)^2}\left(\frac{R_{rad}}{Z_0}\right) \tag{3.24}$$

Additionally, the Q of the antenna can be expressed as $Q = \omega_0 L_{tot}/R_{tot} = 1/\omega_0 R_{tot}C_{tot}$ with R_{tot} and C_{tot} given by (3.20). The impedance that shunts the dipole source will be introduced as $Z_{shunt} = 1/\omega(\alpha C_A + C_{Gap})$. Inserting these expressions into (3.24) gives as useful form of the enhancement equation.

$$\tag{3.25}$$
$$\text{Enhancement} = \frac{3}{2\pi}\left(\frac{\lambda}{d}\right)^2 \left(\frac{Z_{shunt}}{Z_0\left(1 + \alpha + \frac{C_{Gap}}{C_A}\right)}\right)\left(\frac{R_{rad}}{R_{rad} + R_\Omega}\right) Q$$

The expression given here offers insight into how to maximize spontaneous emission enhancement using optical antennas. After the $3/2\pi$ prefactor, the first terms tells us the gap distance, d, needs to be as small as possible. As d is reduced, more current is coupled to the antenna leading to more power radiated away. The second term is associated with the shunting of induced current from the dipole source. It is beneficial to use an antenna with very large impedance where the dipole source is located. The third term is the antenna mode efficiency, η_{Mode}. In combination with the final term, Q, this implies that the maximum enhancement will occur when $\eta_{Mode} = 50\%$. We can see this by expressing the final two terms as:

$$\left(\frac{R_{rad}}{R_{rad} + R_\Omega}\right) Q = \frac{R_{rad}X}{(R_{rad} + R_\Omega)^2} \tag{3.26}$$

where $X = \omega_0 L_{tot} = 1/\omega_0 C_{tot}$ is the reactive impedance of the antenna. The value of the expression in (3.26) is maximized when $R_{rad} = R_\Omega$. Notably, the expression in (3.26) increases as the total resistance decreases. The best antenna design for maximizing spontaneous emission enhancement will have as low of a loss resistance, R_Ω, as possible. There is never a benefit to having additional loss resistance. Once loss resistance has been minimized, the maximum enhancement for a given feedgap dimension will occur with an antenna mode efficiency of 50%. However, efficiency is a more critical figure of merit than enhancement for most applications, so the antenna should be designed to have as high a radiation resistance as possible.

Let us quickly demonstrate that the enhancement predicted here using the circuit model is in agreement with the Purcell effect provided one includes efficiency. The spontaneous emission enhancement given for a dipole antenna in (3.25) can be shown to be similar to the expression given in (1.18) for the Purcell effect by introducing an effective volume.

$$\text{Enhancement} = \frac{3}{2\pi} \left(\frac{Q\lambda^2 \epsilon_0 c}{d^2 \omega (\alpha C_A + C_{Gap})(1 + \alpha + C_{Gap}/C_A)} \right) \eta_{Mode}$$

$$= \frac{3}{4\pi^2} \left(\frac{Q\lambda^3 \epsilon_0}{d^2 (\alpha C_A + C_{Gap})(1 + \alpha + C_{Gap}/C_A)} \right) \eta_{Mode}$$

$$= \frac{3}{4\pi^2} Q \left(\frac{\lambda^3}{V_{eff}} \right) \eta_{Mode} \tag{3.27}$$

where $V_{eff} = d^2 (\alpha C_A + C_{Gap})(1 + \alpha + C_{Gap}/C_A)/\epsilon_0$ is the effective mode volume of the antenna. The antenna mode efficiency is included because only power that is radiated will enhance the photon emission rate of the source.

The overall efficiency of the antenna must include the additional losses due to spreading resistance. We can express the efficiency, η_{Ant}, in terms of each loss resistance and the current flowing through them.

$$\eta_{Ant} = \frac{R_{rad}}{R_{rad} + R_{\Omega} + \left(\frac{I_0}{I_A} \right)^2 R_{spread}} \tag{3.28}$$

where the ratio of current induced by the dipole source, I_0, to the current in the antenna mode, I_A, was given in (3.21). As noted earlier, the spreading resistance increases as the dipole approaches the tips of the antenna. When the gap distance becomes small, the losses due to the spreading resistance will begin to dominate and the efficiency will drop. The result in as tradeoff between enhancement and efficiency as the gap distance is reduced. In general, the enhancement will continue to increase as the gap distance increases. Depending on antenna design, the enhancement may roll off at a certain gap dimension due to the decrease in shunt impedance. At the same time, the efficiency will plummet once the gap distance decreases below around 10 nm.
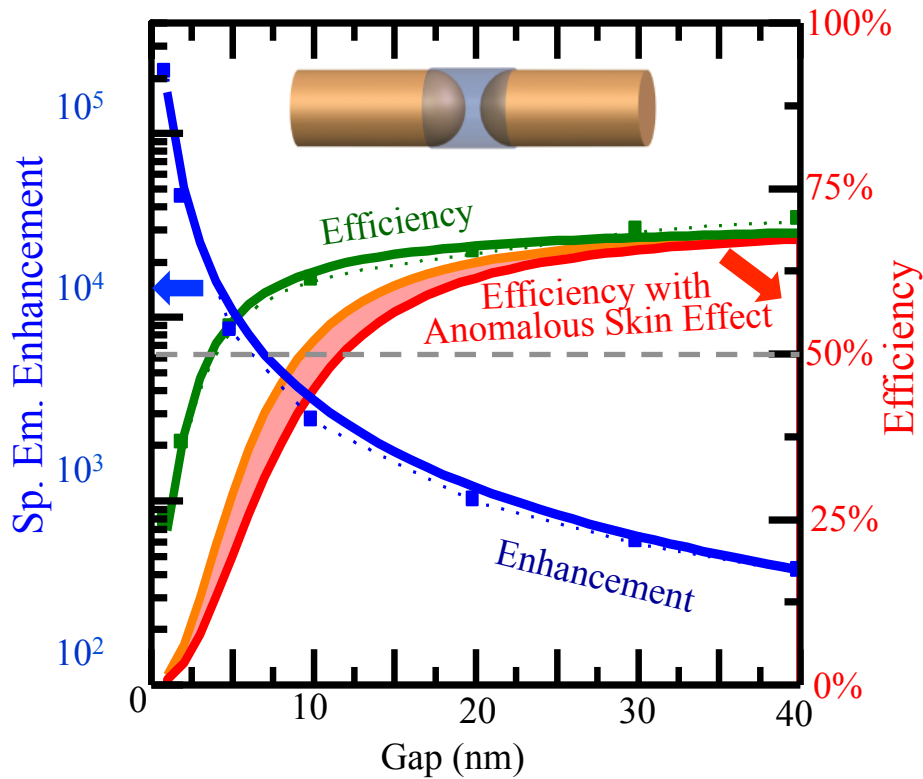
Figure 24. Spontaneous emission enhancement and efficiency for a dipole source coupled to an optical antenna. The gap is filled with a semiconductor of index 3.4 and the antenna tips are rounded to reduce the gap capacitance [34].

The tradeoff between enhancement and efficiency is illustrated by the results in Figure 24. A gold dipole antenna with a feedgap filled with semiconductor of index 3.5 is used. The tips of the antenna have been rounded to minimize the shunting impedance. As the gap size decreases, the spontaneous emission enhancement continues to increase regardless of the overall efficiency. The antenna efficiency is a constant for large gaps because the spreading resistance is small and the antenna mode efficiency, η_{Mode}, only weakly depends on gap size. Once the gap is reduced below 10 nm, the spreading resistance becomes significant and the antenna efficiency suffers. When the anomalous skin effect is taken into account, the losses due to spreading resistance become even more damaging to efficiency. This analysis suggests that sources should not be placed within 5nm of metal in devices intended for spontaneous emission enhancement.

Antenna gap size around 10 nm is the most interesting regime for enhanced spontaneous emission devices. In this range of gap size, this analysis shows it is possible to reach spontaneous emission enhancement of 2500x while still maintaining 50% efficiency. A factor of only 200x was required to make spontaneous emission as fast as stimulated

emission. Therefore, there is very real potential to use optical antennas to make spontaneous emission faster than stimulated emission.

4 Optical Antenna Design

4.1 Wheeler's Limit

Up to this point, the quality factor, Q, of antennas has simply been treated as a function of the inductance, capacitance, and resistance of an antenna structure. While this is true, there is also a fundamental relationship between the size of the antenna and the radiation quality factor, Q_{rad}. This connection was first recognized by Harlod Wheeler in 1947 [35], and resulted in "Wheeler's Limit" giving a minimum achievable Q for an antenna of volume, V.

$$Q_{rad} > \frac{3}{4\pi^2} \left(\frac{\lambda^3}{V} \right)$$

(4.1)

Wheeler's limit has some important consequences for antenna design. It states that the bandwidth of the antenna resonance decreases as the size of the antenna decreases. Semiconductors typically have a spontaneous emission spectrum corresponding to a Q of around 20. Since the resonance of the optical antenna must overlap the emission spectrum of the source in order to get enhancement, Q_{rad} should be no larger than 20. Wheeler's Limit tells us that small antennas will struggle to accomplish the low Q required.

Wheeler's Limit also gives insight into the impact that the size of an optical antenna can have on its efficiency. The antenna mode efficiency can be written as $\eta_{Mode} = Q/Q_{rad}$ where Q includes both ohmic and radiation losses. In the situation where energy is stored in the motion of electrons for half of an optical cycle (when kinetic inductance is dominant), the ohmic loss will be a fixed quantity depending only on the properties of the metal and independent of the antenna's size. In this limiting case, decreasing the size of the antenna, thus decreasing Q_{rad}, will directly reduce the antenna's efficiency. In general, the same behavior will hold true and radiation will be dominated by ohmic loss in small optical antennas.

4.2 Materials in Optical Antennas

The degree that optical antenna enhanced spontaneous emission can be efficient is entirely dependent on the materials from which the antennas are made. Unfortunately, there are no magical metals with extremely low loss at optical frequencies. The lowest loss metals are silver, gold and copper. This section will describe the optical properties of each of these materials so the proper choice can be made when fabricating optical antennas.

The optical properties of metals have been measured in numerous experiments over the years, yet there is still some uncertainty in the commonly accepted values at optical frequencies. The method of measurement, metal deposition conditions, surface topology, and thermal treatment can all contribute to differences in reported optical properties of metals. Recent work on smooth metal surfaces with controlled temperature, base pressure, and deposition rate suggest that losses in metals can be lower than conventionally accepted [36]. Complicating the situation further is the omission of the anomalous skin effect when converting experimental data into optical constants.

The divergence between reported values is especially severe for silver. For example, the commonly cited sources of optical constants for silver by Palik [30] and Johnson and Christy [29] differ by a factor of 2 in loss in the visible range. Recent experiments have attempted to address this discrepancy and show the loss is between that reported in Palik and in Johnson and Christy [37]. In this section, a Drude model with $\epsilon_\infty = 3.64$, $\omega_p = 1.39 \cdot 10^{16}$ (rad/s), and $\gamma_c = 6 \cdot 10^{13}$ (rad/s) will be used to fit the optical constants in silver. The Drude model fits well over the visible and near-infrared with the data reported in [37]. The optical constants of gold and copper have shown less divergence between sources, so those reported by Johnson and Christy will be used here.
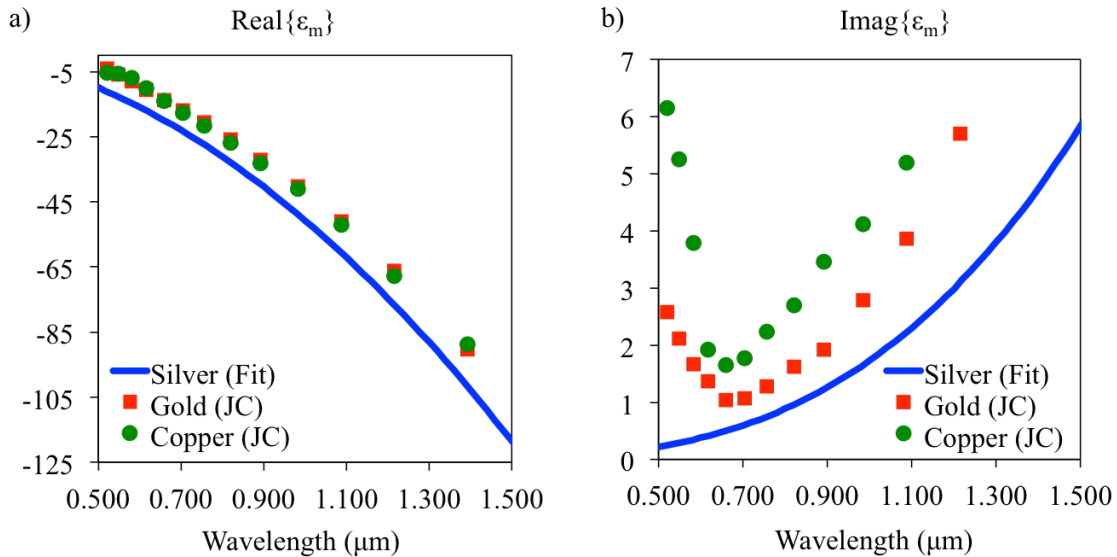
Figure 25. Optical constants for metals that might be used in optical antennas. Data for silver has been fit using a Drude model. Gold and copper data is taken from Johnson and Christy (JC) [29]. a) Real part of the permittivity, ϵ'_m. b) Imaginary part of the permittivity, ϵ''_m.

The complex permittivity for silver, gold, and copper over the visible and near-infrared are shown in Figure 25. We may convert this data into complex resistivity following the transformation given by (3.8). The transformation to complex resistivity makes it very simple to analyze which materials are the best for optical antennas. The real and imaginary parts of the complex resistivity are given in Figure 26.

41
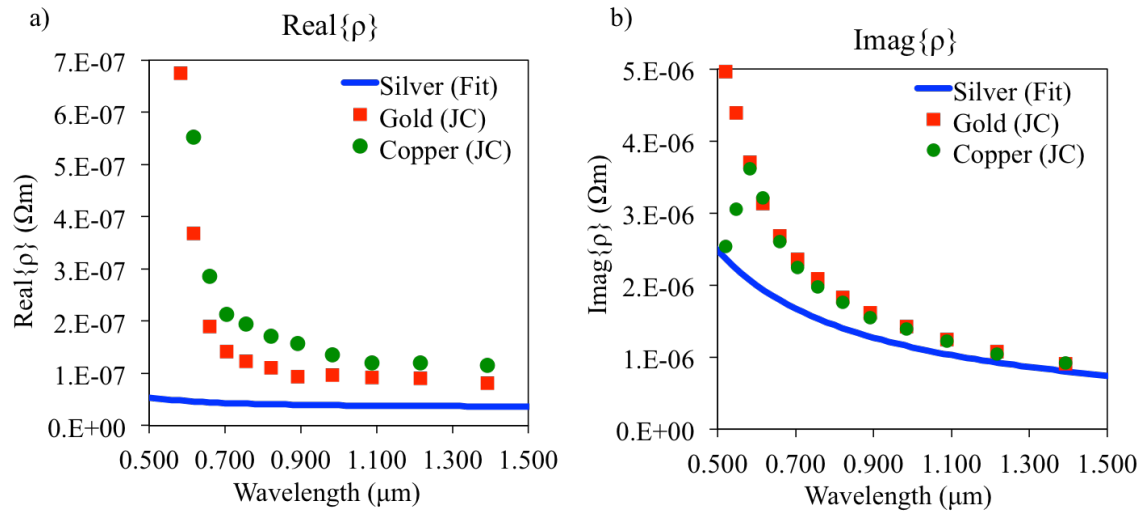
Figure 26. Real and imaginary parts of the complex resistivity for silver, gold and copper. a) Re$\{\rho\}$ corresponding to ohmic loss. b) Im$\{\rho\}$ corresponding to kinetic inductance.

The real part of the complex resistivity is associated with ohmic losses in the metal. For efficient devices, the obvious choice of material will be the metal with lowest loss. Silver is the clear winner by this standard. Unfortunately, silver reacts with sulfur in the air of an ambient environment, which tarnishes the surface. If the design of the antenna relies on high quality silver at an air interface, the performance will be severely degraded. Instead, the next best choice of metal for minimizing loss is gold. Gold is also extremely stable in ambient conditions, so structures incorporating a metal/air interface can achieve good performance. As shown in Figure 26a, gold has an absorption peak that begins to kick in at around 600 nm. Consequently, antennas intended to work at blue and green wavelengths would benefit greatly by using silver.

The imaginary portion of complex resistivity corresponds to kinetic inductance. In optical antennas designed for spontaneous emission enhancement, kinetic inductance is not a very desirable attribute. The added inductance results in reduction of the size of the antenna required for resonance at a given wavelength. A smaller antenna will negatively impact the radiation resistance, which will in turn harm efficiency. Secondly, by application of Wheeler's Limit, a smaller antenna will increase the Q of the antenna. If the antenna Q corresponds to a narrower bandwidth than the spontaneous emission source, there will be no benefit to the increased Q. Kinetic inductance may be useful for other applications of metals at optical frequencies. For example, kinetic inductance can be utilized in optical impedance transformers [20].

Finally, the benefit of using a lower loss metal can be voided if the deposition process introduces defects and impurities. If the dimensions of the device or the skin-depth are less than the mean free path of electrons, the loss will be increased. In conclusion, the choice of metals will come down to gold or silver and should be determined by constraints imposed by the fabrication process.

4.3 Nanocube Antenna Analysis

As a demonstration of the impact that the anomalous skin effect can have on optical antenna efficiency, the circuit theory approach described in this dissertation will be applied to the antenna structure used in [38] to achieve large decay rate enhancement of light emitters in the nanocube antenna gap. The antenna consists of a sheet of index n=1.4 dielectric wedged between a gold sheet and a silver cube. Figure 27 shows the nanocube antenna geometry, which contains an antenna mode similar to that in a parallel plate transmission line.
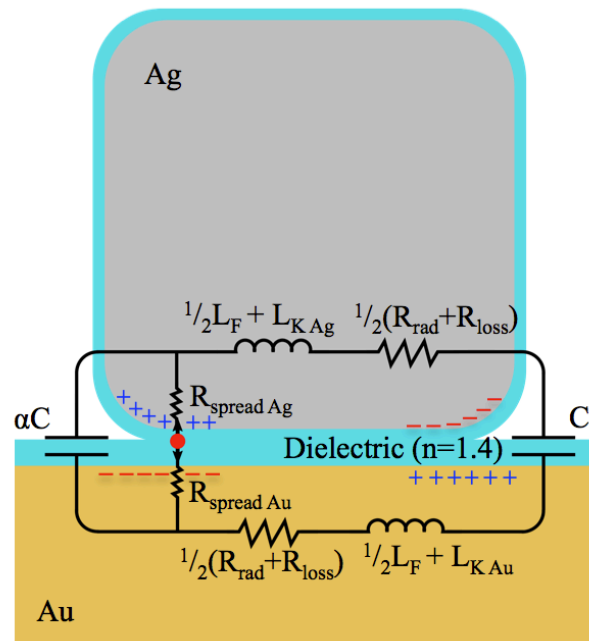
Figure 27. Nanocube antenna geometry used in [38]. The circuit diagram and charge location of the antenna resonance are overlaid.

Like a transmission line, most of the induced charge on one conductor is canceled by opposing charge on the other conductor, leading to very little radiation. Therefore, this structure has a very low radiation resistance and consequently a high radiation quality factor, Q_{rad} (Figure 28a). The resonant wavelength of this antenna depends strongly on the length of the silver cube and the gap size, as shown in Figure 28b. All structures analyzed here are resonant around 650nm, which leads to a reduction in the length of the antenna as the gap is decreased. Equivalently, this means the kinetic inductance of the antenna increases as the gap shrinks, thus making the antenna more plasmonic and sub-wavelength.
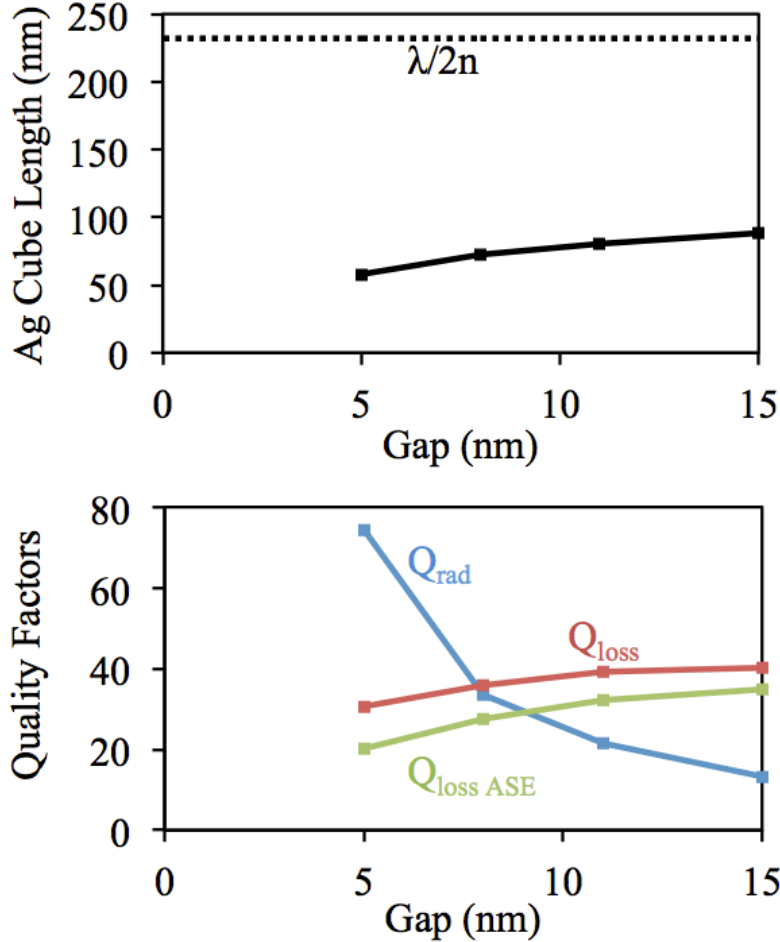
Figure 28. a) Antenna length required for resonance at 650 nm as a function of the gap spacing. The antenna is much shorter than $\lambda/2n$ due to significant kinetic inductance. b) Quality factors for the nanocube antenna as a function of gap spacing. Q_{rad} is large for small gaps.

The circuit model in Figure 23 can be used to analyze the nanocube antenna by using the lumped elements shown in Figure 27. Estimates of component values based on the antenna geometry could be made similar to the procedure that was done for a dipole antenna in an earlier section. In this analysis a different approach will be used, and all component values will be extracted directly from FDTD simulations. The circuit model contains only six parameters (R_{rad}, R_Ω, L, C, α and β), which can be quantified by taking six quantities (η_{Mode}, η_{Dipole}, Enhancement, ω_0, Q_{tot}, R_Ω) from an FDTD simulation.

The method for extracting each of the antenna parameters will be briefly described. η_{Mode} is the efficiency of the antenna mode and can be found by exciting the antenna structure with a plane wave. This efficiency disregards the effect of the location of a dipole source and is a measurement of $R_{rad}/(R_{rad} + R_\Omega)$ from the circuit in Figure 23. η_{Dipole} is the radiative efficiency of a dipole in the antenna gap found by the ratio of radiated power to total power dissipated by the dipole source. This efficiency includes losses in the spreading resistor of Figure 23, but does not take into account the increased losses due to

the anomalous skin effect. The radiative enhancement is the quantity of interest in spontaneous emission rate enhancement experiments and is quantified as the radiated power of the dipole in the antenna gap divided by the radiated power of a dipole in freespace. ω_0 and Q_{tot} are the resonant frequency and total quality factor of the antenna mode, respectively. ω_0 and Q_{tot} are found simply by looking at the frequency response of the antenna mode. R_Ω can be obtained by integrating the total power absorbed, P_{abs}, by the antenna when illuminated by a plane wave. The magnitude of the current flowing through the antenna, I_{ant}, can be extracted in the plane at the midpoint of the antenna mode. Using the relation $R_\Omega = 2P_{abs}/I_{ant}^2$ leads to the final circuit model parameter.

Figure 29 shows how the optical efficiency of the nanocube antenna is reduced as various effects are taken into account. The blue FDTD curve corresponds to the antenna mode efficiency, η_{Mode}, when the bulk collision properties of the metal are assumed. The efficiency is reduced to the red FDTD curve, η_{Dipole}, when a dipole source located in the antenna gap is used as the excitation. The reduction in efficiency between η_{Mode} and η_{Dipole} corresponds to spreading resistance loss. The lower blue and red curves denote η_{Mode} and η_{Dipole} when the anomalous skin effect is taken into account, respectively.
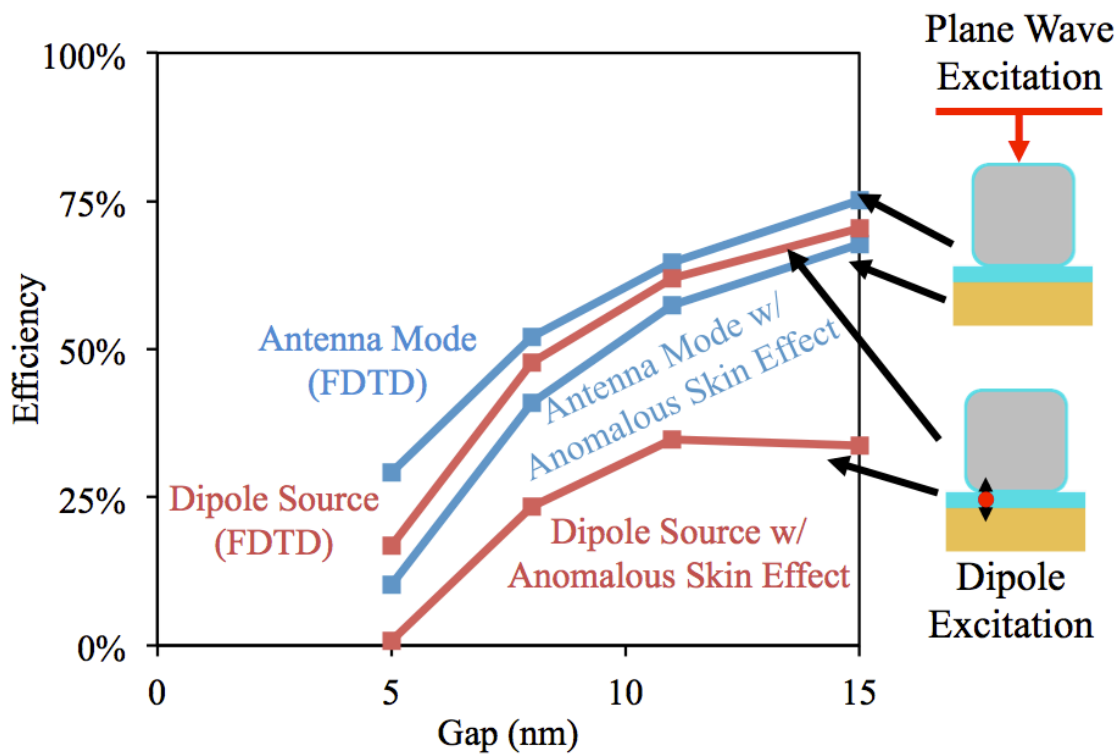
Figure 29. Optical antenna efficiencies incorporating dipole source, anomalous skin effect and surface collisions. (blue FDTD) Antenna mode efficiency using bulk metal properties. (red FDTD) Radiative efficiency using bulk metal properties when excited by a dipole source. (blue ASE) Antenna mode efficiency with the anomalous skin effect. (red ASE) Radiative efficiency incorporating the anomalous skin effect when excited by a dipole source. This curve corresponds to the optical efficiency that would be observed in a spontaneous emission rate experiment.

It is evident from these results that incorporating the anomalous skin effect is crucial to properly estimate optical antenna efficiency. This is especially true for spontaneous emission enhancement experiments where light emitters may be only a few nanometers from a metal surface. For example, FDTD simulation predicts that a light emitter in a nanocube antenna with an 11nm gap will have 62% radiative efficiency (red FDTD curve in Figure 29). Incorporating the anomalous skin effect reduces this efficiency to only 35% (red ASE curve).

In addition to a modification of optical efficiency, the inclusion of these effects through the antenna mode resistance, R_Ω, can have an impact on the expected radiative spontaneous emission enhancement. The loss resistance of the antenna mode is adjusted by the anomalous skin effect by equation (3.15). Essentially, loss in the antenna mode is increased to the extent that the skin depth of the antenna mode is smaller than the skin depth of a plane wave incident on the metal surface. The skin depth formula for a surface plasmon is given by (4.2) and is very similar to that of a plane wave hitting a metal surface except for the k-vector correction. By combining equations (3.15) and (4.2) it is clear that very sub-wavelength (large k-vector, highly plasmonic) antennas will be most affected by this additional loss.

$$\ell_{skinMode} = \frac{1}{\sqrt{k^2 - \epsilon_m \left(\frac{\omega^2}{c^2}\right)}} \tag{4.2}$$

By returning to the enhancement formula given by the circuit model in equation (3.25), we see that the additional loss in the antenna mode will decrease the radiative enhancement. The added loss in the antenna mode will reduce Q_{loss} as depicted in Figure 28. A comparison of the radiative enhancement with and without the anomalous skin effect is given in Figure 30. The change in enhancement is greatest when the gap is small and the antenna is most plasmonic.
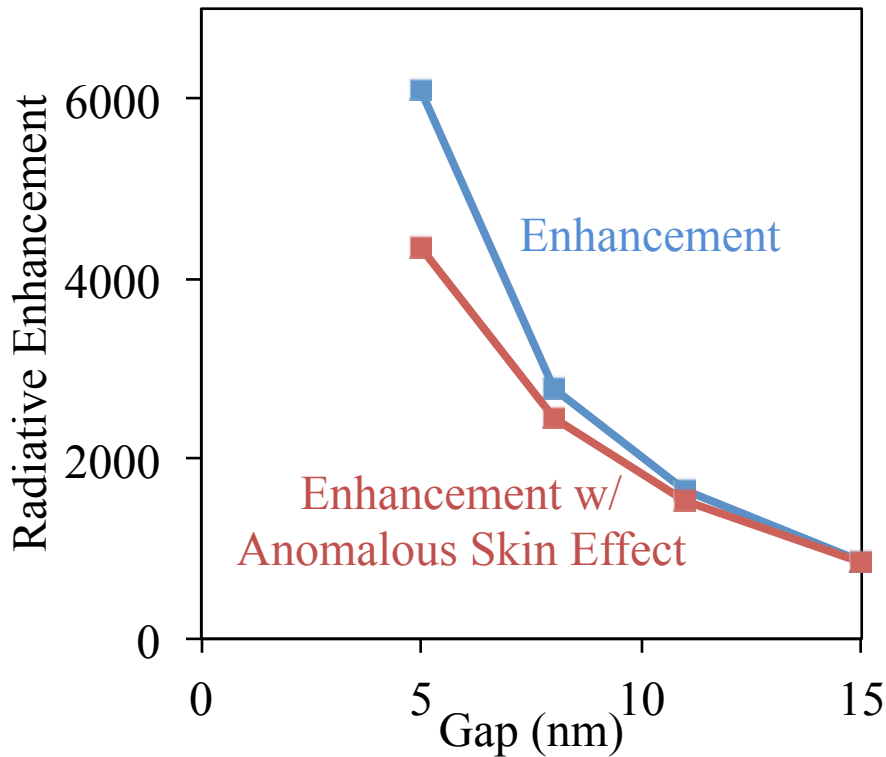
Figure 30. Radiative spontaneous emission enhancement as a function of gap size for the nanocube antenna. The anomalous skin effect and surface collisions have the most impact on enhancement for small gaps, where the antenna is more plasmonic.

The large adjustment of antenna efficiency due to the anomalous skin effect has important consequences for the interpretation of spontaneous emission enhancement experiments. Time-resolved photoluminescence measurements are often used in order to quantify the increased rate of spontaneous emission. The drawback of this technique is that increased radiative rates are indistinguishable from increased non-radiative rates in a time-resolved measurement. The experimentalist will often cite simulated quantum efficiency in order to separate the radiative enhancement from non-radiative enhancement. Because standard simulation software does not incorporate surface collisions and the anomalous skin effect into the quantum efficiency calculation, claims of radiative spontaneous emission enhancement are exaggerated. We propose our circuit model and resistance modification as a straightforward solution to include these often neglected effects.

4.4 Cavity-Backed Slot Antenna

Aperture antennas are a category of antenna designs that are heavily used at microwave frequencies. These antennas consist of a sheet of metal with a dielectric opening. Radiation and spontaneous emission enhancement from these structures can also be explained in terms of the antenna circuit model developed in this dissertation. The cavity-

backed slot antenna, a particular type of aperture antenna, will be studied in this section due to its advantages in experimental demonstration of large spontaneous emission enhancement.

To begin understanding the cavity-backed slot antenna, we first turn our attention a ordinary slot antenna. Radiation from slot antennas can be understood by applying Babinet's principle to the previously analyzed case of a dipole antenna. Babinet's principle states that sum of the fields from a source behind an opaque object and the compliment of the opaque object is equal to the field from the source with no obstruction present. Booker extended the principle to antennas by showing radiation from a dipole antenna can be related to radiation from it's compliment, the slot antenna [39]. The geometry of these two antenna structures is shown in Figure 31.

a)   b)
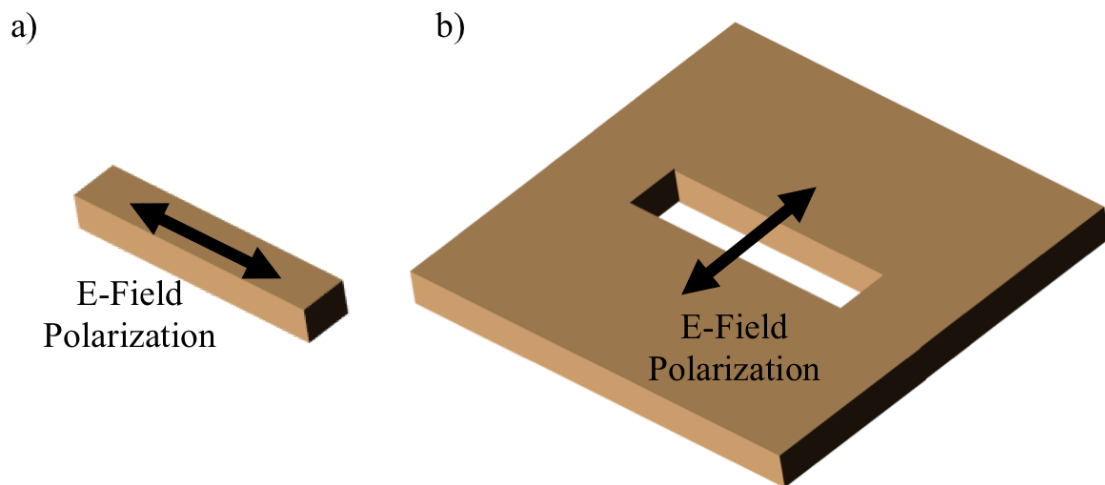
Figure 31. a) Dipole antenna and polarization of antenna mode electric-field. b) Slot antenna and polarization of antenna mode electric-field.

The slot antenna is essentially the dual of the dipole antenna. The substitution of all metals with dielectrics and vice versa in the plane of the antenna leads to an interchange between electric and magnetic fields. Consequently, both structures in Figure 31a and b have the same resonant frequency. The antenna mode of the slot antenna now consists of an electric field with polarization perpendicular to the long-axis of the slot. Therefore, the dipole source orientation that will couple to the slot antenna will also be perpendicular to the long-axis of the slot. The gap length that determines the strength of current induced in the antenna by Ramo's theorem (equation (1.13)) will be the width of the short-axis of the slot.
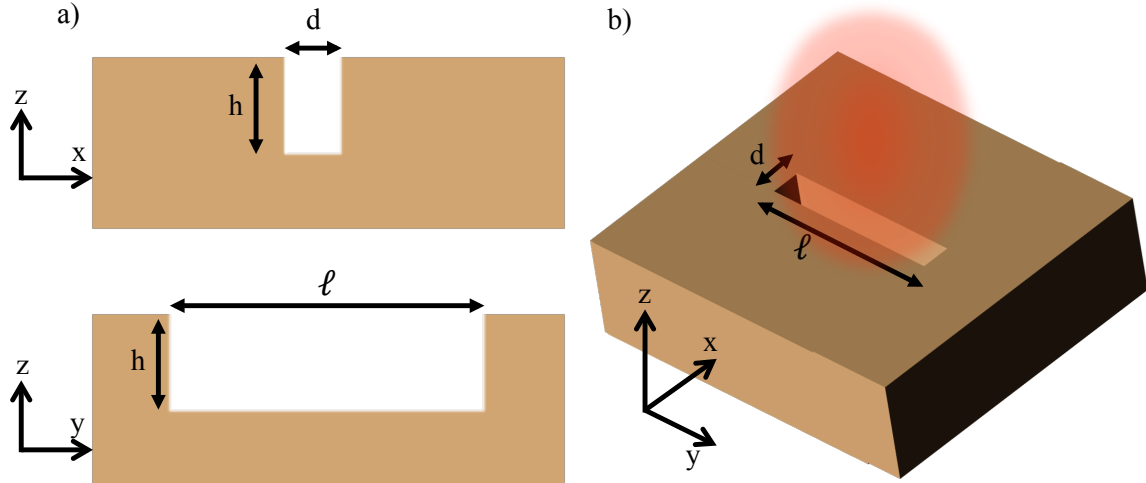
Figure 32. Cavity-backed slot antenna. a) Cross-sections of antenna geometry. The cavity is defined by its length, ℓ, width, d, and depth, h. b) Perspective view of antenna geometry. Radiation is directed only into the hemisphere above the cavity-backed slot antenna.

Adding a cavity to the slot antenna has several advantages for experimental demonstration of spontaneous emission enhancement. First, instead of emitting radiation both above and below the plane of the slot antenna, adding a cavity will direct the radiation into a single hemisphere. The improved directivity will results in easier detection of signals in any optical antenna experiment. Second, the addition of a cavity allows for a method of tuning the resonant properties of the antenna. Lastly, including a cavity allows for a simplified fabrication process of the optical antennas.

A schematic of the cavity-backed slot antenna is shown in Figure 32. The length, width, and height of the cavity are the three parameters that can be adjusted in this design. The width of the antenna should be as small as possible down to 10nm, which is the regime where spreading resistance and the anomalous skin effect begin to substantially harm antenna efficiency. The cavity depth and length can then be tuned so that the antenna will be resonant at the desired frequency. The cavity can be interpreted as added capacitance and inductance to the slot antennas capacitance and inductance. The cavity can be treated like a rectangular waveguide to estimate these additional reactive elements [40]. As the cavity depth is increased, the length of the slot must be reduced to maintain the same resonant frequency.

Changing the cavity length and depth will affect the total quality factor, Q, and the radiation quality factor, Q_{rad}. At the same resonant frequency, longer slots will have larger radiation resistance ($R_{rad} \propto \ell^2/\lambda^2$) and result in lower Q_{rad}. Ohmic losses in the antenna mode will only weakly depend on the length of the antenna slot. Each antenna has the same gap width of 20nm and is tuned to be resonant at $\lambda = 700$nm.

As the slot length is reduced and Q_{rad} is increased, the antenna mode efficiency (Q/Q_{rad}) approaches 50%. If we recall, the circuit model for optical antenna enhanced spontaneous emission predicts that the enhancement is maximized when the antenna mode efficiency is 50%. Indeed, when a dipole source is placed in the antenna gap of each of the structures analyzed in Figure 33, the highest spontaneous emission enhancement is achieved by the antenna that has 50% efficiency.
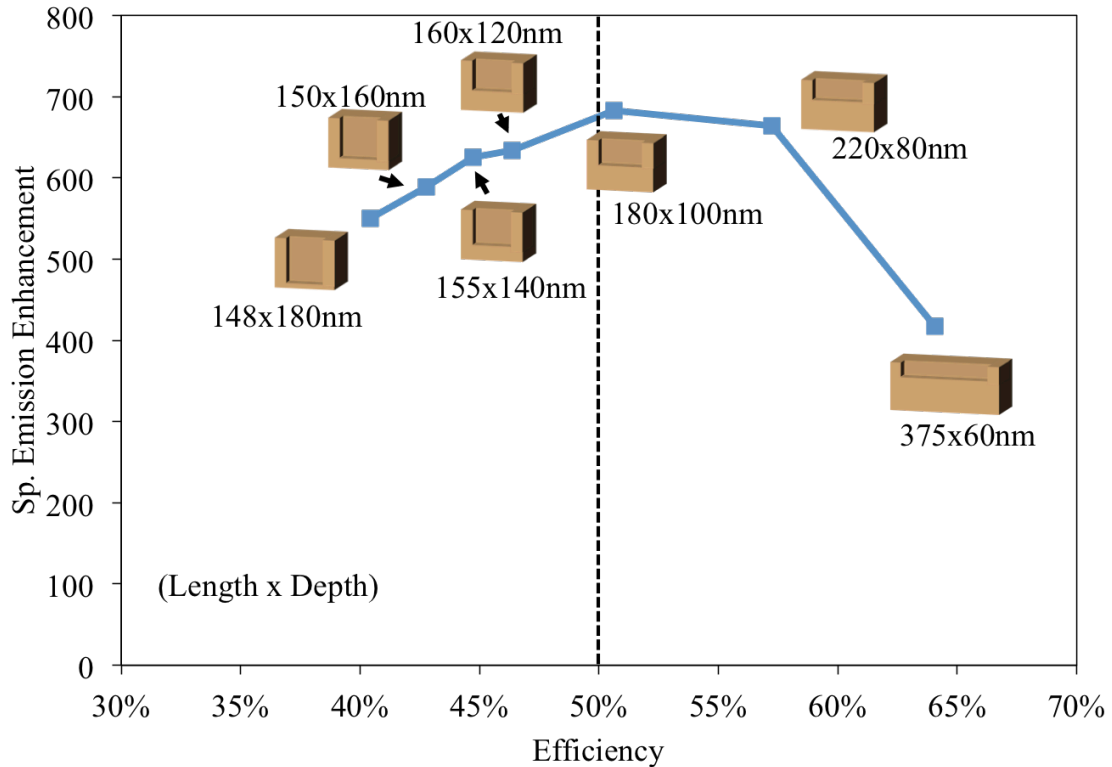
Figure 33. Slot antenna enhancement and efficiency for various cavity depths. All of the antennas have the same gap size of 20nm. The length of each antenna is chosen so that the structure is resonant at λ=700nm. The maximum enhancement occurs when the antenna efficiency is 50%.

The cavity-backed slot antenna is a very interesting antenna design due to the advantages detailed in this section. It is an easily fabricated structure with directional emission into one hemisphere. Additionally, the cavity allows for a range of designs with the same resonant frequency that can be chosen either to maximize efficiency or to maximize spontaneous emission enhancement.

5 Enhanced Spontaneous Emission from InP

Interest in enhancing the spontaneous emission rate of light emitters has increased over the past decade. Early experiments on single molecules in the gap of bowtie antennas demonstrated the ability of antennas to enhance the decay rate of a coupled light emitter [41]. Enhancement of spontaneous emission from quantum wells was demonstrated using scattering from plasmons in a metal sheet [42] and dipole antennas [43], but these approaches were limited to low enhancement and efficiency. Larger enhancement has recently been demonstrated using dye molecules [38], [44], [45] and erbium atoms [46], but these emitters do not provide the path to electrical injection that is required for an antenna-enhanced LED. In this section, an InP ridge will be used as the active material and will be coupled directly to the gap of an arch-dipole antenna.

5.1 Device Design and Fabrication

The antenna used to enhance the spontaneous emission rate of InP is an arch dipole antenna. This geometry provides for a method of tuning the gap impedance in the antenna to reduce shunting of source current that occurs for with very small antenna gaps. Additionally, this structure has an advantage in fabrication due to the self-alignment of the antenna gap to the semiconductor source. The arch dipole structure has been utilized in both SERS and spontaneous emission enhancement experiments to enhance light-matter interactions [34], [47], [48].

The addition of the inductive arch to the antenna causes the fundamental mode of the antenna to split into two resonances. The lowest frequency resonance corresponds to the mode that has both the current in the antenna arms and the current in the arch in phase with each other. This will be referred to as the symmetric mode. The higher frequency resonance is a mode with the current in the antenna arms 180 degrees out of phase with the current in the inductive arch. This will be referred to as the anti-symmetric mode. The mode used for this design will be the anti-symmetric mode because the length of the antenna operating at the anti-symmetric resonance is longer than the antenna operating at the symmetric resonance. Since Wheeler's limit tells us that the radiation Q of the antenna depends on the antenna volume, we know that the longer antenna will be the better antenna.
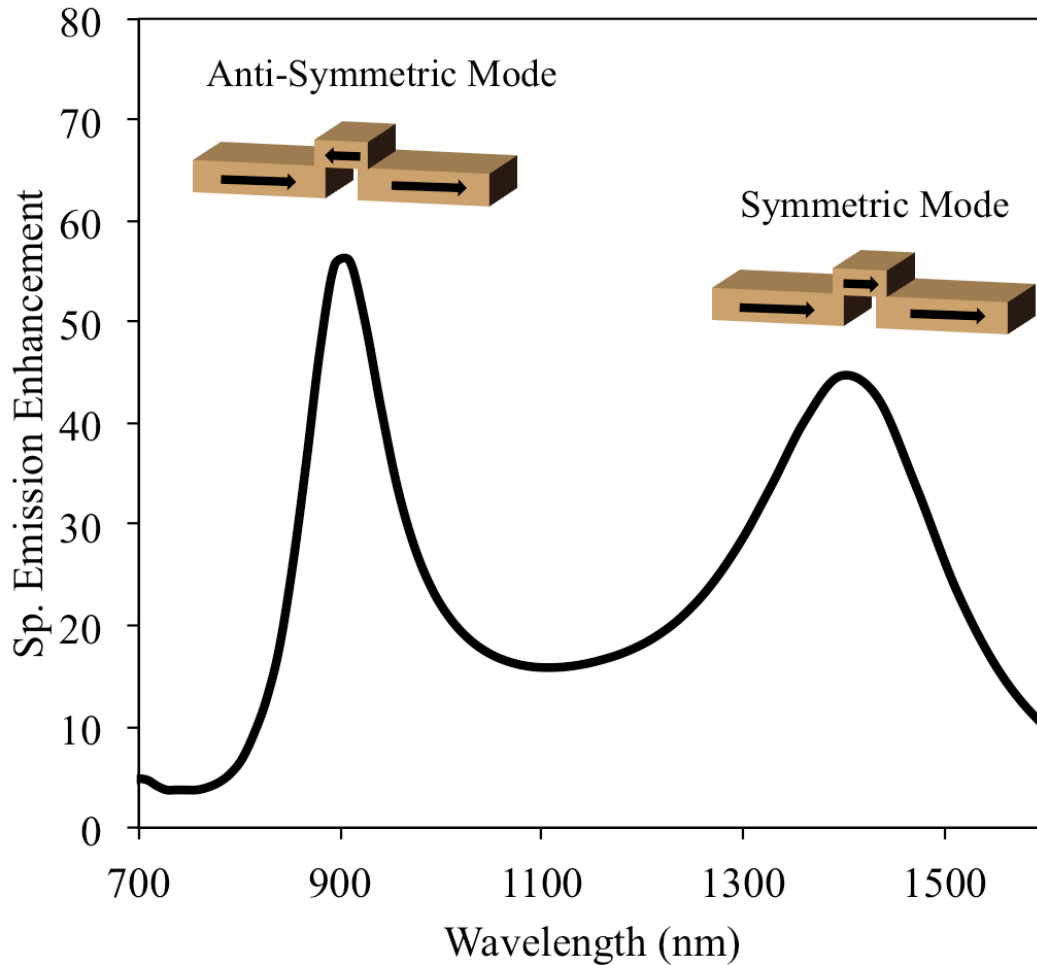
Figure 34. Spontaneous emission enhancement for Arch-Dipole antenna coupled to an InP source. The arch splits the fundamental antenna resonance into a higher frequency anti-symmetric mode and a lower frequency symmetric mode.

The fabrication process for this optical antenna design begins by forming the InP emitter. The InP needs to be shaped into a nanoscale ridge with a width that approaches 10nm. The width of the InP ridge will dictate the size of the antenna gap, which has a large impact on how much spontaneous emission enhancement can be achieved by the optical antenna. An outline of the process used to fabricate the small InP ridges is shown in Figure 35.
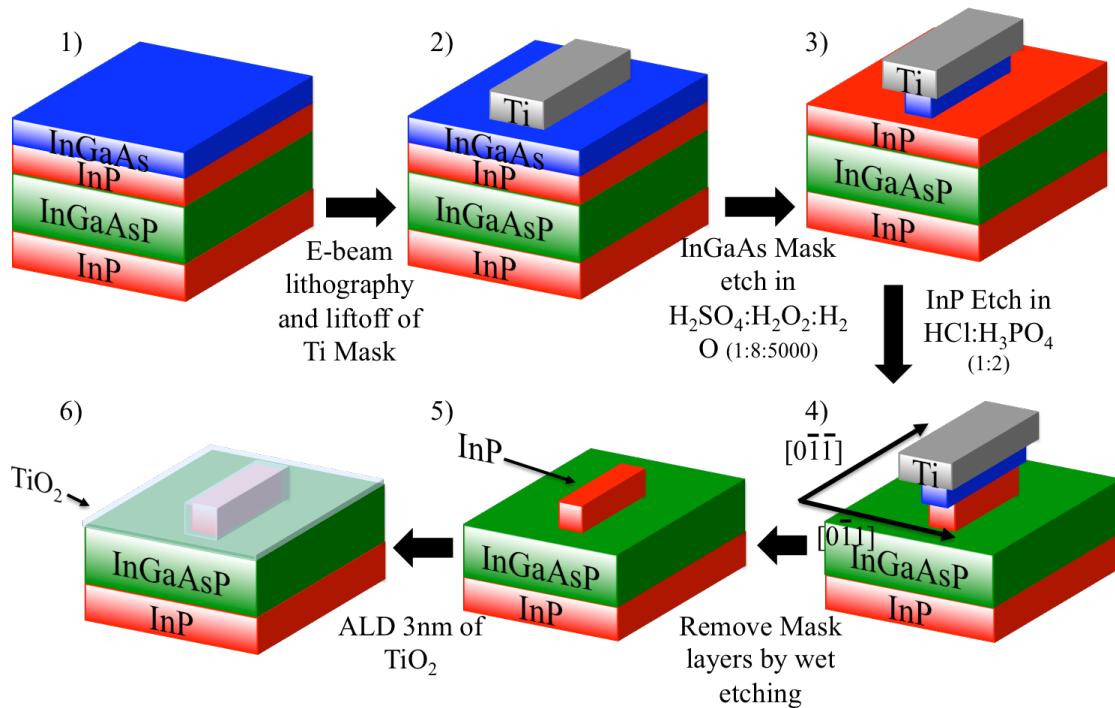
Figure 35. Fabrication process flow for InP ridges with widths down to 10nm. The crystal plane orientation is shown in step 4.

The process begins with an epitaxially grown wafer consisting of a 10nm InGaAs layer, the 10nm InP active layer, a 150nm InGaAsP etch stop, and the InP substrate. The process begins by patterning a titanium hard mask, which will be used to etch the InGaAs layer into thin ridges. PMMA A2 photoresist is patterned by electron beam lithography and developed in MIBK/IPA (1:3). The titanium mask is then formed by electron-beam eveaporation of 7nm of titanium followed by liftoff in acetone. Next, the InGaAs layer is etched using a dilute mixture of sulfuric acid, hydrogen peroxide, and water (1:8:5000). This etches InGaAs at a rate of approximately 2nm/s [49]. The goal of this etch is to form InGaAs ridges with as narrow a width as possible. Several different widths of titanium masks with an average width of about 100nm were used so that the precise timing of the wet-etch would not be crucial. An example of the resulting undercut and remaining InGaAs ridge is shown in Figure 36. Typically an undercut of around 40nm was used, and the narrowest ridges were around 15nm wide.
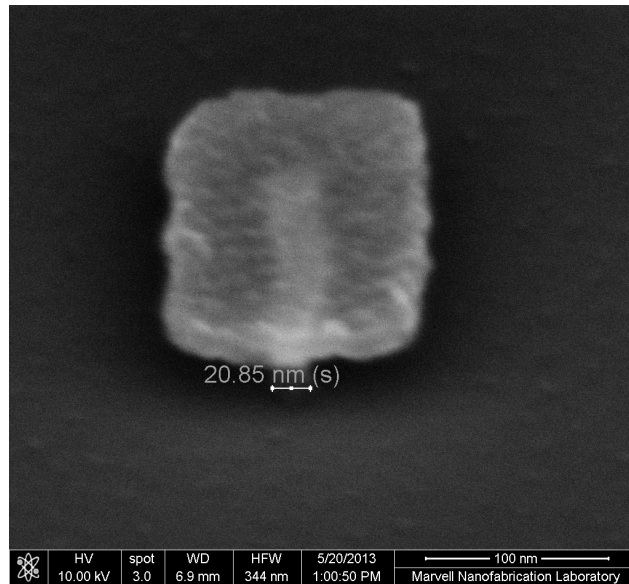
Figure 36. Tilted SEM image of InGaAs ridge after using wet-etch to undercut the Ti mask corresponding to step 3 in Figure 35. Good control of the etching rate enables ridge widths in the 10-20nm range.

The InGaAs ridge will now be used as a mask to etch the InP ridge that will be the emitting material for the optical antennas. There are a multiple reasons why this method was used to etch the InP rather than using a dry-etching method. First, dry etching of III-V materials is known to induce many defects at the etched surface. Since the surface to volume ratio for the InP ridges is very large, the poor surfaces created by dry-etching would make the PL efficiency prohibitively low. Instead, wet etching InP with HCl based etchants results in relatively good surfaces. However, the etch rate of InP in HCl solutions cannot be controlled with the precision necessary to get a 15nm wide ridge. The etch rate of InGaAs in dilute H_2SO_4:H_2O_2:H_2O can be controlled into the nm/s range allowing for precise control of ridge width. Finally, HCl based etching of InP shows a very anisotropic etching pattern when masked by a layer of epitxially grown InGaAs [50]–[53]. By choosing the long axis of the ridge to follow the [0,1,1] crystal plane, the sidewall of the InP will be nearly vertical and will not undercut the InGaAs mask above it. In this way the precisely controlled InGaAs wet-etch can be used to control the width of the InP ridge beneath it.

54
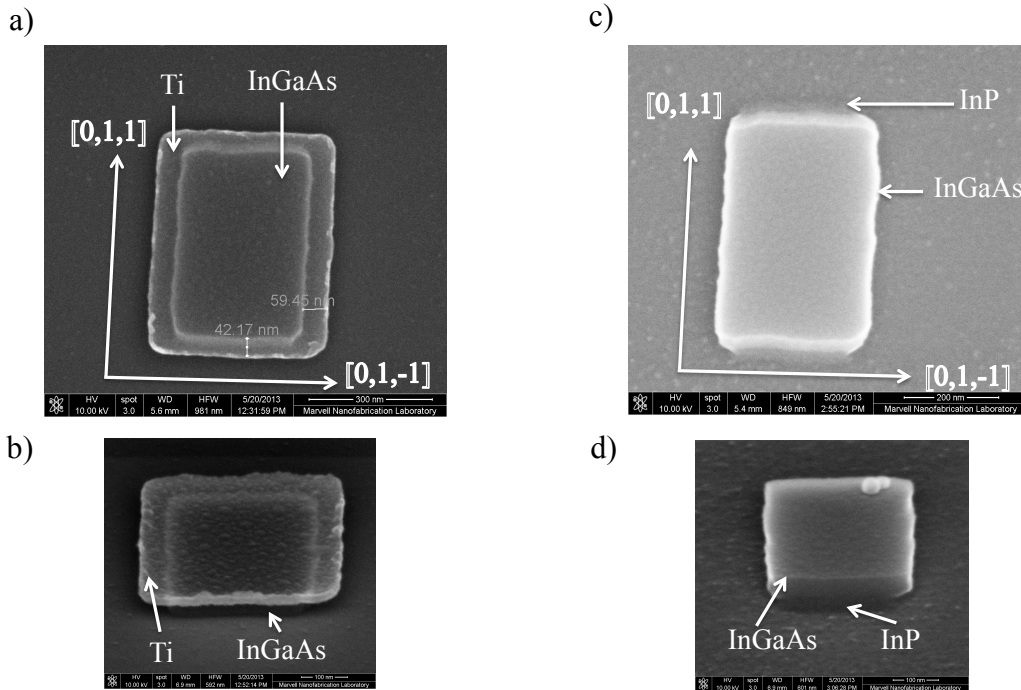
Figure 37. a) SEM Image showing undercut of Ti mask after InGaAs etch step. b) Tilted
view of after InGaAs etch. b) Image of ridge after InP etch and Ti mask removal. The InP
etch is sensitive to the crystal plane orientation such that one edge has a nearly vertical
sidewall. d) Tilted view after InP etch and Ti mask removal.

The anistropic etching of InP beneath the InGaAs mask can be seen in Figure 37. The
HCl based etchant does not etch the InP beneath the InGaAs and the [0,1,1] edges are
nearly vertical. There is a noticeable undercut at the corners of the test patch because the
[0,0,1] and [0,1,0] crystal planes do get etched. After completing the InP etch in
HCl:H_3PO_4 (1:2), titanium mask is removed with HF. The InGaAs mask can then be
removed using H_2SO_4:H_2O_2:H_2O. Finally, a 3nm film of TiO_2 is deposited by atomic
layer deposition (ALD). The insulating layer is used to provide a barrier between the InP
active region and the optical antenna.
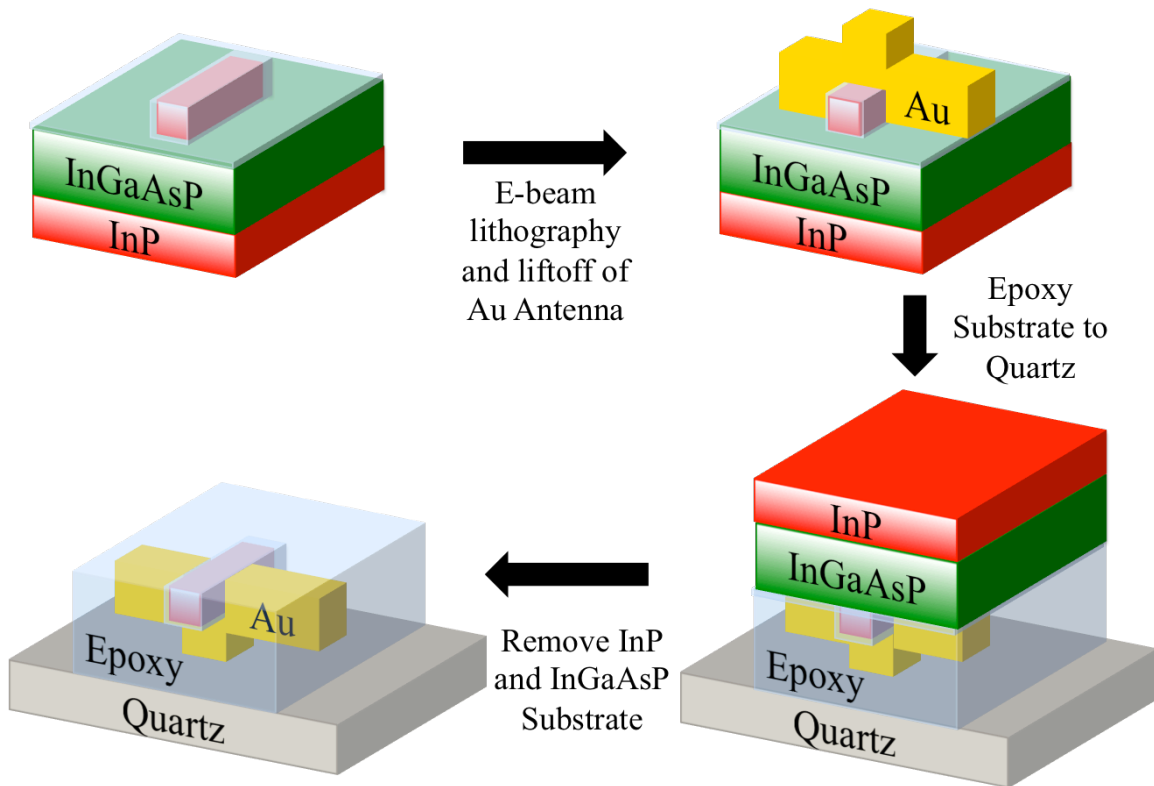
Figure 38. Fabrication process flow for optical antennas used to enhance the spontaneous emission rate of InP.

Optical antennas can then be fabricated on some of the InP ridges while others are left bare to serve as the control for characterizing spontaneous emission enhancement. PMMA A2 resist is again used for e-beam lithography to define the optical antenna. E-beam evaporation is then used to deposit a thin layer (1-2nm) of titanium for an adhesion layer. Next, a 35nm layer of gold is evaporated to form the optical antennas. The sample is soaked in acetone to liftoff the excess metal regions. Images of the bare InP ridge and completed optical antenna devices are shown in Figure 39.
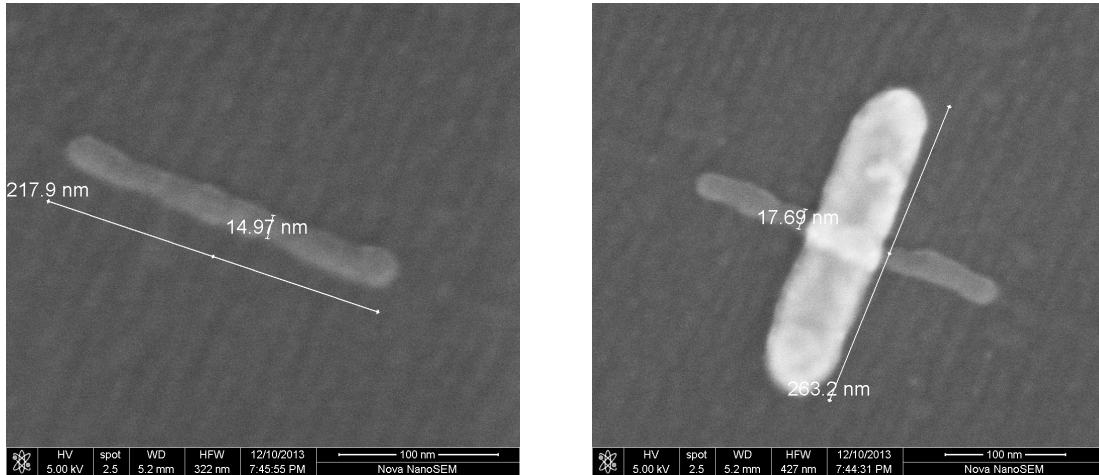
Figure 39. Completed fabrication of a) bare InP ridge and b) optical antenna device before substrate removal

The final step in the fabrication process involves transferring the completed devices to a transparent substrate. A bead of optical epoxy (NOA 81) is placed on the top-side of the sample. A quartz substrate is placed on top of the epoxy and the entire structure is cured in a UV oven for 10 minutes. Once the quick cure is complete, the sample is placed on a hotplate for 12 hours at 50C. The majority of the InP is removed by mechanical lapping with 1500 grit silicon carbide sandpaper. The sample is placed in $HCl:H_3PO_4$ (1:1) at 50C until the remainder of the InP substrate is removed. Lastly, the InGaAsP etch stop can be removed using $H_2SO_4:H_2O_2:H_2O$ (1:1:10). The end result is the structure shown in the final step of Figure 38.

Removal of the high-index InP substrate is crucial for characterizing spontaneous emission enhancement. Light emitted by an antenna at the interface between air and a high-index substrate will preferentially emit into the substrate [54]. If the substrate consists of planar interfaces, much of the light will be trapped in the high-index substrate [55]. However, if the surface contains scattering sites such as roughness or antennas, the trapped light can escape. In a PL experiment this would result in more light collected from the region containing antennas than regions that do not. This effect is not related to the rate of spontaneous emission, so it must either be mitigated or accounted for. Removing the high-index substrate and replacing it with quartz greatly reduces the impact of light-trapping due to a quadratic dependence on the refractive index.

5.2 Measuring Spontaneous Emission Enhancement

There are two strategies that can be used to experimentally measure the enhancement of spontaneous emission. The best method for determining spontaneous emission enhancement will depend on the quantum efficiency of the light emitter used. For low quantum efficiency, a comparison of quantum efficiency of the antenna coupled emitter

to a bare emitter will give spontaneous emission rate enhancement. For efficiencies near 100%, a time resolved measurement would give the enhancement. For moderate efficiencies, a combination of both quantum efficiency and time-resolved measurement may be necessary to accurately determine the rate enhancement. In order to demonstrate how each of these measurements is related to the spontaneous emission rate, we need to return to the carrier recombination rate equations.

The quantum efficiency of the semiconductor light emitter without an optical antenna can be described in terms of a radiative, τ_0, and non-radiative, τ_{nr}, lifetime as was done in Chapter 1.

$$QE = \frac{\frac{1}{\tau_r}}{\frac{1}{\tau_r} + \frac{1}{\tau_{nr}}} \tag{5.1}$$

First, we will examine the case of low quantum efficiency emitter ($\tau_{nr} \ll \tau_0$). This gives with good approximation a simplified form of quantum efficiency.

$$QE \approx \frac{\tau_{nr}}{\tau_0} \tag{5.2}$$

The antenna-coupled source will emit a factor of F_p more power than in the bare case, where F_p was defined in (1.24). Using the antenna efficiency, η_{Ant}, defined as the ratio of radiated power to total power loss in the antenna allows us to write the quantum efficiency of the antenna-coupled source.

$$QE_{Ant} = \frac{\frac{F_p}{\tau_0}\eta_{Ant}}{\frac{F_p}{\tau_0} + \frac{1}{\tau_{nr}}} \tag{5.3}$$

If the quantum efficiency is still low ($\tau_{nr} \ll \tau_0/F_p$), the antenna-coupled quantum efficiency may also be simplified.

$$QE_{Ant} \approx \left(\frac{\tau_{nr}}{\tau_0}\right) F_p \eta_{Ant} \tag{5.4}$$

Now, the ratio of (5.4) and (5.2) gives an experimental determination of spontaneous emission enhancement.

$$\frac{QE_{Ant}}{QE_0} = F_p \eta_{Ant} = \text{Enhancement} \tag{5.5}$$

The ratio of quantum efficiencies between the antenna-coupled source and bare source can be obtained by a photoluminescence measurement. This method of experimentally

determining spontaneous emission enhancement will only include increases in the rate of radiation produced by the source material. Notably, the antenna efficiency is already incorporated into the measurement, so the effects of unknown material loss properties in the antenna are included.

Also, the enhancement measured by (5.5) will be an underestimate of the spontaneous emission enhancement for sources with higher quantum efficiencies. As τ_0/F_p approaches τ_{nr}, equation (5.4) is no longer accurate and the enhancement given by (5.5) will yield an artificially low value. This is due to the fact that even for infinite spontaneous emission enhancement, the highest observed quantum efficiency from the antenna-coupled sources will be $QE_{Ant} = \eta_{Ant}$. Therefore, the maximum enhancement that can be experimentally observed by measuring quantum efficiency will be:

$$\text{Max Enhancement} = \frac{\eta_{Ant}}{QE_0} \tag{5.6}$$

The second method of determining spontaneous emission enhancement relies on a direct measurement of the carrier recombination lifetime through a time-resolved photoluminescence measurement. Time-resolved measurements only give information about the total decay rate of the source with no differentiation between the radiative and non-radiative loss mechanisms. Again using the rate equations from Chapter 2, we have the total decay rate of the bare emitter, Γ_0, and the antenna-coupled emitter, Γ_{Ant}.

$$\Gamma_0 = \frac{1}{\tau_0} + \frac{1}{\tau_{nr}}$$

$$\Gamma_{Ant} = \frac{F_p}{\tau_0} + \frac{1}{\tau_{nr}} \tag{5.7}$$

In the low efficiency regime ($\tau_{nr} \ll F_p\tau_0$), the ratio Γ_{Ant}/Γ_0 would yield no information. The carrier recombination rate is set by the non-radiative recombination lifetime, so both situations would yield the same decay rate. In the high efficiency regime ($\tau_{nr} > \tau_0$), we may simplify the decay rate ratio to a form that does yield some information about the spontaneous emission enhancement.

$$\frac{\Gamma_{Ant}}{\Gamma_0} \approx F_p \tag{5.8}$$

Unfortunately, the quantity F_p gives the enhanced rate of emission into both radiation and ohmic losses in the antenna. Therefore, the time-resolved method reveals nothing about the antenna efficiency and relies on assumptions about antenna material quality and design performance. Using a combination of both quantum efficiency and time-resolved measurements will allow for more information to separate the radiative and non-radiative decay channels. However, this is often very difficult in practice since time-resolved measurements are typically performed at very high initial carrier concentrations in order to get sufficient signal incident on the detector. The quantum efficiency can vary

significantly with carrier concentration, so care must be taken to ensure the same carrier concentration is used for both the quantum efficiency and time-resolved measurements.

The experimental demonstrations of spontaneous emission enhancement in this dissertation will utilize the method of quantum efficiency comparison. Photoluminescence measurements are performed while taking into account the effect of the antenna structure on the laser pump intensity seen by the emitting material in order to compare quantum efficiencies with and without the antenna present. This approach gives a lower bound on spontaneous emission enhancement while inherently taking into account ohmic losses in the antenna.

5.3 Pump Enhancement

In any photoluminescence experiment where quantum efficiencies are measured it is necessary to know what portion of the pump laser the light emitter absorbs. In the case of comparing two samples consisting of the same material, one can simply say the two samples absorb the same amount of light. This leads to a straightforward comparison of quantum efficiency by the relative intensity of photoluminescence. However, the amount of absorbed pump light can differ substantially when the two samples are in different electromagnetic environments. The presence of an optical antenna coupled to the light emitter can substantially change how much pump light is absorbed. Therefore, the enhancement in photoluminescence observed by antenna-coupled devices over bare devices must be corrected to account for pump enhancement.

The pump enhancement for this type of antenna design can be accounted for by taking advantage of the fact that the antenna only strongly modifies light polarized along the antenna's long-axis. Characterization of the pump enhancement begins by pumping both the bare InP and antenna-coupled InP with light in the antenna polarization. The antenna enhances the field seen by the antenna-coupled InP leading to greater absorption and a higher carrier density than in the bare InP. A polarizer is then used on the resulting InP photoluminescence so that only light polarized perpendicular to the antenna is collected. In this polarization, the antenna does not strongly modify the spontaneous emission. Therefore, the ratio of light intensity collected by the antenna-coupled device to the bare device gives a measurement of pump enhancement.
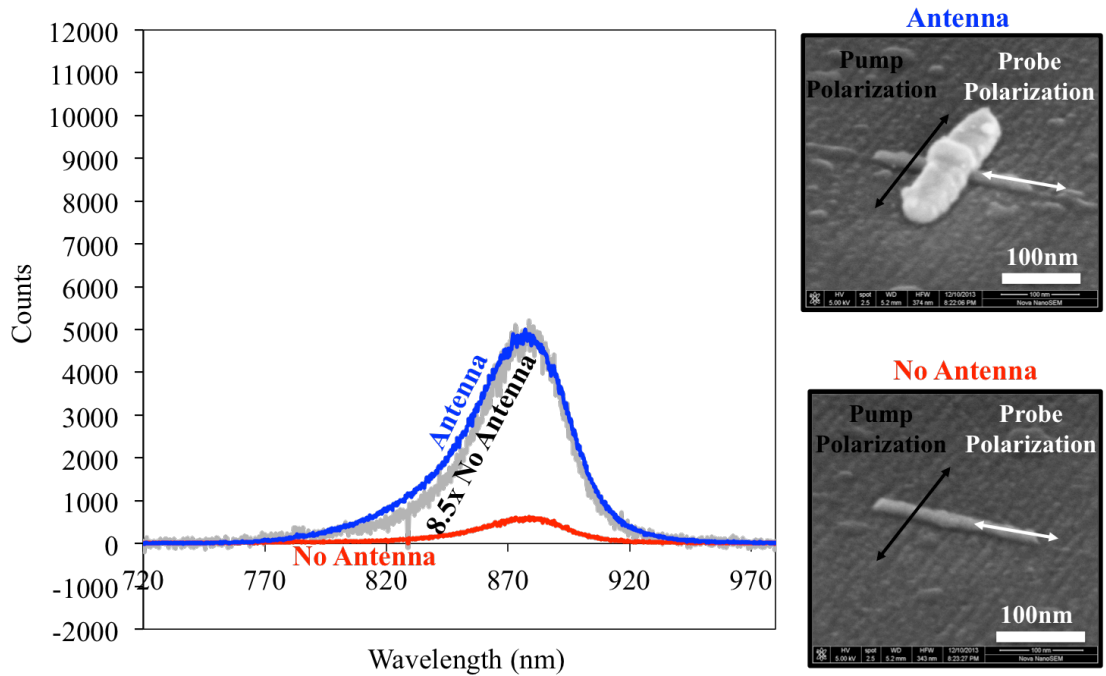
Figure 40. Measurement of pump enhancement. Blue corresponds to light from the antenna-coupled InP ridges. Red corresponds to bare InP ridges. The grey curve is 8.5x the bare case.

The resulting photoluminescence spectra are given in Figure 40. The antenna-coupled InP ridges show about 8.5x stronger signal than the bare InP ridges. This boost in signal is taken as a direct measurement of pump enhancement. These antennas were not designed to be resonant at the pump wavelength (720nm), so the pump enhancement is not especially large. Tuning the antenna to the pump wavelength would be very useful for applications where strong absorption in a small volume of semiconductor is desired. The pump enhancement correction factor may now be used to determine spontaneous emission enhancement.

5.4 Enhancement Results

The enhancement of spontaneous emission can now be characterized by taking photoluminescence spectra from the same devices in Figure 40, but in the antenna polarization. The antenna should strongly modify the spontaneous emission rate in the antenna polarization, which would result in much stronger photoluminescence signal from antenna-coupled devices than bare devices. A comparison between the measured spectra is shown in Figure 41.
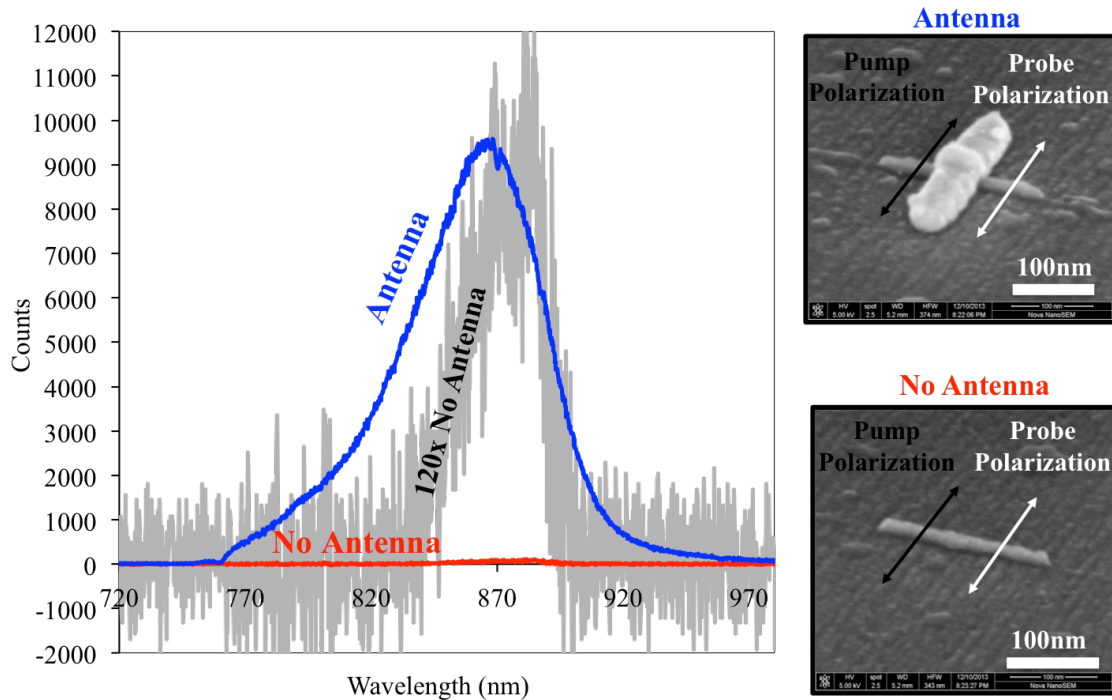
Figure 41. Photoluminescence enhancement of antenna-coupled InP ridges. Blue corresponds to light from the antenna-coupled InP ridges. Red corresponds to bare InP ridges. The grey curve is 120x the bare case.

The antenna-coupled InP ridges show about 120x greater photoluminescence signal than bare InP ridges. Taking into account the factor of 8.5x enhancement due to pump enhancement leaves a factor of 14x increase in quantum efficiency. The boost in quantum efficiency is a direct consequence of an increase in the spontaneous emission rate of the material as explained by (5.5).

A 14x increase in spontaneous emission falls short of the predicted enhancement shown in Figure 34. There are a few reasons why the experimental result falls short of the simulated enhancement. First, the arch-dipole antenna fabricated in this experiment is very sensitive to slight changes in geometry near the antenna gap. As a result, the antenna resonance may be shifted off the emission peak of the InP ridges and cause a reduction in enhancement. Also, the ohmic losses in the fabricated structure may be underestimated in simulation. A layer of 1-2nm of titanium was necessary to get good adhesion of gold during the antenna fabrication. Titanium is very absorbing at these optical frequencies, and would increase ohmic losses and reduce spontaneous emission enhancement.

In conclusion, a 14x enhancement of the spontaneous emission rate was demonstrated by coupling an InP ridge to an optical antenna. Additionally, the antenna-coupled devices showed a 120x increase in photoluminescence in the antenna polarization. The results presented here constitute experimental proof that optical antennas can be used to modify the spontaneous emission rate of a semiconductor. The antenna design used in this section is far from optimal, and will be improved upon in Chapter 6 of this dissertation.

6 Enhanced Spontaneous Emission from 2D Semiconductors

III-V semiconductors have dominated the field of optoelectronics due to a direct band-gap allowing efficient conversion between electron-hole pairs and light. Lasers, LEDs, and solar cells are always composed of III-Vs for this reason. However, a well-known property of these materials is that their surfaces are completely ridden with defects. Surface defects become non-radiative recombination centers if left uncapped. In optical antennas, where the gap of the antenna is preferably around 10nm, the surface to volume ratio is very large and surface recombination completely dominates. While a heterostructure could be used to clad the surfaces of the exposed semiconductor, the cladding layer needs to be around 10nm to effectively passivate the surface [56]. The additional thickness of a cladding layer on each side of the active semiconductor will limit the maximum achievable spontaneous emission enhancement. Instead, a semiconductor with pristine surfaces is desired.

6.1 2D Semiconductor Materials

Only recently a new class of semiconductors has been discovered which has opened the door for exciting new opportunities in solid-state and optoelectronic devices [57]. An entire family of transition-metal dichalcogenide materials exhibits a direct bandgap when reduced to a single monolayer. The quantum efficiency of these monolayers can be in the 0.01% to 1% range meaning that the surfaces have relatively few defects compared to III-V materials. Even more promising, recent results have shown that a super-acid surface treatment of MoS_2 monolayers can increase the quantum efficiency to over 95% [58].
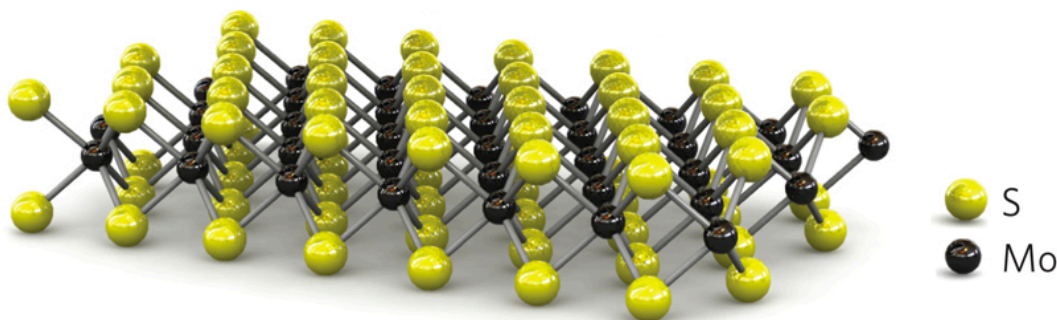
Figure 42. Atomic structure of the monolayer semiconductor MoS_2. Reproduced from [59]

The atomic structure of MoS_2 is shown in Figure 42. Other transition metal dichalcogenide monolayer materials such as WSe_2, WS_2, and $MoSe_2$ have a similar atomic structure. Each of these materials shows light emission in the 600-800nm wavelength range. These materials can also be contacted and electrically injected to form LEDs [60]. The high quality surfaces of 2D semiconductors make them intriguing candidates for the emitter in an antenna-enhanced LED. There have been some demonstrations of spontaneous emission enhancement of monolayer semiconductors, but none showing over 25x enhancement [61], [62]. The remainder of this section will focus on experimentally demonstrating large spontaneous emission enhancement in these 2D semiconductors.

6.2 Cavity-Backed Slot Antenna Resonances

The cavity-backed slot antenna discussed in Chapter 4 is an excellent design for coupling with 2D semiconductors. The location of maximum electric field in the fundamental mode of the cavity-backed slot antenna is at the base of the cavity. By placing the 2D semiconductor in this location, the spontaneous emission enhancement is maximized. The electric-field profile for the cavity-backed slot antenna is shown in Figure 43.
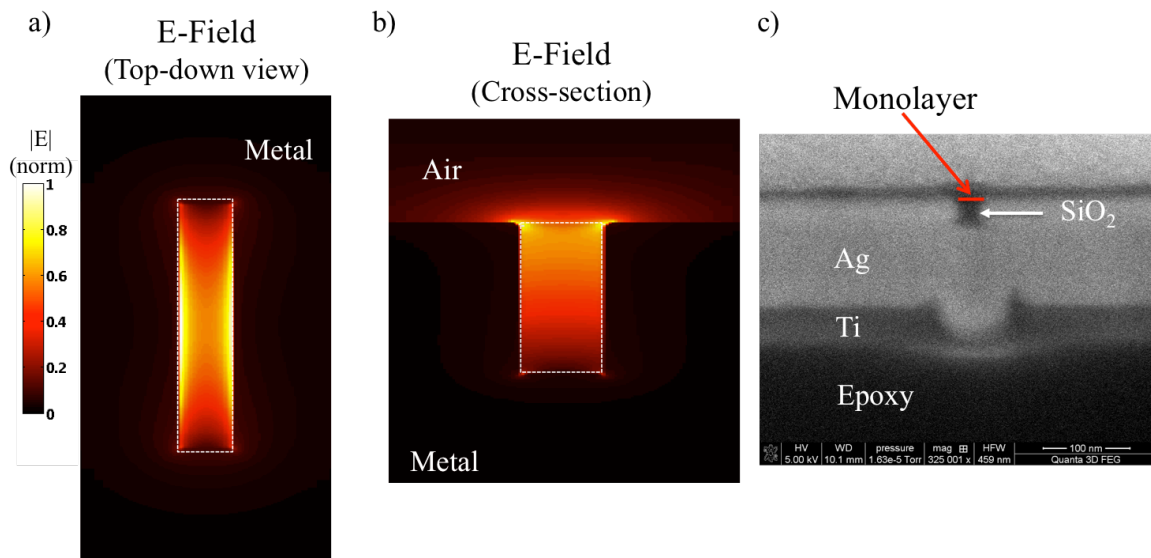
Figure 43. Electric-field profile for the fundamental mode of a cavity-backed slot antenna. a) Looking down on the slot shows the fundamental resonance is essentially a half-wavelength mode. The active material should be placed at the location of maximum electric field (at the top of the cavity as seen in b)) in order to maximize coupling to the antenna. c) The location of maximum monolayer coupling in shown in an SEM cross-section of a fabricated cavity-backed slot antenna.

An additional benefit of using 2D semiconductors with this antenna is that the emitter can be treated as only a small perturbation to the resonant properties of the antenna. If III-V

materials were used to fill the antenna slot, the resonance of the antenna would be changed drastically due to the substantial volume of high-index material. The length of the antenna would have to be reduced by roughly a factor of n in order to compensate for the resonance shift. A monolayer semiconductor, however, adds on a very small volume of high-index material to the antenna. The presence of the 2D semiconductor will cause a slight red-shift in the antennas resonance, but by only a few 10s of nanometers.

The resonances of cavity-backed slot antenna can be experimentally observed through a dark-field scattering measurement. The measurement is performed by illuminating the sample with a broadband light source through a dark-field objective. The dark-field objective restricts the illuminating light to a cone of high numerical aperture. Light incident upon the sample excites the optical antennas, which leads to some light reradiated (scattered) by the antenna. Light will be reradiated most strongly at the resonant wavelength of the antennas. By collecting a cone of light through the dark-field objective of numerical aperture less than the illumination, only light that has been scattered by antennas will be observed. Using this technique gives a simple method for determining the resonant frequency of cavity-backed slot antennas with different geometries.

The resulting dark-field images for arrays of cavity-backed slot antennas of various lengths are shown in Figure 44. The antennas appear as diffraction limited spots of color corresponding to their resonant wavelength. The antennas are spaced 2μm from their nearest neighbor. Each antenna has a cavity roughly 140nm deep, 43nm wide, and filled with exposed HSQ e-beam resist (similar to glass). Alignment marks in the top left of each image scatter the full spectrum of illumination light while the antennas preferentially scatter light at their resonant wavelength. There is a clear red-shift in antenna resonance as the length of the antenna slot increases.
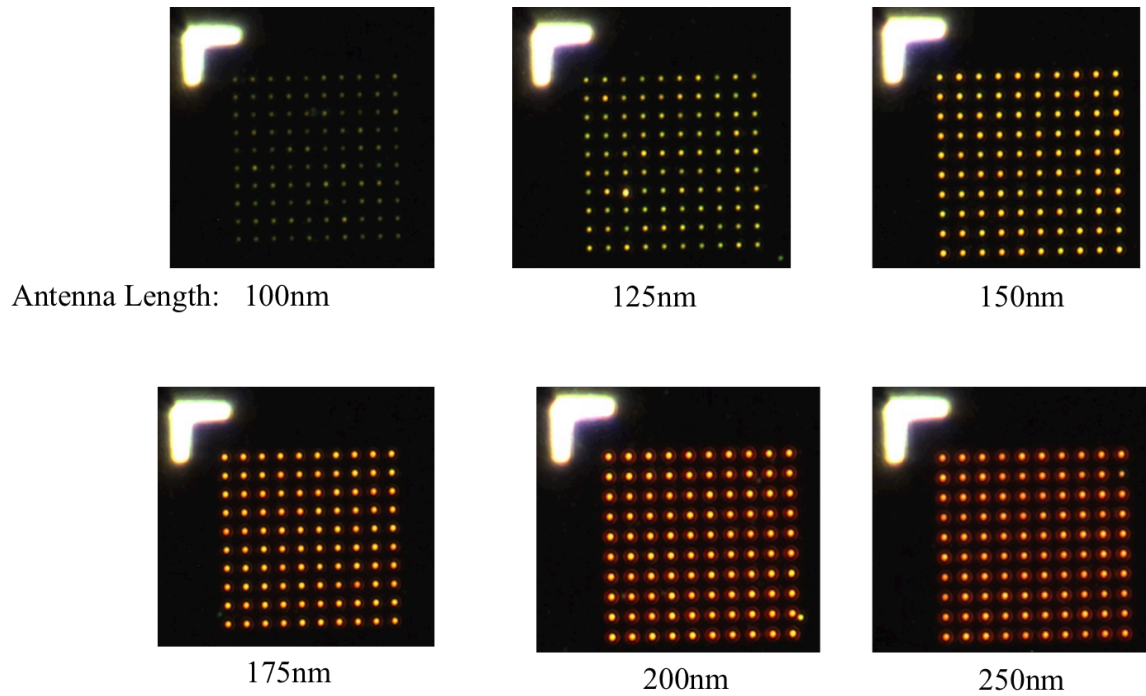
Figure 44. Dark-field images of arrays of cavity-backed slot antennas with increasing slot length. Each antenna has a cavity roughly 140nm deep, 43nm wide, and filled with air. The antenna spacing within an array is 2 μm. Alignment marks in the top left of each image scatter the full spectrum of illumination light while the antennas preferentially scatter light at their resonant wavelength.

As the length of the antennas increase beyond 250nm, the resonant wavelength will move to the infrared and cannot be observed with the naked eye. However, the antennas also have higher order resonances. For longer antennas this higher order resonance will move into the visible regime and can be viewed via the dark field microscope. An example of such a higher order resonance is shown in Figure 45 for an array of cavity-backed slot antennas with 450nm length.
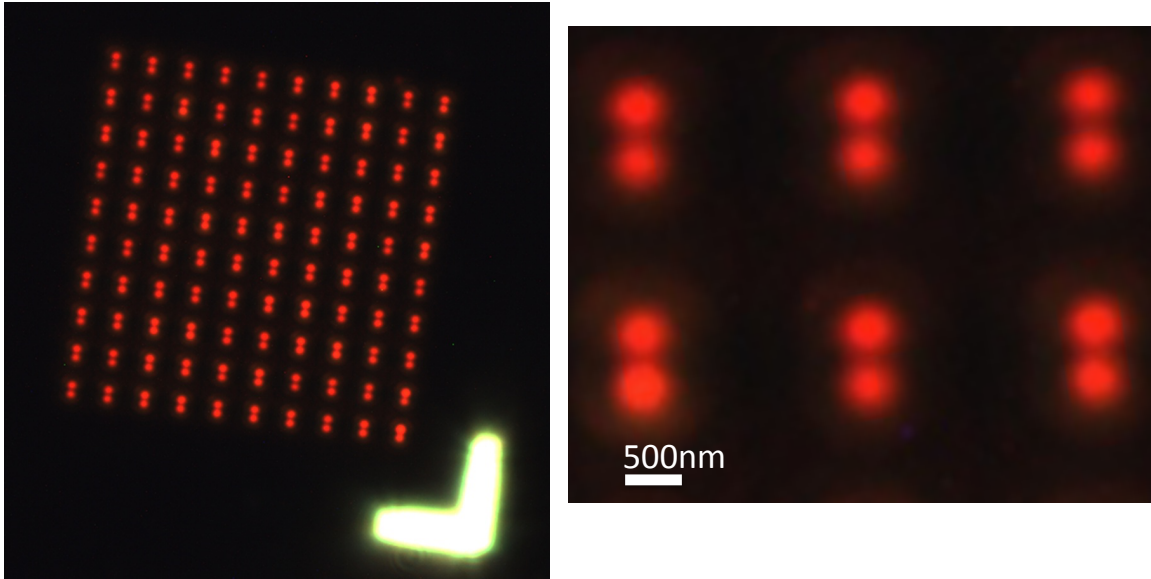
Figure 45. Dark field images of 450nm long cavity-back slot antennas. The cavity is filled with exposed HSQ e-beam resist (similar to glass). The scattering image shows two lobes corresponding to a higher order resonance of the antennas.

Using the same dark-field technique, the scattering spectrum for each array of antennas may also be taken. These spectra are shown in Figure 46 for antennas with length increasing from 100 to 400nm. The first order resonance can be seen for antennas with lengths from 100-300nm. The first order resonance for 350 and 400nm is cutoff by long wavelength limit of the detector, but a higher order resonance is observed around 700nm.
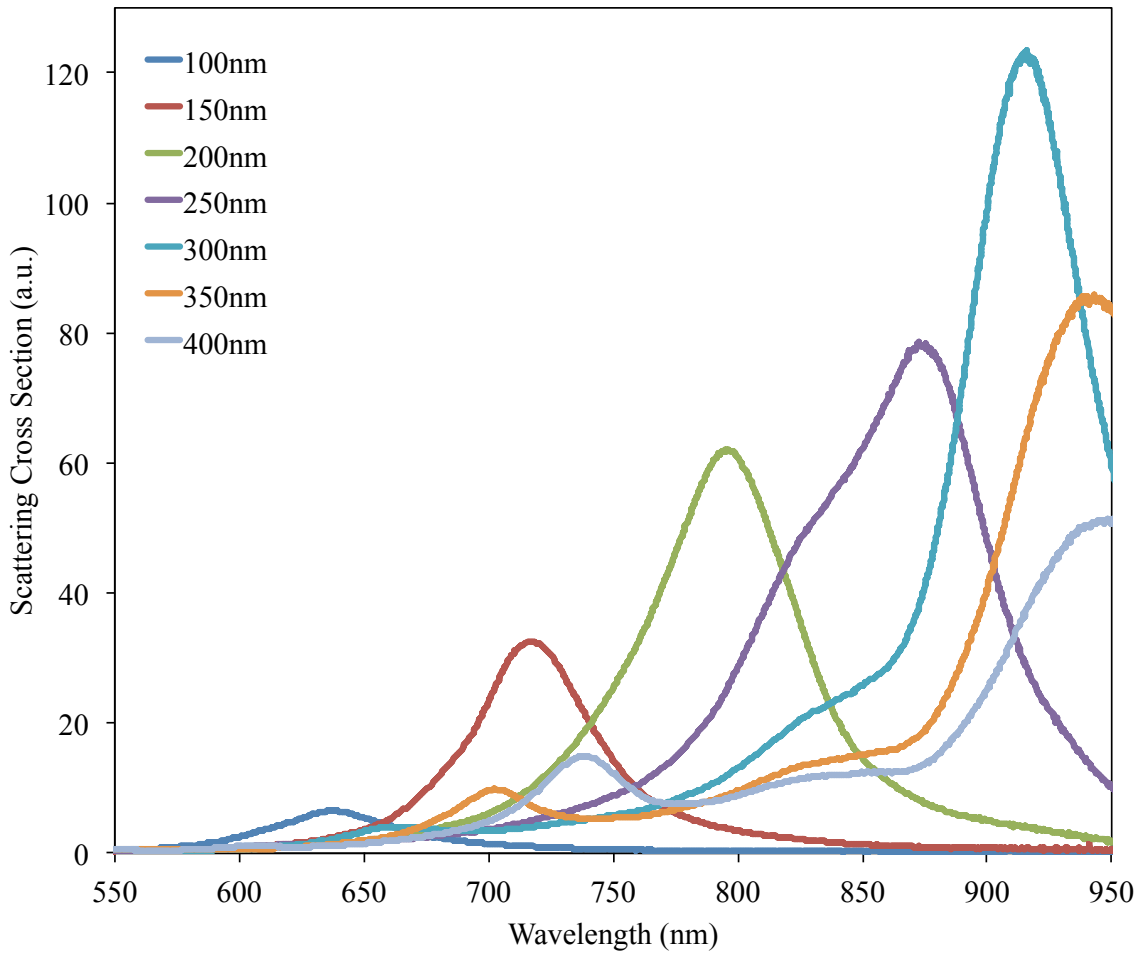
Figure 46. Slot antenna scattering spectra for lengths from 100-400nm. The cavity of the antennas is roughly 40nm wide, 140nm deep and filled with exposed HSQ e-beam resist. The long wavelength limit of the detector cuts off the first order resonances for the 350 and 400nm antennas.

A notable feature of the results in Figure 46 is that the scattering cross section increases as the resonant wavelength of the antennas increase. This is a very fundamental property of antennas and applies even in the optical regime. For a receiving antenna, one can define a capture cross section, A_c. This quantity describes how much power will be delivered to a load, P_L, from an incoming plane wave with intensity I through the relation $A_c = P_L/I$. Using the reciprocal nature of Maxwell's equations, one can derive an expression for the capture cross-section of an antenna in terms of its resonant wavelength, λ, and directivity, D [4]. If the load resistance is matched to the antenna, the capture cross section becomes:

$$A_c = \frac{\lambda^2}{4\pi} D \qquad (6.1)$$

Similarly, a scattering cross section can be defined to relate how much power will be re-radiated by the antenna from an incoming plane wave. If the load is an open circuit, the radiation cross section becomes:

$$A_{rad} = \frac{\lambda^2}{\pi} D \qquad (6.2)$$

The dependence of A_{rad} on λ^2 is clearly demonstrated in Figure 46. These results further demonstrate the equivalence between optical antennas and conventional microwave antennas. Equations (6.1) and (6.2) lead one to consider the possibility of using optical antennas to efficiently focus light from a source, or to emit light preferentially in a certain direction. Potential applications of using optical antennas in this way are sub-diffraction limit imaging [63], focusing laser light for heat-assisted magnetic recording (HAMR) [64], and optical wavelength beam steering [65].
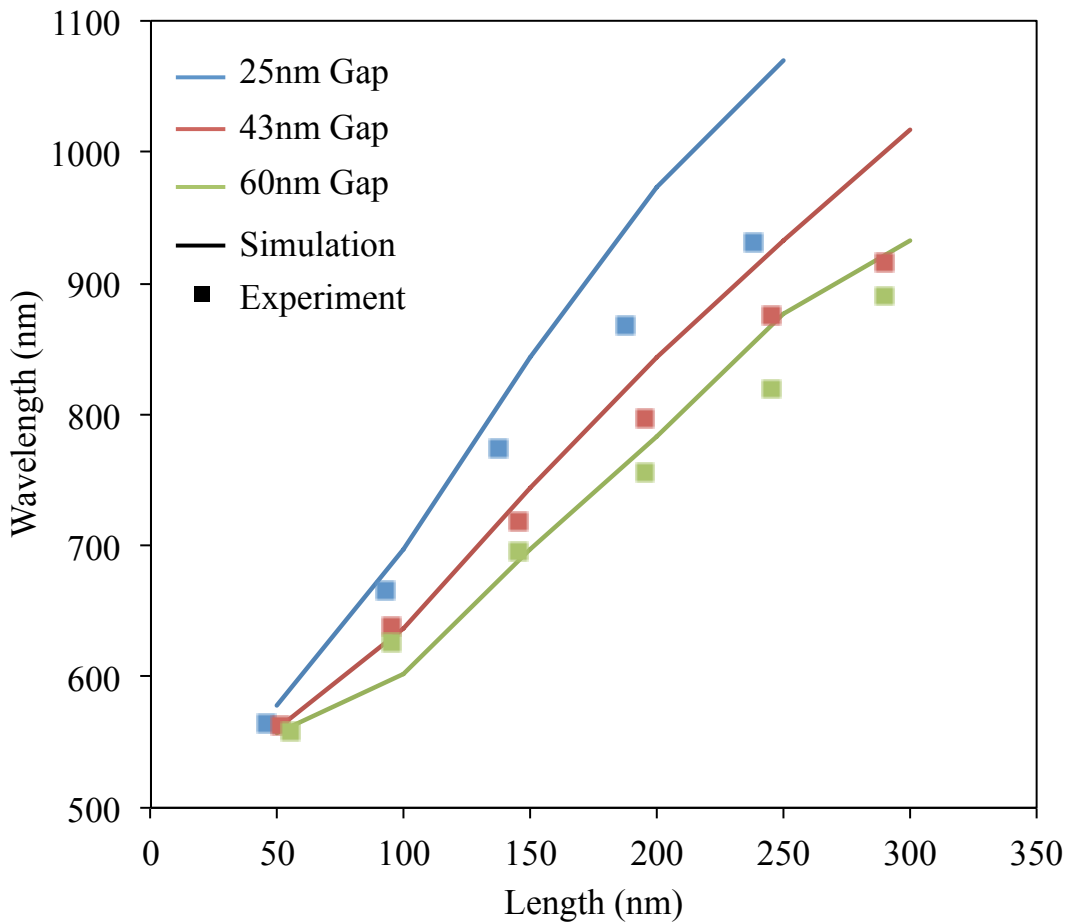
Figure 47. Slot antenna resonant wavelength for various antenna slot lengths and gap widths. The antenna slot is filled with a 140nm deep ridge of exposed HSQ e-beam resist. Points correspond to experimental results while lines come from simulation.

A comparison between the resonant wavelength of the cavity-backed slot antennas measured in Figure 46 and the resonant wavelength predicted by simulation is shown in Figure 47. There is a slight discrepancy between the experimental data and the resonance predicted by simulation. The mismatch is most likely due to the imperfect fabrication of the cavity-backed slot antennas. Nevertheless, the general trends of resonant shift predicted by simulation in terms of antenna length and gap width were confirmed by the experiment. Once the resonant wavelength of the antennas is know, an array can be chosen to match the emission spectrum of the desired 2D semiconductor so that the maximum spontaneous emission enhancement can be attained.

6.3 WSe$_2$ Enhancement

The cavity-backed slot antenna was used to demonstrate spontaneous emission enhancement in monolayer WSe$_2$ [40], [66]. This 2D semiconductor emits light at a peak wavelength at 760nm and quantum efficiency on the order of 1%. The WSe$_2$ monolayer in this experiment was restricted only to the "hotspot" of the antenna mode. Similar structures were fabricated without metal present in order to quantify the relative benefit in quantum efficiency due to the optical antenna. The fabrication process for these devices is outlined below.
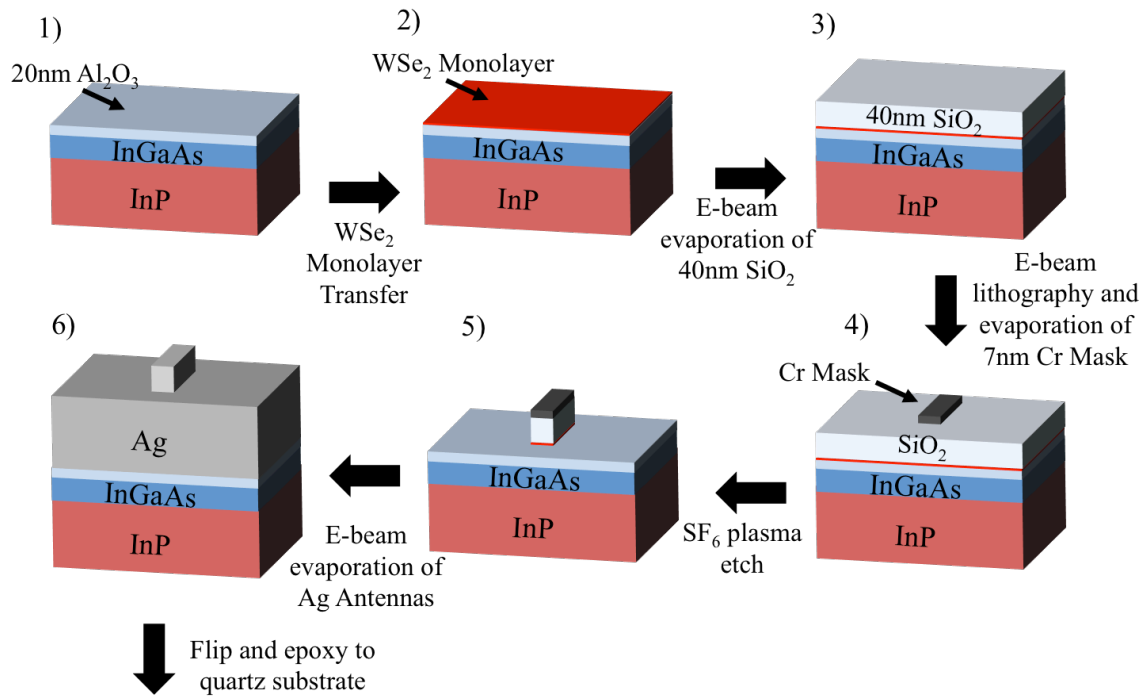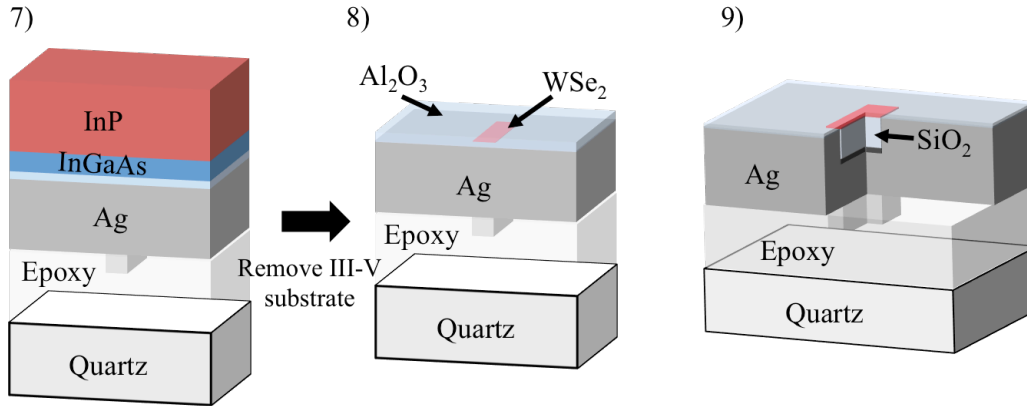
Figure 48. Process flow for fabrication of WSe$_2$ coupled to Ag cavity-backed slot antennas. Bare samples follow the same process with the exception of the Ag evaporation in step 6. A cross-section of the completed device is shown in 9).

A sacrificial substrate consisting an epitaxial grown InGaAs etch stop on InP is used to begin the fabrication process. A 20nm layer of Al$_2$O$_3$ is deposited on the substrate by atomic layer deposition. This layer will serve as a protective layer for the Ag once the devices are completed. The WSe$_2$ monolayer is then transferred to the substrate. These monolayers are obtained by exfoliation to a Si/SiO$_2$ substrate and transferred with a layer of PMMA. Next, a 40nm layer of SiO$_2$ is deposited by e-beam evaporation. The SiO$_2$ will form the cavity of the antenna, so the thickness of the layer will determine the cavity depth. A Cr hard mask is then fabricated by e-beam lithography and development of PMMA A2 resist followed by e-beam evaporation and liftoff. The width of the Cr mask determines the antenna slot width, which limits the maximum attainable spontaneous emission enhancement. The devices presented here had slot widths of around 30nm. The unmasked SiO$_2$ and WSe$_2$ are then etched away in SF$_6$ plasma for 40-50 seconds. The remaining ridge is shown in step 5 of Figure 48.

The metal forming the antenna is now deposited by e-beam evaporation. Silver was chosen due to its low loss at optical frequencies. A thick layer (>200nm) was deposited to completely cover the top surface of the substrate. An extra 20nm of Ti was then deposited to improve adhesion during the subsequent substrate removal process. Devices fabricated to serve as bare WSe$_2$ emitters were fabricated following the same process with the exception of the Ag evaporation in step 6.

The substrate is then removed following the same InP removal process described earlier chapter 5. First, the majority of the InP substrate is mechanically lapped away using 1500 grit silicone. The remaining InP and InGaAs layers are removed in HCl:H$_3$PO$_4$ (1:1) and H$_2$SO$_4$:H$_2$O$_2$:H$_2$O (1:1:10), respectively. The final structure is shown in step 9 of Figure 48. The initial 20nm protective layer of Al$_2$O$_3$ is still present to prevent the reaction of silver with sulfur in the ambient environment. Critically, at no point in the process does the silver surface of the cavity-backed slot antenna come in contact with ambient air conditions.
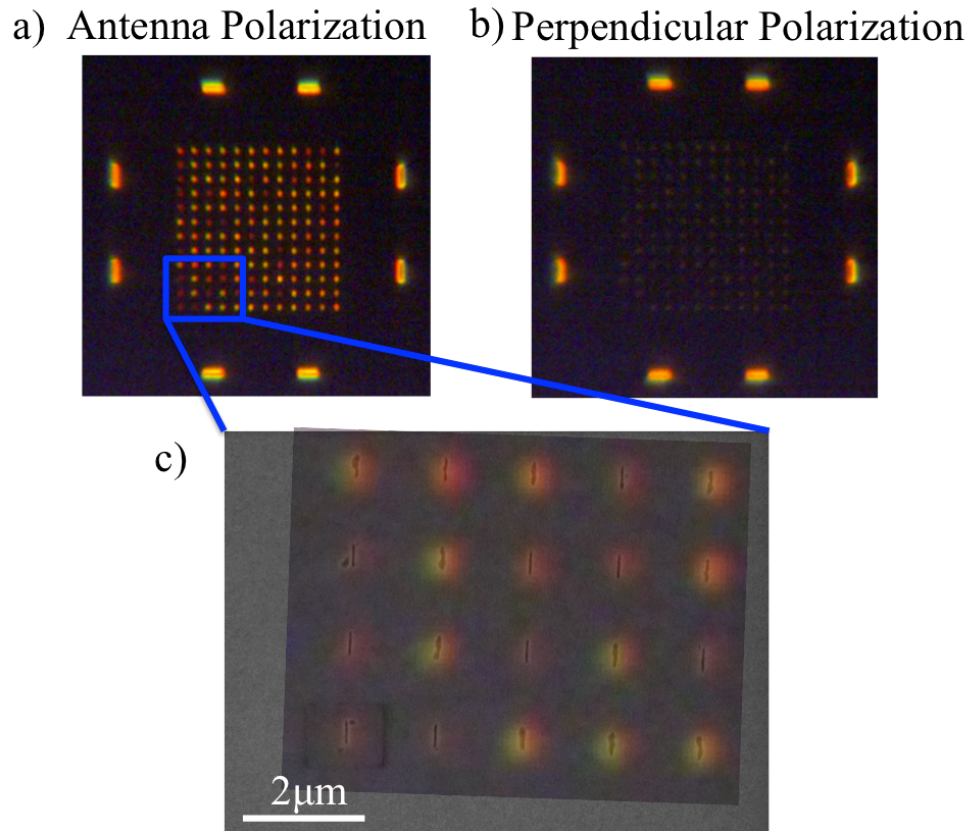
Figure 49. Dark-field images of silver cavity-backed slot antennas in the a) antenna polarization and b) perpendicular polarization. The SEM image in c) is overlayed with the dark-field image in a). Antennas slots with defects show a resonance in the visible while smooth antenna slots are resonant in the infrared.

The silver cavity-backed slot antennas fabricated by this method have significant variation from antenna to antenna. Dark-field images of an array of silver cavity-backed antennas are shown in Figure 49a. Even though each antenna in the array was formed using the same dimensions, there is a significant variation in their resonant frequencies. The SEM image in Figure 49c is overlayed with the dark field image in a) revealing the cause of the variation in resonance. These antennas were designed to be resonant at 770nm, so an ideal slot should appear a very deep red in a dark-field image. Interestingly, the slots that have defects (seen in c)) have a blue-shifted resonance and appear yellow-orange in the dark-field image. The variation in resonant frequency will impact the amount of spontaneous emission enhancement observed by each antenna-coupled WSe_2 device due to the required matching of resonant frequency to emission wavelength.
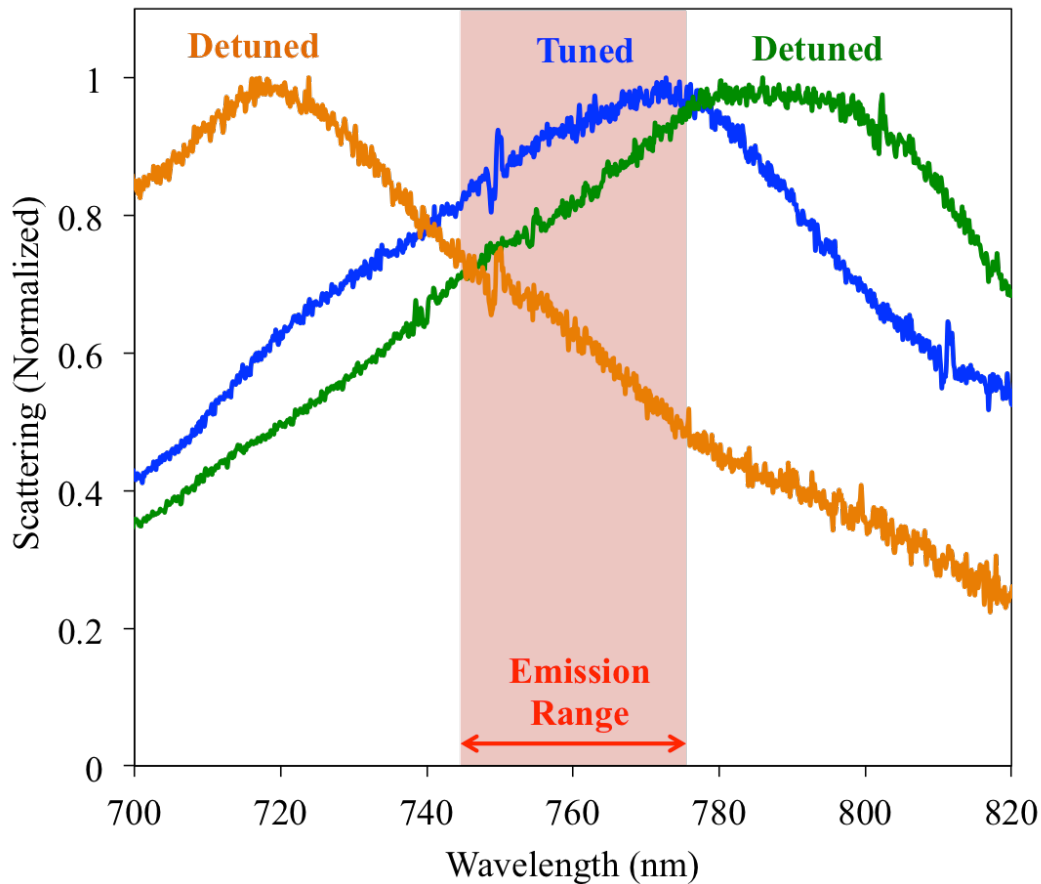
Figure 50. Scattering spectra of silver cavity-backed slot antennas used for spontaneous emission enhancement in WSe$_2$. Orange and green curves correspond to antennas poorly matched to the wavelength of emission of WSe$_2$. The blue curve shows the scattering spectra of a tuned antenna.

The variation in antenna resonant frequency can be seen in the scattering spectra of the antennas. Dark-field scattering spectra of the silver cavity-back slot antennas coupled to WSe$_2$ are shown in Figure 50. While each curve is dominated by the scattering from a single antenna, some light from nearby antennas in the array is incorporated in the measured spectra. Additionally, defects on the sample surface cause additional scattered light, which can broaden the resonances observed above. The blue curve shows a fairly good match in resonance to the wavelength range of light emission from WSe$_2$, so this antenna is expected to have the largest spontaneous emission enhancement of the three. The green and orange curves are not well matched, and should show a corresponding decrease in enhancement. The antennas measured here were used in the photoluminescence measurements discussed next.
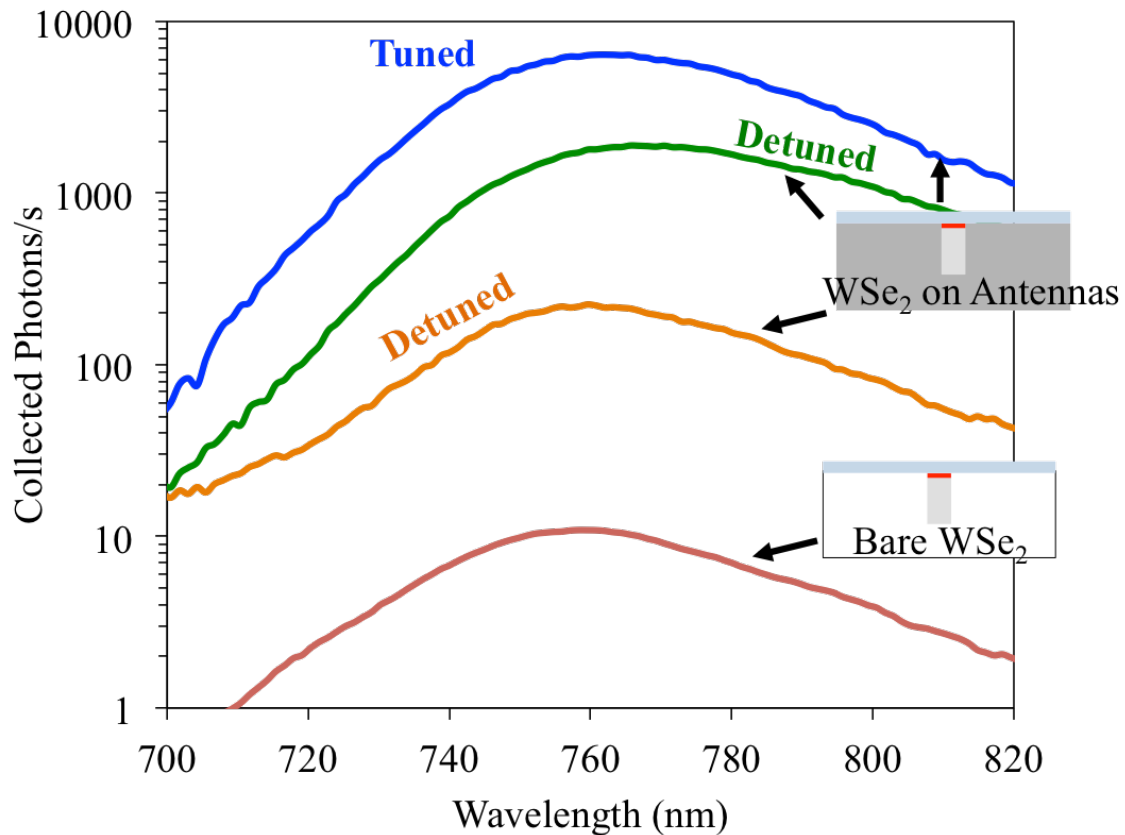
Figure 51. Photoluminesccnce data from etched WSe$_2$ monolayers. When coupled to a cavity-backed slot antenna the WSe$_2$ emission was enhanced. Antennas with resonances not tuned to the emission wavelength of WSe$_2$ only enhanced the collected signal by 20x (orange) and 190x (green). The antenna tuned to the emission wavelength of WSe$_2$ enhanced the collected PL signal by 700x.

Photoluminescence measurements were performed on both samples with and without the silver cavity-backed slot antennas. Excitation of carriers in the WSe$_2$ was provided by a 532nm CW laser polarized perpendicular to the antenna mode. The laser was focused on the sample using a 100x 0.8NA objective, and PL was collected through the same objective. After filtering out the pump laser using dichroic and long-pass filters, the PL was directed to a grating. The resulting PL spectra were measured using a liquid nitrogen cooled Si CCD.

The PL measured for various antenna-coupled devices and for the bare WSe$_2$ is shown in Figure 51. The WSe$_2$ emission was enhanced when coupled to a cavity-backed slot antenna over the case when no silver antenna was present. Antennas with resonances not tuned to the emission wavelength of WSe$_2$ only enhanced the collected signal by 20x

(orange) and 190x (green). The antenna tuned to the emission wavelength of WSe_2 enhanced the collected PL signal by 700x (blue).

As discussed earlier, an increase in quantum efficiency is evidence of an increase in the spontaneous emission rate of the active material. A few experimental correction factors must be accounted for in order to extract the boost in quantum efficiency from the PL data shown in Figure 51. First, the pump intensity seen by the WSe_2 monolayer with and without an antenna will be slightly modified. The pump laser was polarized perpendicular to the antenna mode to mitigate this effect, but there will still be a small correction factor. FDTD simulations of the polarized 532nm laser show that pump intensity is enhanced by a factor of 1.6x for the antenna devices over bare devices. Second, the cavity-backed slot antenna emits radiation only into the upper hemisphere. The bare WSe_2 devices will emit radiation in all directions. The emission will from bare devices will be slightly stronger down into the substrate than up into free-space due to the substrate index of 1.5. The result of the difference in radiation pattern between the two cases is a 2.8x increase in collection efficiency from antenna-coupled devices. Lastly, the cavity-backed slot antenna will only enhance emission from dipoles in WSe_2 that are oriented in the antenna polarization. Therefore, the unpolarized bare WSe_2 emission must be reduced by a factor of 2x.

Together, the pump intensity, radiation pattern, and polarization factors result in a reduction of 2.2x to convert enhancement of collected PL signal shown in Figure 51 to enhancement of quantum efficiency. Therefore, the tuned antenna resulted in a 318x increase in quantum efficiency. The enhancement is a direct result of an increased spontaneous emission rate in WSe_2. The goal set at the beginning of this dissertation was to demonstrate a 200x enhancement to show that spontaneous emission can be faster than the fastest stimulated emission. These results indicate that such a large spontaneous emission enhancement is possible and has been observed.

6.4 MoS_2 Enhancement

The results presented in the previous section using monolayer WSe_2 show very high spontaneous emission enhancement, but the overall quantum efficiency was still low (1% range). The process of etching the WSe_2 monolayer into small rectangles creates defects at the edges leading to a large increase in non-radiative recombination. In the following experiment, the monolayer semiconductor is left unetched in order to mitigate edge recombination. MoS_2 was chosen as the semiconductor emitter in order to demonstrate that both high quantum efficiency and fast spontaneous emission is possible. With a superacid surface treatment, MoS_2 has shown over 95% quantum efficiency [58]. Here, a monolayer of MoS_2 will be coupled to gold cavity-backed slot antennas. A comparison of quantum efficiency of the flake before and after transfer to the optical antenna array will indicate the amount of spontaneous emission enhancement.

6.4.1 Device Fabrication

The process of fabricating the optical antennas for MoS_2 spontaneous emission enhancement begins by making the cavity-backed slot antennas. The process flow is detailed in Figure 52. A sacrificial substrate composed of an InP substrate with alternating InP and InGaAs etch stop layers is initially used to carry the patterned antenna slots. A layer of HSQ e-beam resist is then spun on. The thickness of the HSQ layer will determine the depth of the antenna cavity and was chosen to be roughly 80nm for these devices. E-beam lithography is used to pattern the lateral dimension of the antenna slots. A range of lengths from 100-400nm and widths from 20-60nm were used. The unexposed HSQ can then be removed by placing the sample in TMAH for 60 seconds.

The metal for the optical antenna is then deposited by e-beam evaporation. A very thin layer of titanium (0.5nm) was used to provide adhesion sites for the gold layer. Next, a 200nm gold layer was evaporated with a chamber pressure of 2e-6 torr at a deposition rate of around 0.3nm/sec. The sample was mounted inside the chamber on a tilting stage. As gold was being evaporated, the sample was rotated around the long axis of the antennas. In situ tilting was important for eliminating sidewall defects in the final antenna structure. Without tilting during evaporation, the gold would not sufficiently cover the sidewalls of the HSQ ridges, which leads to more variation in the final antenna properties.
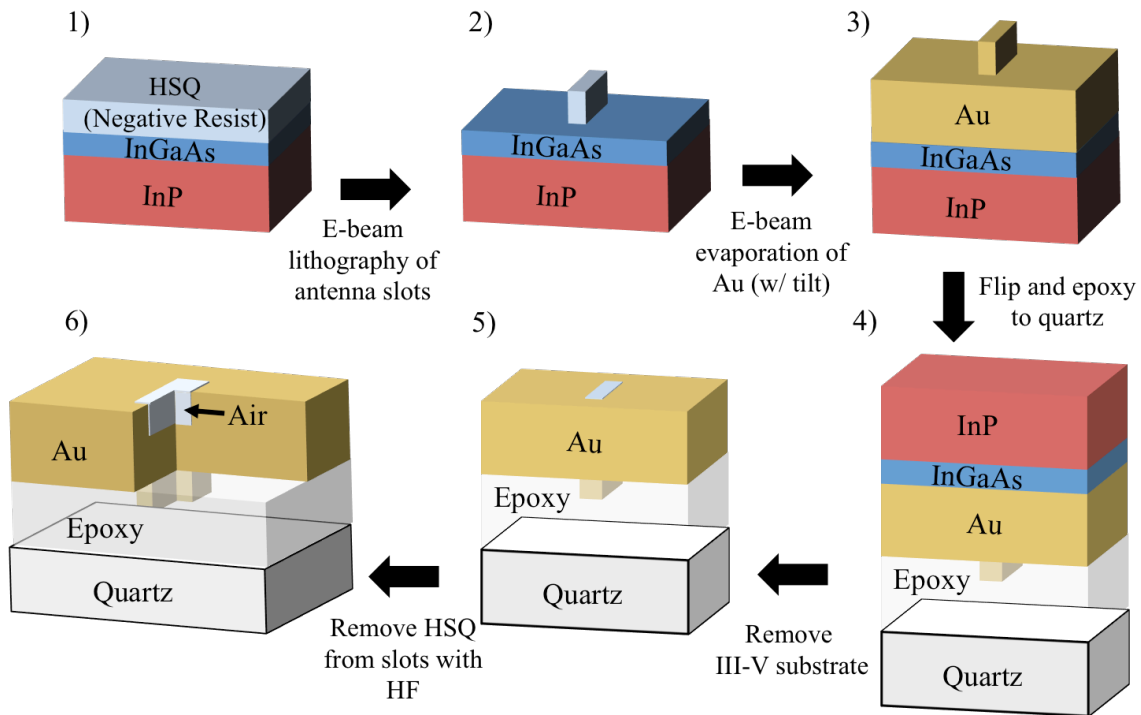
Figure 52. Process flow for gold cavity-backed slot antenna fabrication.

After gold evaporation, a capping layer of 20nm titanium was used to improve adhesion during the substrate removal process. The sample was flipped over and bonded to a quartz slide using optical epoxy (Norland's Optical Adhesive 81). Following the same

mechanical lapping and etching process as described in Figure 35, the III-V substrate materials were removed. The resulting structure reveals arrays of cavity-backed slot antennas that are filled with exposed HSQ e-beam resist. Finally, the HSQ can be removed by a 10sec etch in 1:10 buffered HF. As an added benefit, the HF will also remove the thin titanium layer that was initially deposited for adhesion purposes.
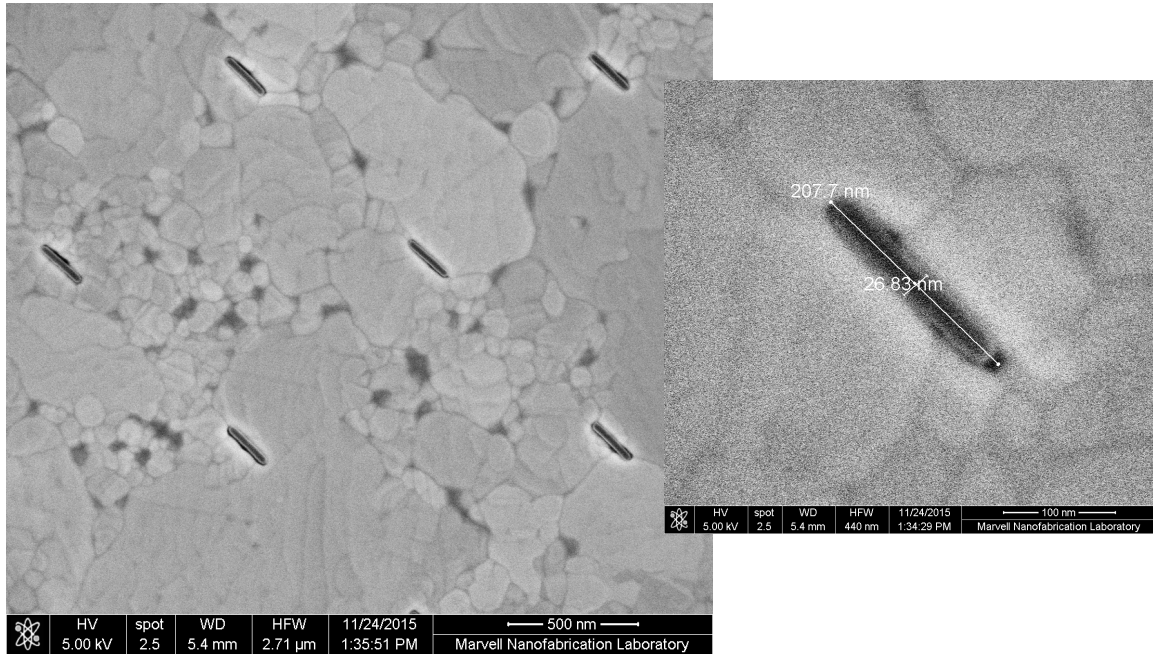
Figure 53. SEM images of cavity-backed slot antennas before HSQ removal. Slot antenna gap widths down to 25nm were achieved.

An example of the fabricated antennas after substrate removal is shown in Figure 53. Slot antenna gap widths down to 25nm were achieved. The gold surface is very smooth due to the evaporation onto an epitaxially grown wafer followed by substrate removal. Also, the large grain size of gold visible in Figure 53 suggests that the metal is of high quality.

After completing the fabrication of arrays of cavity-backed slot antennas, the resonances of each array can be measured by dark-field scattering. As shown in Figure 54, the peak emission wavelength of monolayer MoS_2 is around 660nm. The antenna array with length of around 275nm, and gap width of roughly 25nm was chosen to match well to the 660nm emission wavelength.
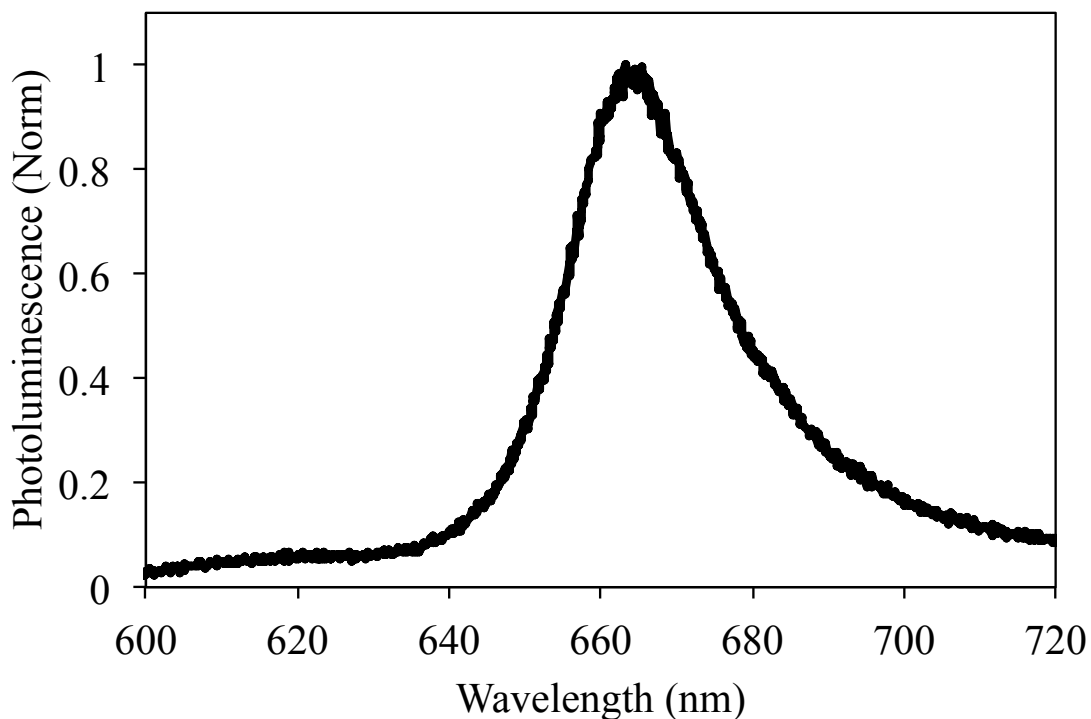
Figure 54. Photoluminescence spectrum of an as exfoliated monolayer of MoS_2

The transfer process used to locate the MoS_2 monolayer on the desired array of antennas is outlined in Figure 55. The monolayer is initially exfoliated onto a Si/SiO_2 substrate. The SiO_2 layer is 90nm thick and provides good optical contrast so that monolayers can be distinguished from multilayers. A layer of PMMA is spun on the Si/SiO_2 substrate, and a small section around the monolayer is cut out for transfer. The MoS_2 monolayer sticks to the PMMA when it is lifted from the substrate and placed at the desired location on the antenna substrate. Finally, the PMMA is removed in an acetone bath.
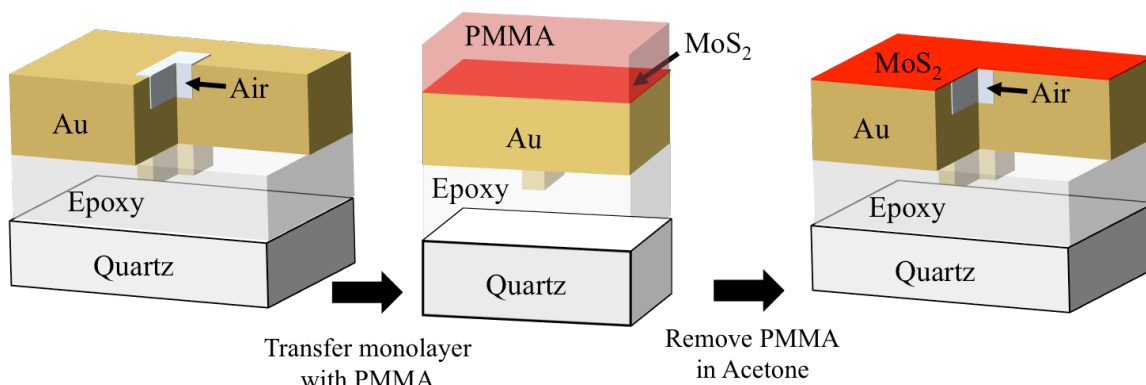
Figure 55. MoS_2 monolayer transfer process.

An image of a MoS$_2$ monolayer after it has been transferred to an antenna array is shown in Figure 56. The monolayer appears very faintly over the array due to its approximately 5% absorptivity [67]. Each antenna in the array can be seen as a dark spot in the image due to their absorption in the visible range. The spacing between each antenna is 1μm, and the monolayer is around 10μm in sized.
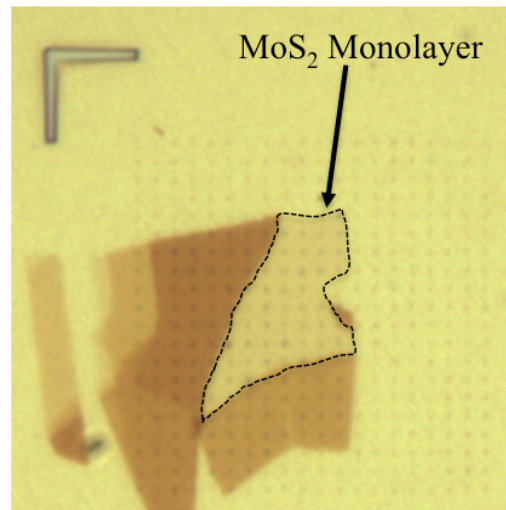
Figure 56. MoS$_2$ monolayer on an antenna array of the transfer process. The monolayer appears very faintly so it is outlined. The antennas appear as dark spots in the image due to their absorption of light. The spacing between each antenna is 1μm.

6.4.2 Experimental Results

The quantum efficiency and spontaneous emission enhancement of the MoS$_2$ coupled to optical antennas can now be obtained through photoluminescence measurements. A CW laser at 532nm was used as to excite carriers in the MoS$_2$ monolayer. The same pump power of 1.5μW was measured coming out of the objective for all measurements. Photoluminescence was collected through the same 100x, 0.8NA objective that was used for pumping. Dichroic and long-pass filters were used to separate PL from the pump laser. The PL signal was then directed to a spectrometer and detected by a liquid nitrogen cooled Si CCD.

Photoluminescence was taken on a monolayer of MoS$_2$ after it was exfoliated onto the Si/SiO$_2$ substrate. This measurement gives the baseline quantum efficiency for the experiment. The same measurement was performed on the same MoS$_2$ monolayer after it was transferred to the optical antenna array. The resulting signal in raw counts from the

Si CCD is shown in Figure 57. There is an approximately 4x increase in total PL signal coming from the MoS_2 coupled to antennas over MoS_2 on a Si/SiO_2 substrate.
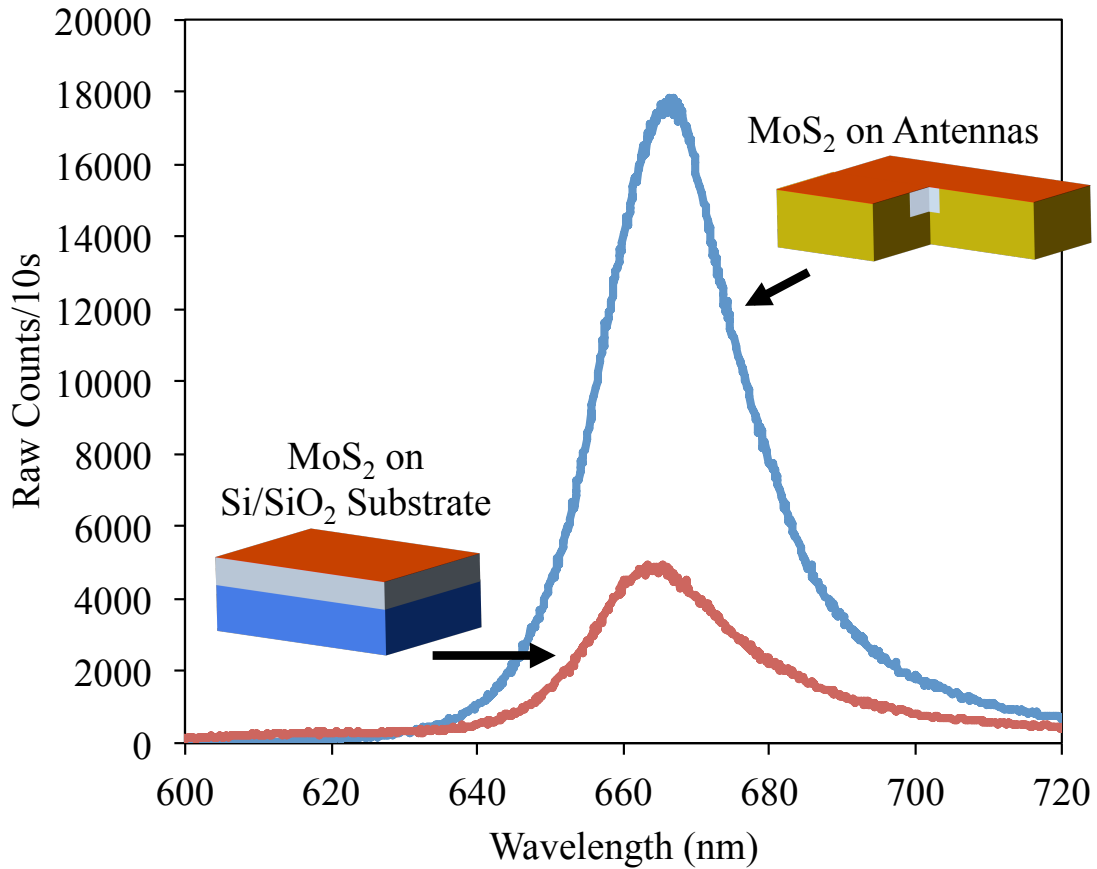
Figure 57. Raw photoluminescence data before and after transfer of a MoS_2 monolayer from Si/SiO_2 substrate to an optical antenna array.

In order to interpret these results, we must first notice that the majority of the area of the transferred MoS_2 monolayer is not in the "hotspot" of the optical antennas. Most of the monolayer is directly above the gold surface and does not couple to an optical antenna at all. Based on the earlier discussion in this dissertation of dipole emitters the approach metal surfaces, we should expect very inefficient emission from the MoS_2 everywhere outside of the slot of the optical antennas. A diagram showing the spatial dependence of expected PL efficiency is given in Figure 58.
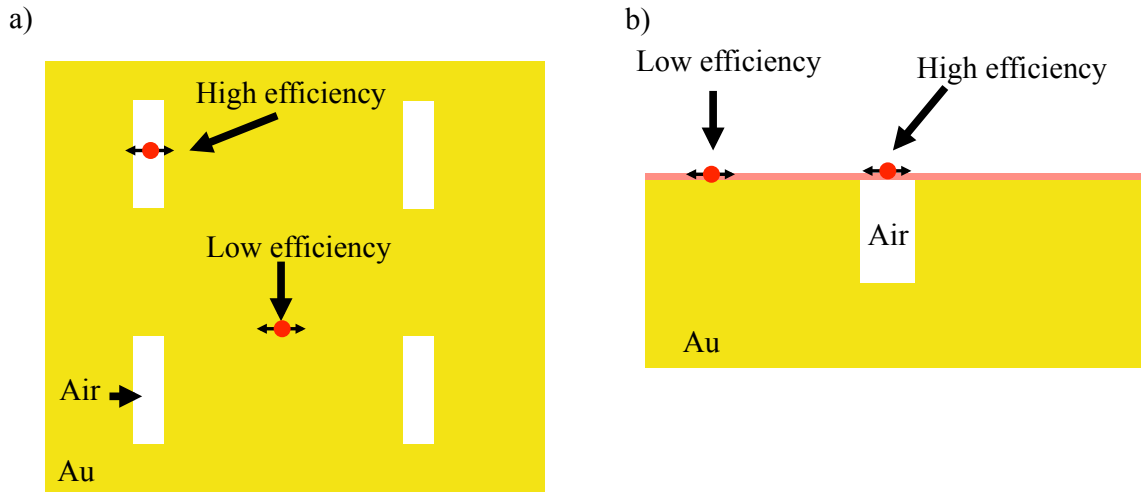
Figure 58. Spatial dependence of radiation efficiency. The spontaneous emission rate will be enhanced in MoS$_2$ located inside the slot of each antenna leading to efficient PL. MoS$_2$ outside the antenna slots will be dominated by emission into ohmic losses in the gold and lead to inefficient PL. a) Top-down diagram of spatial dependence of PL efficiency. b) Cross-section of spatial dependence of PL efficiency.

Images of the PL emitted by the antenna-coupled MoS$_2$ monolayer show exactly the behavior one would expect. There is a bright PL spot located at each antenna location, with a spacing corresponding to the antenna array spacing of 1µm. Also, the PL is strongly polarized. Spatial images of PL emission in the antenna polarization and perpendicular to the antenna polarization are shown in Figure 59. Antenna polarized PL is strong and confined to the location of antennas, while perpendicular polarized PL is weak and broad area.
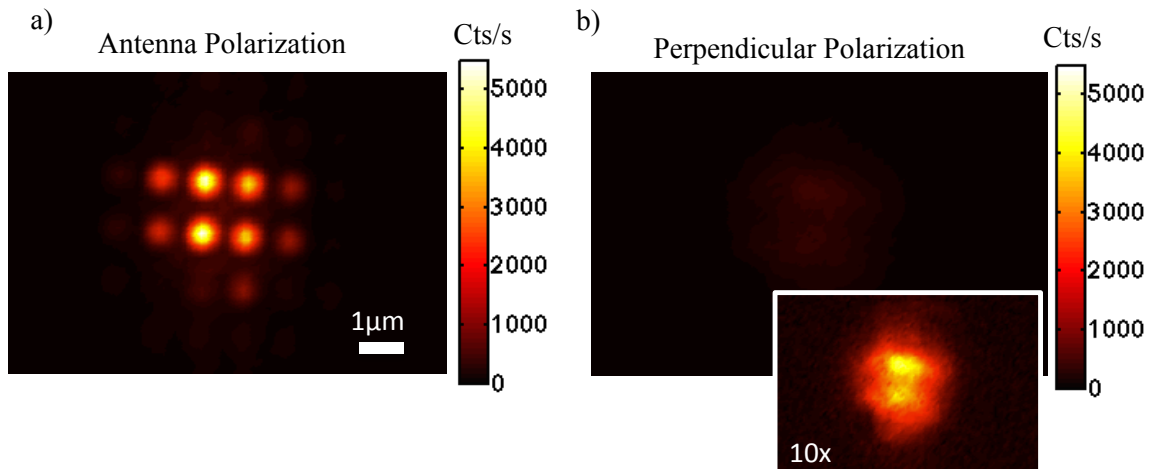
Figure 59. Spatial dependence of photoluminescence emitted by a MoS$_2$ monolayer coupled to an array of optical antennas.

The results shown in Figure 59 are confirmation of the influence of the antennas on the spontaneous emission from the MoS$_2$ monolayer. The strong polarization ratio of PL emission from the optical antennas arises from the fact that the antennas only enhance the spontaneous emission rate of the antenna polarization. This is also evidence that the spatial dependence of the PL is not due to changes in the pump intensity. If the antenna were causing greater absorption of pump light, the emission intensity would have increased for both the antenna and perpendicular polarizations.

Now that the spatial distribution of PL emission is known to be confined only to the area of the antennas, we may apply a correction factor to the raw data in Figure 57. The area occupied by antennas is around 111x less than the full area of the MoS$_2$. Therefore, to compare the intensity of emission from the antenna-coupled MoS$_2$ to the as exfoliated MoS$_2$, we must multiply the antenna PL signal by this factor.

The pump intensity seen by the monolayer and the collection efficiency of the optical setup must be accounted for in order to convert from the raw PL signals to quantum efficiency. The pump laser was polarized perpendicular to the polarization of the antennas to mitigate any pump enhancement. Optical simulations of the 90nm SiO$_2$ on Si substrate show that constructive interference due to the dielectric stack leads to a stronger pump intensity for the as exfoliated case than the antenna case by a factor of 2.2x.

The cavity-backed slot antenna emits light only into the hemisphere above the sample, which leads to greater collection efficiency than the as exfoliated case. Optical simulations of the two cases show that the collection efficiency will be 2.7x greater for the antenna case than the as exfoliated case. Finally, the throughput of the optical setup must be calibrated in order to estimate the absolute quantum efficiency for each case. Calibration was performed by illuminating a piece of spectralon (diffuse lambertian reflector) with a red laser. The spectral dependence of throughput was determined using a calibrated blackbody source. Both the antenna polarization and perpendicular polarizations were calibrated to account for the polarization dependence of all optics in the PL beam path.

The calibrated photoluminescence spectra for the same MoS$_2$ before and after transfer to the optical antennas is shown in Figure 60. By integrating over the full spectrum, we can estimate the absolute quantum efficiency of the MoS$_2$ monolayer in each case. The as exfoliated flake shows 0.025% efficiency while the antenna-coupled MoS$_2$ has 7% quantum efficiency. The resulting boost in quantum efficiency is 280x.
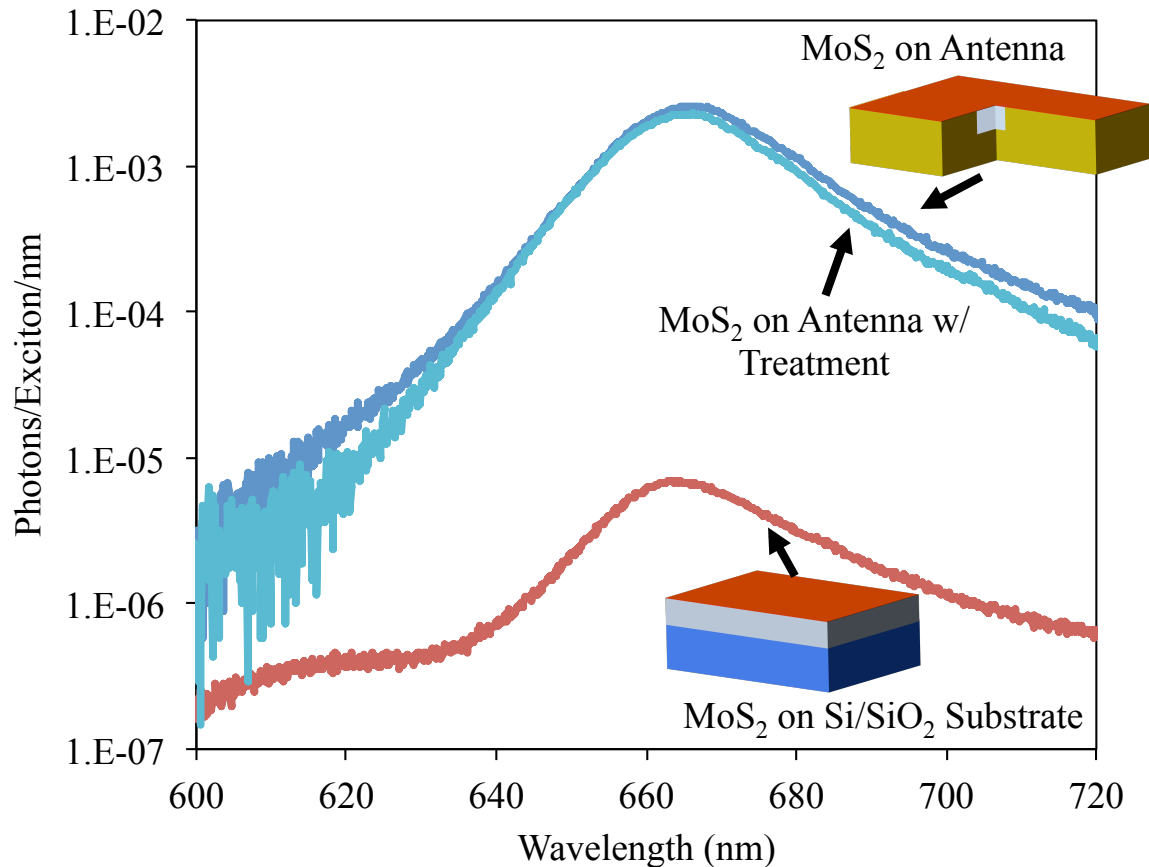
Figure 60. Calibrated quantum efficiency for the same MoS$_2$ as exfoliated on the Si/SiO$_2$ substrate, after transfer to the optical antennas, and after surface treatment.

The spontaneous emission rate of the antenna-coupled MoS$_2$ has only been enhanced in the antenna polarization. Since the as exfoliated monolayer emits equally in both polarizations, the spontaneous emission enhancement in the antenna polarization is 2x the boost in quantum efficiency. Therefore, these results are an indication of a spontaneous emission enhancement of 560x.

The super-acid surface treatment was then applied to the MoS$_2$ monolayer in an attempt to further increase the absolute quantum efficiency of these devices. If the efficiency were limited by non-radiative recombination at defects on the surface of the MoS$_2$ monolayer, applying the surface treatment should show improved quantum efficiency. However, the resulting PL obtained after surface treatment did not increase. This suggests that quantum efficiency was instead limited by the diffusion of excitons out of the "hotspot" of the antennas.

The results demonstrated here show that high efficiency and large spontaneous emission enhancement can be achieved in the same device. Further improvements on the absolute quantum efficiency of the devices will require some type of carrier confinement in order to eliminate diffusion of carriers as a loss mechanism. Recent experiments showing the growth of lateral heterojunctions using 2D semiconductors may provide a solution to this

problem [68]. Additionally, progress on efficient electrical injection of carriers into these 2D semiconductors will be required for an efficient antenna-enhanced LED.

7 Conclusion

This dissertation has examined the fundamental physics, practical limits, and experimental demonstration of antenna enhanced spontaneous emission in semiconductors. Beginning with a simple explanation of spontaneous emission as radiation from the dipole moment of the semiconductor, a circuit model was created to describe the tradeoffs and limits to enhanced spontaneous emission. By coupling to an optical antenna, the large mismatch between the size of a semiconductor's dipole moment and the wavelength of light emission is corrected and the spontaneous emission rate is increased. The circuit model theory described in this dissertation can be applied to any optical antenna and leads to several conclusions about how optical antennas should be designed and applied.

The application of optical antenna-enhanced LEDs for short-range optical interconnects was discussed. LEDs are typically insufficient for the emitters in optical interconnects due to the slow rate of spontaneous emission. However, by using an antenna the modulation rate of the LED can be greatly enhanced and exceed that of lasers. Antenna-enhanced LEDs may be operated at extremely low current levels and maintain their fast modulation speed making them ideal for the emitter in a low-power optical interconnect.

A complete description of spontaneous emission enhancement was developed through the development of a circuit model. The coupling of dipole sources to optical antennas was incorporated using Ramo's theorem. The antenna resonant frequency and quality factor was incorporated by treating the antenna as an RLC resonator. The effects of material properties at optical frequencies were described by the complex permittivity and added to the circuit model. Kinetic inductance was shown to be a parasitic effect that is included in a material's complex permittivity.

The anomalous skin effect and its impact on optical antennas were also described in this dissertation. This often neglected effect occurs when the skin depth of the electric field is shorter than the mean free path of electrons in the metal. The result is an increase in ohmic loss and decrease in efficiency. These additional losses can be incorporated in the optical antenna circuit model to give more accurate descriptions of achievable antenna efficiency. The anomalous skin effect is not included in standard FDTD or FEM solvers, so an example antenna design was analyzed to show the severity of this loss mechanism for antenna feedgaps below 10nm.

Antenna enhanced spontaneous emission was demonstrated on InP emitters. The arch-dipole antenna design was utilized to mitigate shorting due to a low impedance antenna gap. Photoluminescence measurements showed a 120x increase in emitted light intensity from the antenn-coupled InP over bare InP ridges. After accounting for the increased pump intensity, this result corresponded to a 14x increase in spontaneous emission rate.

The potential of 2D semiconductors for efficient antenna-enhanced LEDs was introduced. The cavity-backed slot antenna was shown to be an excellent antenna design for coupling to 2D semiconductors. The resonances of the cavity-backed slot antenna were explored through dark-field scattering measurements. WSe_2 monolayers were coupled to a silver cavity-backed slot antenna and etched to restrict emission only to the antenna hotspot. Properly tuned antennas demonstrated a 318x spontaneous emission enhancement. MoS2 monolayers were transferred to optical antenna arrays with resonances matched to the 660nm wavelength of MoS_2 emission. Photoluminescence results revealed an increase quantum efficiency of the MoS_2 from 0.025% as exfoliated to 7% when coupled to the optical antennas. The corresponding increase in spontaneous emission enhancement is estimated to be 560x. This result demonstrates that antenna-enhanced LEDs have the potential to be both fast and efficient light emitters.

8 Bibliography

[1] S. L. Chuang, *Physics of photonic devices*, vol. 80. John Wiley & Sons, 2012.

[2] A. Yariv, *Quantum Electronics*, 3 edition. New York: Wiley, 1989.

[3] L. G. Shantharama, A. R. Adams, C. N. Ahmad, and R. J. Nicholas, "The k.p interaction in InP and GaAs from the band-gap dependence of the effective mass," *J. Phys. C Solid State Phys.*, vol. 17, no. 25, p. 4429, 1984.

[4] C. A. Balanis, *Antenna Theory: Analysis and Design, 3rd Edition*, 3 edition. Hoboken, NJ: Wiley-Interscience, 2005.

[5] S. Ramo, "Currents Induced by Electron Motion," *Proc. IRE*, vol. 27, no. 9, pp. 584–585, Sep. 1939.

[6] W. Shockley, "Currents to Conductors Induced by a Moving Point Charge," *J. Appl. Phys.*, vol. 9, no. 10, pp. 635–636, Oct. 1938.

[7] J.-J. Greffet, M. Laroche, and F. Marquier, "Impedance of a Nanoantenna and a Single Quantum Emitter," *Phys. Rev. Lett.*, vol. 105, no. 11, p. 117701, Sep. 2010.

[8] E. Purcell, "Spontaneous emission probabilities at radio frequencies," in *Physical Review*, 1946, vol. 69, p. 681.

[9] A. F. Koenderink, "On the use of Purcell factors for plasmon antennas," *Opt. Lett.*, vol. 35, no. 24, p. 4208, Dec. 2010.

[10] "The Zettabyte Era—Trends and Analysis," *Cisco*. [Online]. Available: http://www.cisco.com/c/en/us/solutions/collateral/service-provider/visual-networking-index-vni/VNI_Hyperconnectivity_WP.html. [Accessed: 05-Apr-2016].

[11] J. Koomey, "Growth in data center electricity use 2005 to 2010," *Rep. Anal. Press Complet. Req. N. Y. Times*, p. 9, 2011.

[12] "NRDC: Data Center Efficiency Assessment - Scaling Up Energy Efficiency Across the Data Center Industry - Evaluating Key Drivers and Barriers (PDF) - data-center-efficiency-assessment-IP.pdf." [Online]. Available: https://www.nrdc.org/sites/default/files/data-center-efficiency-assessment-IP.pdf. [Accessed: 05-Apr-2016].

[13] M. Glick, "Optical Interconnects in Next Generation Data Centers: An End to End View," in *Optical Interconnects for Future Data Center Networks*, C. Kachris, K. Bergman, and I. Tomkos, Eds. Springer New York, 2013, pp. 31–46.

[14] N. Magen, A. Kolodny, U. Weiser, and N. Shamir, "Interconnect-power Dissipation in a Microprocessor," in *Proceedings of the 2004 International Workshop on System Level Interconnect Prediction*, New York, NY, USA, 2004, pp. 7–13.

[15] D. A. B. Miller, "Device Requirements for Optical Interconnects to Silicon Chips," *Proc. IEEE*, vol. 97, no. 7, pp. 1166–1185, Jul. 2009.

[16] E. Säckinger, *Broadband Circuits for Optical Fiber Communication*. John Wiley & Sons, 2005.

[17] S. W. C. L. A. Coldren, *Diode Lasers and Photonic Integrated Circuits: 1st (First) Edition*. Wiley, John & Sons, Incorporated, 1995.

[18] M. S. Eggleston and M. C. Wu, "Efficient Coupling of an Antenna-Enhanced nanoLED into an Integrated InP Waveguide," *Nano Lett.*, vol. 15, no. 5, pp. 3329–3333, May 2015.

[19]   S. A. Schelkunoff and H. T. Friis, *Antennas: theory and practice*, vol. 639. Wiley New York, 1952.

[20]   M. Staffaroni, J. Conway, S. Vedantam, J. Tang, and E. Yablonovitch, "Circuit analysis in metal-optics," *Photonics Nanostructures - Fundam. Appl.*, vol. 10, no. 1, pp. 166–176, Jan. 2012.

[21]   J. Lekner, "Capacitance coefficients of two spheres," *J. Electrost.*, vol. 69, no. 1, pp. 11–14, Feb. 2011.

[22]   J. B. Khurgin, "Ultimate limit of field confinement by surface plasmon polaritons," *Faraday Discuss*, vol. 178, pp. 109–122, 2015.

[23]   H. London, "The High-Frequency Resistance of Superconducting Tin," *Proc. R. Soc. Lond. Math. Phys. Eng. Sci.*, vol. 176, no. 967, pp. 522–533, Nov. 1940.

[24]   G. E. H. Reuter and E. H. Sondheimer, "The Theory of the Anomalous Skin Effect in Metals," *Proc. R. Soc. Lond. Math. Phys. Eng. Sci.*, vol. 195, no. 1042, pp. 336–364, Dec. 1948.

[25]   A. B. Pippard, "The Surface Impedance of Superconductors and Normal Metals at High Frequencies. II. The Anomalous Skin Effect in Normal Metals," *Proc. R. Soc. Lond. Math. Phys. Eng. Sci.*, vol. 191, no. 1026, pp. 385–399, Nov. 1947.

[26]   U. Kreibig and C. v Fragstein, "The limitation of electron mean free path in small silver particles," *Z. Für Phys.*, vol. 224, no. 4, pp. 307–323, 1969.

[27]   P. W. Gilberd, "The anomalous skin effect and the optical properties of metals," *J. Phys. F Met. Phys.*, vol. 12, no. 8, p. 1845, 1982.

[28]   T. Holstein, "Optical and Infrared Reflectivity of Metals at Low Temperatures," *Phys. Rev.*, vol. 88, no. 6, pp. 1427–1428, Dec. 1952.

[29]   P. B. Johnson and R.-W. Christy, "Optical constants of the noble metals," *Phys. Rev. B*, vol. 6, no. 12, p. 4370, 1972.

[30]   E. D. Palik, *Handbook of Optical Constants of Solids, Vol. 1*. San Diego: Academic Press, 1985.

[31]   N. A. Mortensen, S. Raza, M. Wubs, T. Søndergaard, and S. I. Bozhevolnyi, "A generalized non-local optical response theory for plasmonic nanostructures," *Nat. Commun.*, vol. 5, p. 3809, May 2014.

[32]   C. David and F. J. García de Abajo, "Spatial Nonlocality in the Optical Response of Metal Nanoparticles," *J. Phys. Chem. C*, vol. 115, no. 40, pp. 19470–19475, Oct. 2011.

[33]   J. M. McMahon, S. K. Gray, and G. C. Schatz, "Nonlocal Optical Response of Metal Nanostructures with Arbitrary Shape," *Phys. Rev. Lett.*, vol. 103, no. 9, p. 097403, Aug. 2009.

[34]   M. S. Eggleston, K. Messer, L. Zhang, E. Yablonovitch, and M. C. Wu, "Optical antenna enhanced spontaneous emission," *Proc. Natl. Acad. Sci.*, vol. 112, no. 6, pp. 1704–1709, Feb. 2015.

[35]   H. A. Wheeler, "Fundamental Limitations of Small Antennas," *Proc. IRE*, vol. 35, no. 12, pp. 1479–1484, Dec. 1947.

[36]   K. M. McPeak, S. V. Jayanti, S. J. P. Kress, S. Meyer, S. Iotti, A. Rossinelli, and D. J. Norris, "Plasmonic Films Can Easily Be Better: Rules and Recipes," *ACS Photonics*, vol. 2, no. 3, pp. 326–333, Mar. 2015.

[37]   Y. Jiang, S. Pillai, and M. A. Green, "Re-evaluation of literature values of silver optical constants," *Opt. Express*, vol. 23, no. 3, p. 2133, Feb. 2015.

[38]   G. M. Akselrod, C. Argyropoulos, T. B. Hoang, C. Ciracì, C. Fang, J. Huang, D. R. Smith, and M. H. Mikkelsen, "Probing the mechanisms of large Purcell enhancement in plasmonic nanoantennas," *Nat. Photonics*, vol. 8, no. 11, pp. 835–840, Oct. 2014.

[39]   H. G. Booker, "Slot aerials and their relation to complementary wire aerials (Babinet's principle)," *J. Inst. Electr. Eng. - Part IIIA Radiolocation*, vol. 93, no. 4, pp. 620–626, 1946.

[40]   M. S. Eggleston, "Metal Optics Based nanoLEDs: In Search of a Fast, Efficient, Nanoscale Light Emitter," *eScholarship*, Jan. 2015.

[41]   A. Kinkhabwala, Z. Yu, S. Fan, Y. Avlasevich, K. Müllen, and W. E. Moerner, "Large single-molecule fluorescence enhancements produced by a bowtie nanoantenna," *Nat. Photonics*, vol. 3, no. 11, pp. 654–657, Nov. 2009.

[42]   D. Fattal, M. Fiorentino, M. Tan, D. Houng, S. Y. Wang, and R. G. Beausoleil, "Design of an efficient light-emitting diode with 10 GHz modulation bandwidth," *Appl. Phys. Lett.*, vol. 93, no. 24, p. 243501, Dec. 2008.

[43]   D. Arbel, N. Berkovitch, A. Nevet, A. Peer, S. Cohen, D. Ritter, and M. Orenstein, "Light emission rate enhancement from InP MQW by plasmon nano-antenna arrays," *Opt. Express*, vol. 19, no. 10, p. 9807, May 2011.

[44]   K.-G. Lee, H. Eghlidi, X.-W. Chen, A. Renn, S. Götzinger, and V. Sandoghdar, "Spontaneous emission enhancement of a single molecule by a double-sphere nanoantenna across an interface," *Opt. Express*, vol. 20, no. 21, p. 23331, Oct. 2012.

[45]   K. J. Russell, T.-L. Liu, S. Cui, and E. L. Hu, "Large spontaneous emission enhancement in plasmonic nanocavities," *Nat. Photonics*, vol. 6, no. 7, pp. 459–462, Jul. 2012.

[46]   J.-H. Song, J. Kim, H. Jang, I. Yong Kim, I. Karnadi, J. Shin, J. H. Shin, and Y.-H. Lee, "Fast and bright spontaneous emission of Er3+ ions in metallic nanocavity," *Nat. Commun.*, vol. 6, p. 7080, May 2015.

[47]   T. J. Seok, A. Jamshidi, M. Eggleston, and M. C. Wu, "Mass-producible and efficient optical antennas with CMOS-fabricated nanometer-scale gap," *Opt. Express*, vol. 21, no. 14, p. 16561, Jul. 2013.

[48]   K. Messer, M. Eggleston, M. Wu, and E. Yablonovitch, "Enhanced Spontaneous Emission Rate of InP using an Optical Antenna," in *2014 Conference on Lasers and Electro-Optics (CLEO)*, 2014, p. STu1M.3.

[49]   A. R. Clawson, "Guide to references on III–V semiconductor chemical etching," *Mater. Sci. Eng. R Rep.*, vol. 31, no. 1, pp. 1–438, 2001.

[50]   P. Eliáš, I. Kostič, J. Šoltýs, and S. Hasenöhrl, "Wet-etch bulk micromachining of (100) InP substrates," *J. Micromechanics Microengineering*, vol. 14, no. 8, p. 1205, 2004.

[51]   F. Fiedler, A. Schlachetzki, and G. Klein, "Material-selective etching of InP and an InGaAsP alloy," *J. Mater. Sci.*, vol. 17, no. 10, pp. 2911–2918, Oct. 1982.

[52]   N. Matine, M. W. Dvorak, J. L. Pelouard, F. Pardo, and C. R. Bolognesi, "InP in HBTs by vertical and lateral wet etching," in *1998 International Conference on Indium Phosphide and Related Materials*, 1998, pp. 195–198.

[53]   T. L. Koch, P. J. Corvini, and W. T. Tsang, "Anisotropically etched deep gratings for InP/InGaAsP optical devices," *J. Appl. Phys.*, vol. 62, no. 8, pp. 3461–3463, Oct. 1987.

[54]   N. Engheta, C. H. Papas, and C. Elachi, "Radiation patterns of interfacial dipole antennas," *Radio Sci.*, vol. 17, no. 6, pp. 1557–1566, Nov. 1982.

[55]   E. Yablonovitch, "Statistical ray optics," *J. Opt. Soc. Am.*, vol. 72, no. 7, p. 899, Jul. 1982.

[56]   Y.-L. Chang, I.-H. Tan, Y.-H. Zhang, D. Bimberg, J. Merz, and E. Hu, "Reduced quantum efficiency of a near-surface quantum well," *J. Appl. Phys.*, vol. 74, no. 8, pp. 5144–5148, Oct. 1993.

[57]   K. F. Mak, C. Lee, J. Hone, J. Shan, and T. F. Heinz, "Atomically Thin MoS$_2$: A New Direct-Gap Semiconductor," *Phys. Rev. Lett.*, vol. 105, no. 13, p. 136805, Sep. 2010.

[58]   M. Amani, D.-H. Lien, D. Kiriya, J. Xiao, A. Azcatl, J. Noh, S. R. Madhvapathy, R. Addou, S. Kc, M. Dubey, K. Cho, R. M. Wallace, S.-C. Lee, J.-H. He, J. W. Ager, X. Zhang, E. Yablonovitch, and A. Javey, "Near-unity photoluminescence quantum yield in MoS2," *Science*, vol. 350, no. 6264, pp. 1065–1068, Nov. 2015.

[59]   B. Radisavljevic, A. Radenovic, J. Brivio, V. Giacometti, and A. Kis, "Single-layer MoS2 transistors," *Nat. Nanotechnol.*, vol. 6, no. 3, pp. 147–150, Mar. 2011.

[60]   R. Cheng, D. Li, H. Zhou, C. Wang, A. Yin, S. Jiang, Y. Liu, Y. Chen, Y. Huang, and X. Duan, "Electroluminescence and Photocurrent Generation from Atomically Sharp WSe2/MoS2 Heterojunction p–n Diodes," *Nano Lett.*, vol. 14, no. 10, pp. 5590–5597, Oct. 2014.

[61]   G. M. Akselrod, T. Ming, C. Argyropoulos, T. B. Hoang, Y. Lin, X. Ling, D. R. Smith, J. Kong, and M. H. Mikkelsen, "Leveraging Nanocavity Harmonics for Control of Optical Processes in 2D Semiconductors," *Nano Lett.*, vol. 15, no. 5, pp. 3578–3584, May 2015.

[62]   S. Najmaei, A. Mlayah, A. Arbouet, C. Girard, J. Léotin, and J. Lou, "Plasmonic Pumping of Excitonic Photoluminescence in Hybrid MoS2–Au Nanostructures," *ACS Nano*, vol. 8, no. 12, pp. 12682–12689, Dec. 2014.

[63]   N. Caselli, F. La China, W. Bao, F. Riboli, A. Gerardino, L. Li, E. H. Linfield, F. Pagliano, A. Fiore, P. J. Schuck, S. Cabrini, A. Weber-Bargioni, M. Gurioli, and F. Intonti, "Deep-subwavelength imaging of both electric and magnetic localized optical fields by plasmonic campanile nanoantenna," *Sci. Rep.*, vol. 5, p. 9606, Jun. 2015.

[64]   S. Bhargava, "Heat-Assisted Magnetic Recording: Fundamental Limits to Inverse Electromagnetic Design," 2015.

[65]   D. Dregely, R. Taubert, J. Dorfmüller, R. Vogelgesang, K. Kern, and H. Giessen, "3D optical Yagi-Uda nanoantenna array," *Nat. Commun.*, vol. 2, p. 267, Apr. 2011.

[66]   M. S. Eggleston, S. Desai, K. Messer, S. Madhvapathy, J. Xiao, X. Zhang, E. Yablonovitch, A. Javey, and M. C. Wu, "Enhanced spontaneous emission from an optical antenna coupled WSe2 monolayer," in *2015 Conference on Lasers and Electro-Optics (CLEO)*, 2015, pp. 1–2.

[67]   B. Mukherjee, F. Tseng, D. Gunlycke, K. K. Amara, G. Eda, and E. Simsek, "Complex electrical permittivity of the monolayer molybdenum disulfide (MoS_2) in near UV and visible," *Opt. Mater. Express*, vol. 5, no. 2, p. 447, Feb. 2015.

[68]   C. Huang, S. Wu, A. M. Sanchez, J. J. P. Peters, R. Beanland, J. S. Ross, P. Rivera, W. Yao, D. H. Cobden, and X. Xu, "Lateral heterojunctions within monolayer MoSe2–WSe2 semiconductors," *Nat. Mater.*, vol. 13, no. 12, pp. 1096–1101, Dec. 2014.

Appendix. Optical Setup for Photoluminescence Measurements

A schematic of the optical setup used for photoluminescence measurements in the MoS_2 and WSe_2 spontaneous emission experiments is shown in Figure 61. The optical setup is structured around the two turret system provided by an Eclipse TE-2000U Nikon microscope. The microscope setup also allows for several output ports to be selected so that switching between cameras for imaging and spectroscopy can be done quickly. Various configurations of optics within the two turret system allow for switching between bright-field imaging, dark-field imaging/spectroscopy, and photoluminescence imaging/spectroscopy without moving the sample.
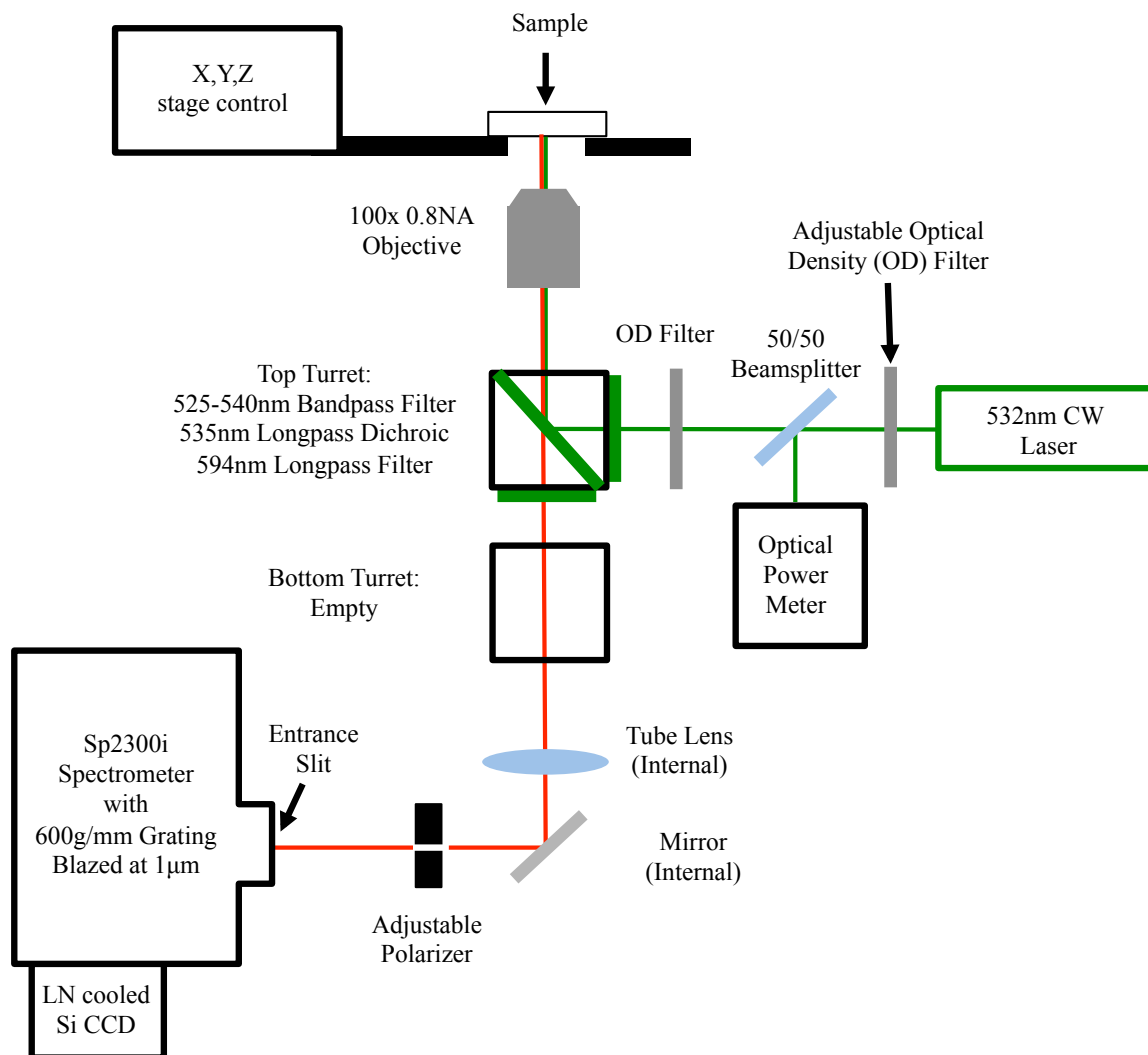

Figure 61. Schematic of optical setup used for photoluminescence measurements of WSe_2 and MoS_2 monolayers.

The sample is mounted on an X, Y, Z stage above the inverted microscope. All dark-field and photoluminescence measurements on the 2D semiconductors were performed using a 100x 0.8NA objective. The top turret was utilized for filtering the 532nm pump laser from longer wavelength photoluminescence. A bandpass filter (Semrock FF02-525/40) initially filters the pump laser. The dichroic filter (Semrock DiO2-R532) reflects the laser to the objective and allows longer wavelength PL to pass through. The long pass filter (Semrock BLP01-594R) removes any residual laser signal. The pump laser power was adjusted using an optical density filter wheel and measured by a Thorlabs S130C optical power meter.

The photoluminescence signal is then passed through a rotatable polarizer before illuminating the entrance slit of the Princeton Instruments Sp2300i Spectrometer. The entrance slit is positioned in the focal plane of the microscope allowing for imaging with the attached liquid nitrogen cooled Si CCD (Princeton Instruments 1340x100 array). By switching the grating turret of the spectrometer between a mirror and the 600g/mm grating, both PL imaging and spectroscopy can be performed.